Physik-Department

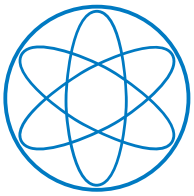

Measurement of the $Z \to \tau^+\tau^-$ production cross section in proton-proton collisions at 7 TeV center-of-mass energy with the ATLAS detector

Dissertation
von
Daniele Capriotti

München
Mai 2012

Max-Planck-Institut für Physik
(Werner-Heisenberg-Institut)

TECHNISCHE UNIVERSITÄT MÜNCHEN

Max-Planck-Institut für Physik
(Werner-Heisenberg-Institut)

Measurement of the $Z \to \tau^+\tau^-$ production cross section in proton-proton collisions at 7 TeV center-of-mass energy with the ATLAS detector

Daniele Capriotti

Vollständiger Abdruck der von der Fakultät für Physik der Technischen Universität München zur Erlangung des akademischen Grades eines

Doktors der Naturwissenschaften (Dr. rer. nat.)

genehmigten Dissertation.

Vorsitzender:	Univ.-Prof. Dr. A. Ibarra
Prüfer der Dissertation:	
1.	Priv.-Doz. Dr. H. Kroha
2.	Univ.-Prof. Dr. St. Schönert

Die Dissertation wurde am 8. Mai 2012 bei der Technischen Universität München eingereicht und durch die Fakultät für Physik am 11. Juni 2012 angenommen.

Abstract

The subject of this thesis is the measurement of the $Z \to \tau\tau$ production cross section in proton-proton collisions at a centre-of-mass energy of 7 TeV with the ATLAS detector at the Large Hadron Collider (LHC). The study of this process is important for several reasons. First, the measurement of the Z boson production in the $\tau\tau$ final state confirms the measurements in the electron and muon pair final states providing information about the parton density functions at the energy of the Large Hadron Collider. In addition, the search for a low mass Higgs boson decaying into τ lepton pairs requires knowledge of the inclusive $Z \to \tau\tau$ production cross section. $Z \to \tau\tau$ production is an important benchmark process for the validation of τ lepton reconstruction and identification which is very difficult at a hadron collider.

The reconstruction of $Z \to \tau\tau$ events can be performed in several final states depending on the decay modes of the τ leptons. The semi-leptonic final state, where one τ lepton decays into an electron or muon and neutrinos and the other one into hadrons plus neutrino, has been investigated in this thesis. The production cross section has been determined for data collected in 2011 corresponding to an integrated luminosity of 1.5 fb^{-1}. This involved the determination of the muon trigger and reconstruction efficiencies from data and the estimation of the multi-jet background with a data driven technique. The results using the semileptonic final states,

$$\sigma(pp \to Z + X, Z \to \tau\tau) = 998.1 \pm 23.7(\text{stat}) \pm 131.9(\text{syst}) \pm 36.9(\text{lumi})\ \text{pb} \quad (\tau_e\tau_\text{h}\ \text{channel}),$$

$$\sigma(pp \to Z + X, Z \to \tau\tau) = 912.4 \pm 15.0(\text{stat}) \pm 94.7(\text{syst}) \pm 33.7(\text{lumi})\ \text{pb} \quad (\tau_\mu\tau_\text{h}\ \text{channel}),$$

can be combined with the measurement in the $\tau_e\tau_\mu$ channel to

$$\sigma(pp \to Z + X, Z \to \tau\tau) = 920.6 \pm 16.7(\text{stat}) \pm 78.1(\text{syst}) \pm 34.0(\text{lumi})\ \text{pb} \quad (\text{combined})$$

and are in a good agreement with the theoretical expectation at NNLO.

Contents

You want to know how I did it?
This is how I did it, Anton:
I never saved anything for the swim back

Chapter 1

Introduction

The Standard Model describes with high accuracy the experimental observations in elementary particle physics. However there are aspects of the theory that are not confirmed experimentally yet. An important issue is the origin of the masses of elementary particles. In order to preserve the gauge invariance of the theory, fundamental particles are required to be massless. The Higgs mechanism gives masses to the particles without destroying the local gauge invariance by introducing a new scalar field, the Higgs boson field. The existence of the Higgs boson is not yet confirmed by experiments: its discovery or exclusion is one of the main goals of the experiments at the Large Hadron Collider (LHC) at CERN.

A brief introduction to the Standard Model is given in Chapter 2 together with a description of the phenomenology of the hadron collider physics.

The LHC is a proton proton collider with a maximal centre-of-mass energy of 14 TeV and a designed luminosity of 10^{34} cm^{-2}s^{-1}. It is designed to discover and study new phenomena like supersymmetric particles and to give answers to open questions in our current understanding of the elementary particles and their interactions like the origin of particle masses and the existence of the Higgs boson.

One of the two general-purpose detectors of the LHC is the ATLAS detector. A brief description of the Large Hadron Collider and of the ATLAS detector is given in Chapter 3.

In Chapter 4, the muon spectrometer of the ATLAS experiment is described in detail. The muon spectrometer measures the momenta of muons emerging from the high energy interactions with a resolution of better than 10% up to 1 TeV. Final states with muons play an important role for the measurements in this thesis.

The main subject of this thesis is the measurement of the cross section of $Z \to \tau\tau$ production in proton-proton collisions at a centre-of-mass energy of 7 TeV with the ATLAS experiment. The measurement of the inclusive Z cross section in $\tau\tau$ final states can confirm the measurement in the electron and muon pair final states. The search for a low mass Higgs boson decaying into τ pairs requires knowledge of the $Z \to \tau\tau$ cross section. In addition, the selection of a clean sample of $Z \to \tau\tau$ events is instrumental for studies of the performance of the reconstruction of hadronic τ decays. In Chapter 5, the reconstruction of the electrons, muons and hadronic τ decays needed for the $Z \to \tau\tau$ event selection is described.

The measurement of inclusive $Z \to \tau\tau$ production can be performed in several final states depending on the decay modes of the τ leptons. The semileptonic final state with one τ lepton decaying into an electron or muon and neutrinos (τ_e, τ_μ) and the other one into hadrons plus neutrino (τ_{h}) is described in this thesis. The study of the muon reconstruction performance with the so-called tag-and-probe method using $Z \to \mu\mu$ events is described in Chapter 6. It is mainly addressed to the $Z \to \tau\tau \to \tau_\mu\tau_{\mathrm{h}}$ production, although many of the results can be extended to other processes involving muons.

The $Z \to \tau\tau$ decays are studied with data collected by the ATLAS experiment during 2011 corresponding to an integrated luminosity of 1.5 fb^{-1}. The selection of signal events, the estimation of the main backgrounds from data and the determination of the cross section including systematic uncertainties are described in Chapter 7.

The results presented in this thesis have been approved by the ATLAS Collaboration and are published in [1].

Chapter 2

The Standard Model

The study of elementary particle physics began more than 100 years ago with the discovery of the electron. The analysis of the cosmic rays composition stimulated the curiosity of the scientific community at that time since the cosmic radiation was the only source of high energy particles. High energy accelerators were then developed, revealing a variety of new particles and exploring the structure of subnuclear matter.

The large variety of experimental data can be accounted for by the Standard Model of particle physics. The fundamental interactions relevant in particle physics are the electromagnetic, the weak and the strong force. At low energies these interactions appear to be completely unrelated. For example, they have very different coupling strengths which give rise to interaction cross sections which differ by about 12 orders of magnitude. At very high energies, the coupling constants may, however, converge to a single value and interactions between elementary particles may be explained in terms of a single unified force.

In the 1960s a major breakthrough along the road to unification of the forces was made by Glashow [2], Weinberg [3] and Salam [4] when they unified the electromagnetic and weak interactions reinforcing the belief in the existence of a single unified theory of the fundamental interactions. The most significant theoretical step in this direction was the realization that all fundamental interactions are invariant under *local gauge transformations*.

In the Standard Model, all the interactions are described by three gauge symmetry groups,

$$\mathrm{SU(3)_C} \otimes \mathrm{SU(2)_L} \otimes \mathrm{U(1)_Y}$$

for the strong interaction (Quantum Chromodynamics) and the unified weak and electromagnetic interactions (Electroweak Theory). The electroweak $SU(2)_L \otimes U(1)_Y$ gauge symmetry is broken via the Higgs mechanism which predicts the existence of the Higgs field.

2.1 Particles and interactions

According to the Standard Model, matter is composed of fundamental particles with spin ½ (fermions): six quarks and six leptons with different masses and electric charges. Leptons exist

as free particles while quarks (a part from the top quark) are grouped into baryons consisting of 3 quarks or mesons, bound states of a quark and an anti-quark.

Interactions between particles are described by the exchange of a virtual spin 1 boson specific for the interaction. Three fundamental interactions are described by the Standard Model. The strong interaction is responsible for binding the quarks together within mesons and baryons and is mediated by eight massless particles, the gluons. The electromagnetic interaction is mediated by one massless boson, the photon. The weak interaction is, for example, responsible for the β decays of nuclei with the associated emission of neutrinos and is mediated by the massive $W^{\pm}$ and Z^0 bosons. The gravitational interaction is the weakest of all interactions. It cannot yet be described by a quantum field theory and, therefore, is not part of the Standard Model.

The elementary particles and interactions of the Standard Model are listed in Table 2.1.

Table 2.1: The fundamental particles and interactions described by the Standard Model.

Spin ½	Particle			Q/|e|
Leptons	e	μ	τ	-1
	ν_e	ν_μ	ν_τ	0
Quarks	u	c	t	+2/3
	d	s	b	-1/3

Spin 1	Interaction	Q/|e|
Gluon, g	Strong	0
Photon, γ	Electromagnetic	0
$W^{\pm}$,Z^0	Weak	$\pm$1, 0

Spin 0	Q/|e|
Higgs	0

2.2 Symmetries and conservation laws

The invariance of the equations that describe the physical system under symmetry transformations is related to the conservation of physical quantities according to the *Noether Theorem* [5]. An example of such symmetry transformations are translations in space and time which correspond to the 4-momentum conservation.

The fundamental principle which determines the interactions of the Standard Model is the *gauge symmetry*, the invariance under continuous phase transformations of the matter field.

2.3 Quantum Chromodynamics

Quantum Chromodynamics (QCD) describes the strong interactions between colored quarks and gluons based on the $SU(3)_C$ gauge symmetry. The color charge of the quarks can have three values called red, blue and green. The interaction is mediated by eight gluons carrying color and an anti-color quantum number and belonging to a $SU(3)_C$ octet. A characteristic of the gluons in the $SU(3)_C$ gauge theory is their self-interaction due to their color charges.

At small distances, the interaction potential between quarks is Coulomb like, while it increases linearly at large distances leading to *quark confinement*:

$$V(r) = -\frac{4}{3}\frac{\alpha_S}{r} + kr$$

where α_S is the strong coupling and k is a phenomenological parameter. Free colored states do not exist. Increasing the distance between two color-charged particles leads to a linear increase in binding energy and eventually to the creation of quark-antiquark pairs from the vacuum. These new quarks are grouped together with the initial partons in color-neutral bound states, the hadrons, which are observed. This process is called *hadronization*.

Quarks interact weakly at small distances and at high energies allowing for perturbative calculation of cross sections. This feature is called *asymptotic freedom* and is typical of non-Abelian gauge field theories, where the gauge bosons carry charges of the gauge groups and thus have self-coupling.

2.4 The Electroweak interaction

All leptons and quarks interact via the weak force. The original Fermi theory of the weak interaction describing nuclear β decay assumed point-like coupling between four fermions. A serious difficulty arises when the Fermi theory is applied to scattering processes at high energies. The cross-section for elastic ν_e-e scattering, for instance, is proportional to $G^2 s$, where G is the weak Fermi coupling constant and s is the square of the centre-of-mass energy. The unitary violation at high energies can be avoided by introducing an intermediate gauge boson, the $W^{\pm}$, as mediator of the weak interaction. The amplitude for this process to lowest order in perturbation theory is of the form

$$M = \frac{g}{\sqrt{2}}(J^{\mu})^{\dagger}\frac{1}{M_W^2 - q^2}\frac{g}{\sqrt{2}}(J_{\mu}) \tag{2.1}$$

with the weak gauge coupling constant g and the mass of the $W^{\pm}$ boson M_W. It is a product of a weak isospin current $(J^{\mu})^{\dagger}$, a charge-raising weak current J_{μ}, both of which behave like vectors and axial-vectors under Lorentz and parity transformations (V-A structure), and the W boson propagator. Processes with charge-changing currents are called *charged current* weak interactions and are mediated by the exchange of charged bosons, $W^{\pm}$. The introduction of the charged weak bosons solved the unitarity violation of weak charged current processes. Weak neutral current processes like $\nu\bar{\nu} \rightarrow W^+W^-$ required the introduction of an additional neutral gauge boson, Z^0, to remove the unitary problem.

The Feynman graphs for electromagnetic and weak interactions between quarks and leptons show a strong similarity between them.

In 1960, Glashow [2], Weinberg [3] and Salam [4] described the electromagnetic and weak interactions within the framework of an unified electroweak gauge theory. In this theory, the weak coupling g is related to the electric charge by the relation

$$e = g \sin\theta_W \tag{2.2}$$

where θ_W is the Weinberg mixing angle which has to be determined experimentally.

The electroweak theory requires four massless gauge bosons arranged in a *weak isospin* (I) triplet $W_{\mu}^{(1)}$, $W_{\mu}^{(2)}$, $W_{\mu}^{(3)}$ of the $SU(2)_L$ group, and a *weak hypercharge* (Y) singlet B_{μ} of the

$U(1)_Y$ group.

The weak $SU(2)_L$ charge current interaction involves only left-handed fermions, while the electroweak neutral current $U(1)_Y$ interaction allows for both chirality.

The weak hypercharge Y is connected to the third component of the weak isospin I_3 and the electric charge Q by the Gell-Mann-Nishijima relation for the electroweak theory:

$$Y = 2Q - 2I_3. \tag{2.3}$$

Leptons and quarks are arranged in multiplets of the electroweak gauge group. The quantum numbers of left- and right-handed fermions are summarized in Table 2.2.

The weak gauge boson field $W_\mu^\pm$ and Z_μ^0 are massive while the photon field A_μ remains massless. The physical boson fields ($W_\mu^\pm$, Z_μ^0, A_μ) are related to the components of the weak isospin triplet ($W_\mu^{(1)}$, $W_\mu^{(2)}$, $W_\mu^{(3)}$) and weak hypercharge singlet (B_μ) by the following relations:

$$W_\mu^+ = \frac{W_\mu^{(1)} + iW_\mu^{(2)}}{\sqrt{2}}, \qquad W_\mu^- = \frac{W_\mu^{(1)} - iW_\mu^{(2)}}{\sqrt{2}}, \tag{2.4}$$

$$Z_\mu^0 = \cos\theta_W W_\mu^{(3)} - \sin\theta_W B_\mu, \qquad A_\mu = \sin\theta_W W_\mu^{(3)} + \cos\theta_W B_\mu. \tag{2.5}$$

Spontaneous breaking of the $SU(2)_L \otimes U(1)_Y$ symmetry is required to provide masses to the gauge bosons, preserving the local gauge invariance of the Lagrangian and the renormalisability of the theory. This is achieved by the introduction of a new scalar field and the Higgs mechanism [6, 7, 8] (see section 2.5).

Table 2.2: Fermion multiplets of the electroweak gauge group with their quantum numbers.

	Fermion Multiplets			I	I_3	Y	Q
leptons	$\begin{pmatrix}\nu_e\\ e^-\end{pmatrix}_L$	$\begin{pmatrix}\nu_\mu\\ \mu^-\end{pmatrix}_L$	$\begin{pmatrix}\nu_\tau\\ \tau^-\end{pmatrix}_L$	1/2 1/2	1/2 -1/2	-1/2 -1/2	0 -1
	e_R^-	μ_R^-	τ_R^-	0	0	-2	-1
quarks	$\begin{pmatrix}u\\ d\end{pmatrix}_L$	$\begin{pmatrix}c\\ s\end{pmatrix}_L$	$\begin{pmatrix}t\\ b\end{pmatrix}_L$	1/2 1/2	1/2 -1/2	1/3 1/3	2/3 -1/3
	u_R	c_R	t_R	0	0	4/3	2/3
	d_R	s_R	b_R	0	0	-2/3	-1/3

2.5 The Higgs mechanism

The invariance of the electroweak Lagrangian under local gauge transformations demands massless gauge bosons ($W^\pm$ and Z^0) and fermions, while the observed particles are massive. The $SU(2)_L \otimes U(1)_Y$ gauge symmetry is spontaneously broken providing masses to the weak gauge bosons and the fermions (Higgs mechanism).

The electroweak gauge symmetry is spontaneously broken by requiring the ground state of the system - the *vacuum* - to acquire a non-zero expectation value making it non-invariant under the gauge transformations.
At high energies (much greater than 100 GeV), the masses become negligible and the gauge symmetry is restored. At low energy, the symmetry is broken such that the weak W and Z bosons become massive, while the photon remains massless.

The Higgs mechanism introduces four scalar fields φ_i arranged in a complex weak isospin doublet with hypercharge $Y = 1$:

$$\varphi = \begin{pmatrix} \varphi^+ \\ \varphi^0 \end{pmatrix} = \frac{1}{\sqrt{2}} \begin{pmatrix} \varphi_1 + i\varphi_1' \\ \varphi_2 + i\varphi_2' \end{pmatrix}. \tag{2.6}$$

The scalar Lagrangian invariant under $SU(2)_L \otimes U(1)_Y$ is

$$\mathscr{L} = (\mathscr{D}_\mu \varphi)^\dagger (\mathscr{D}^\mu \varphi) - \mu^2 \varphi^\dagger \varphi - \lambda(\varphi^\dagger \varphi)^2 \tag{2.7}$$

with the covariant derivative

$$\mathscr{D}_\mu = \partial_\mu - g\mathbf{I} \cdot \mathbf{W}_\mu - (g'/2) Y B_\mu. \tag{2.8}$$

with the weak charged and neutral current coupling constants $g = \frac{e}{\cos\theta_W}$ and $g' = \frac{e}{\sin\theta_W}$ respectively. The first term in 2.7 is the kinetic term, while the second and third terms represent the self-interaction potential of the scalar field.

Figure 2.1 shows the potential for $\mu^2 > 0$ (left) and $\mu^2 < 0$ (right). The extremum at $\varphi = 0$ is not a minimum in the case of $\mu^2 < 0$ but there are minima for $|\varphi| = \pm v = \pm\sqrt{-\mu^2/\lambda}$, where v is the vacuum expectation value of the scalar field.

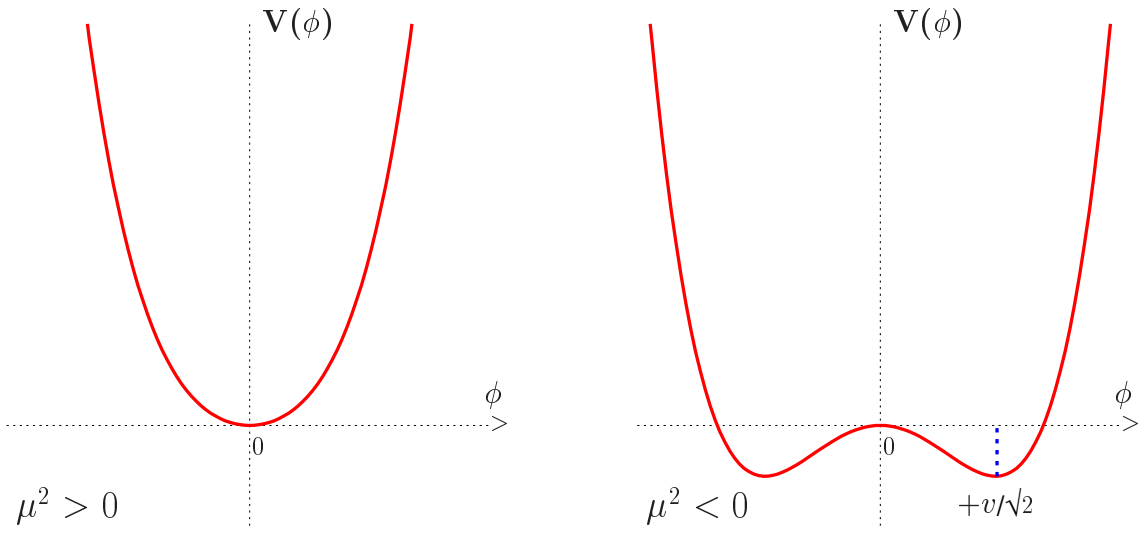

Figure 2.1: The Higgs potential for $\mu^2 > 0$ (left) and $\mu^2 < 0$ (right) [9]. In the latter case, the selection of a particular ground state breaks the electroweak gauge symmetry of the Lagrangian.

The $SU(2)_L \otimes U(1)_Y$ symmetry is *spontaneously broken* when one of the ground states for $\mu^2 < 0$ is chosen. One can choose the vacuum state by selecting a specific direction in the space of the four scalar fields:

$$\varphi = \frac{1}{\sqrt{2}} \begin{pmatrix} 0 \\ \upsilon \end{pmatrix}. \tag{2.9}$$

Perturbation theory can be formulated in terms of excitations from the new ground state defined as the scalar Higgs boson field $H(x)$. After a $SU(2)_L$ gauge transformation eliminating the complex phase of the scalar field φ it can be parametrized as

$$\varphi(x) = \frac{1}{\sqrt{2}} \begin{pmatrix} 0 \\ \upsilon + H(x) \end{pmatrix}. \tag{2.10}$$

Equations 2.4, 2.5 and 2.10 are introduced into the Lagrangian 2.7, and the following expression for the kinetic term is obtained:

$$(\mathscr{D}_\mu \varphi)^\dagger (\mathscr{D}^\mu \varphi) = \frac{g^2 \upsilon^2}{8} (W_\mu^+ W^{+\mu} + W_\mu^- W^{-\mu}) + \frac{g^2 \upsilon^2}{8 \cos^2 \theta_W} Z_\mu Z^\mu. \tag{2.11}$$

which are mass terms for the $W_\mu^\pm$ and Z_μ fields. The gauge bosons $W^\pm$ and Z^0 acquire masses through the interaction with the Higgs field. The masses are given by the following relation:

$$m_Z \cos \theta_W = m_W = \frac{g\upsilon}{2}. \tag{2.12}$$

The masses of the fermions are generated by the couplings of the fermions f to the Higgs field, which requires an additional term in the Lagrangian

$$\mathscr{L} = -m_f \bar{f} f - (g_f/\sqrt{2}) \bar{f} f H. \tag{2.13}$$

for each fermion. The Lagrangian contains the fermion masses $m_f = g_f \upsilon/\sqrt{2}$ and the fermion couplings g_f to the Higgs boson which are proportional to the fermion mass. Neutrinos do not couple to the Higgs boson in the original formulation of the theory without right-handed neutrino states.

2.6 Phenomenology of Z^0 boson productions at hadron colliders

The Glashow-Salam-Weinberg theory predicts the existence of the $W^\pm$ and Z^0 bosons and their properties. In 1983, the three weak gauge bosons have been discovered by the UA1 and UA2 experiments at CERN [10, 11, 12, 13] with the predicted properties.

The Z^0 boson can decay into fermion-antifermion pairs. In comparison to the $W^\pm$ production, the Z^0 production cross section is about one-tenth. The Z^0 boson decays into lepton pairs provide a clean signature for identification and can be reconstructed accurately. For this reason, the measurement of the Z^0 decays is very important both for the test of the Standard Model and for detector calibration.

A precise measurement of the Z^0 mass was performed by the four experiments (ALEPH, DELPHI, L3 and OPAL) [14] at the LEP, an electron-positron collider [15]:

$$M_{Z^0} = 91.188 \pm 0.002\ GeV.$$

The branching ratios corresponding to the partial decay widths of the Z^0 are listed in Table 2.3.

Table 2.3: Partial widths and branching ratios decays [14].

Modes	partial width (MeV)	BR($Z^0 \to X$)%
e^+e^-	83.91 ± 0.12	3.363 ± 0.004
$\mu^+\mu^-$	83.99 ± 0.18	3.366 ± 0.007
$\tau^+\tau^-$	84.08 ± 0.22	3.367 ± 0.008
Hadrons	1744.4 ± 2.0	69.91 ± 0.06
Neutrinos	499.0 ± 1.5	20.00 ± 0.06

The cross section for Z production in proton proton collisions is calculated to NNLO in perturbation theory. The fundamental process is the $q\bar{q} \to Z$ interaction:

$$\sigma_Z^{q\bar{q}} = \frac{8\pi}{3}\frac{G_F M_Z^2}{\sqrt{2}}(g_V^2 + g_A^2)\delta(Q^2 - M_Z^2) \tag{2.14}$$

where $Q^2 = x_a x_b s$, x_a and x_b the momentum fractions of the five quarks involved, s their centre-of-mass energy squared, $g_V^2 + g_A^2 = (1 - 4|e_q| \sin^2\theta_W + 8e_q^2 \sin^4\theta_W)/8$, e_q is the quark charge and θ_W is the Weinberg angle. The Z^0 production cross section in proton-proton collisions is the convolution of the relation 2.14 with the quark and antiquark distribution functions $q(x, Q^2)$ in the proton, which give the probability to encounter a parton a with momentum fraction x_a:

$$\sigma^{pp\to ZX} = \sum_q \int dx_a dx_b [q(x_a, Q^2)\bar{q}(x_b, Q^2) + a \leftrightarrow b]\sigma_Z^{q\bar{q}}. \tag{2.15}$$

In addition to the primary "hard" interaction, many "soft" QCD interactions occur among the colliding and the spectator partons. The confinement of quarks and gluons requires that outgoing colored partons from the soft interactions undergo hadronization into colorless hadrons.

The Z^0 production cross section depends on the parton density functions (PDFs) of the proton: different parametrization of the PDFs predict different Z boson production rates. The differences between the predictions are taken into account as theoretical uncertainties.

Chapter 3

The ATLAS experiment at the Large Hadron Collider

In this chapter an overview of the ATLAS experiment at the Large Hadron Collider (LHC) [16] at CERN is given.

On 20 November 2009, the LHC started to collide protons at a centre-of-mass energy of 900 GeV. On 30 March 2010, the LHC achieved with 7 TeV the highest center-of-mass energy ever reached at colliders. The LHC experiments collected data at 7 TeV in 2010 and 2011. From 2014, after further improvements of the accelerator, the LHC will run at its designed centre-of-mass energy of 14 TeV. The lower energy of 7 TeV is, however, sufficient to perform precision measurements of the Standard Model processes at the highest energies and to search for the Higgs boson and new physics beyond the Standard Model.

3.1 The Large Hadron Collider

The Large Hadron Collider (LHC) is the highest-energy particle accelerator. It is designed to accelerate proton beams up to an energy of 7 TeV per beam. For safety reasons, it started operation at a beam energy of only 3.5 TeV.

The LHC was built to test predictions of the Standard Model at the highest energies, to verify the existence of the Higgs boson and to search for new phenomena beyond the Standard Model.

The LHC is installed in a tunnel of 26.7 km circumference which housed the Large Electron Positron Collider (LEP) [15] until the year 2002.

In order to produce rare events with sufficient rate, the LHC is designed to reach a maximum luminosity of $10^{34}\text{cm}^{-2}\text{s}^{-1}$. The protons are kept on their circular path by superconducting dipole magnets which are cooled with liquid helium at 1.9 K temperature.

The event rate for a process with cross section σ is given by:

$$N = \sigma \int \mathcal{L} dt = \sigma L,$$

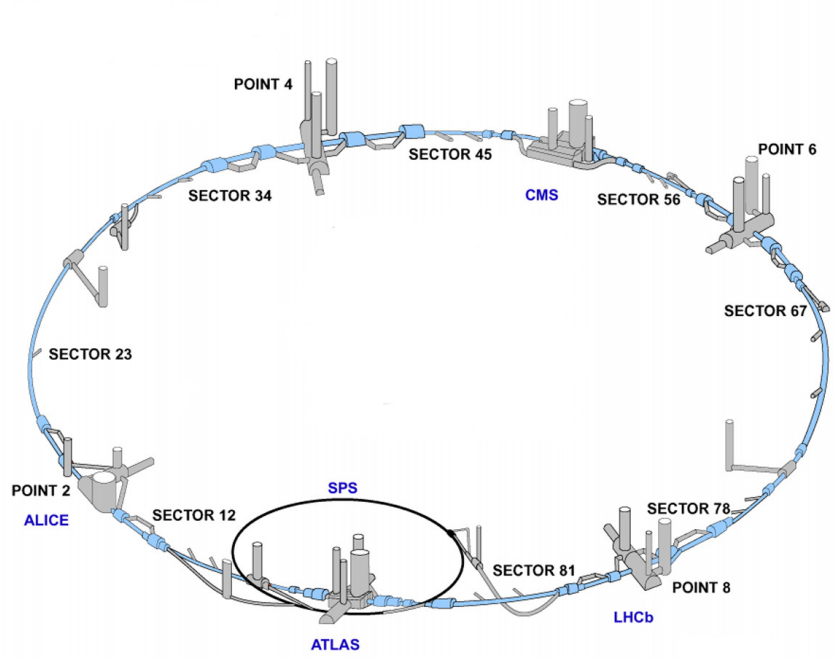

Figure 3.1: View of the LHC system.

where $\mathcal{L}$ is the instantaneous luminosity and L the integrated luminosity. The instantaneous luminosity is a parameter of the collider and depends on the beam shape and on the number of protons in each beam. At the design luminosity, the bunch crossing frequency is 40 MHz.

Figure 3.1 shows the LHC ring with the four detectors located at the interaction points:

The ATLAS Detector (A Toroidal LHC ApparatuS) [17] is one of the general purpose experiments. Data taken with the ATLAS detector are used for this thesis.

The CMS Detector (Compact Muon Solenoid) [18] is the second general purpose experiment. Like ATLAS, it is designed to fully exploit the discovery potential of the LHC.

The ALICE Detector (A Large Ion Collider Experiment) [19] is designed to study the strong interaction and the Quark-Gluon Plasma (QGP) in heavy-ion (Pb-Pb) collisions.

The LHCb Detector (Large Hadron Collider beauty) [20] is a dedicated B-physics experiment. The aim of the experiment is the search for new physics via precision measurements of CP violating effects in B hadron decays and in rare decays, which are mostly produced in forward direction with respect to the beam.

Table 3.1: LHC beam parameters for the peak luminosity.

	Unit	Injection	Collision
Number of particles / bunch	-	$1.15 \cdot 10^{11}$	
Number of bunches / beam	-	2808	
Circulating beam current	(A)	0.582	
Proton Energy	(GeV)	450	7000
RMS transverse beam size	(μm)	375.2	16.7
Stored beam energy	(MJ)	23.3	362
Bunch crossing frequency	(MHz)	-	40

3.2 The ATLAS detector

ATLAS is composed of dedicated sub-detectors to fulfill the required tasks:

- The inner tracking system measures the tracks and momenta of charge particles and allows for the identification of electrons. In addition, decay vertices of particles are reconstructed accurately.
- The calorimeters identify electrons, photons and hadron jets and measure their energy and direction. With their good hermeticity and angular coverage they also allow for the measurement of missing transverse energy.
- The muon spectrometer identifies muons and measures precisely their momenta.
- A highly selective trigger system is required to suppress the huge background at the LHC.

3.2.1 The coordinate system

For the ATLAS detector the following right-handed coordinate system has been defined.

The z direction is parallel to the beam pipe with the origin located at the center of the detector. The x direction points to the center of the LHC ring, while the y axis points upwards.

The azimuthal angle ϕ and the polar angle θ are defined with respect to the z axis. Instead of the polar angle, the pseudorapidity η is frequently used at colliders:

$$\eta = -\ln \tan(\theta/2).$$

Distances in the η-ϕ plane are given by

$$\Delta R = \sqrt{\Delta\eta^2 + \phi^2}.$$

3.2.2 The magnet system

The ATLAS magnet system [21] consists of four superconducting magnets.

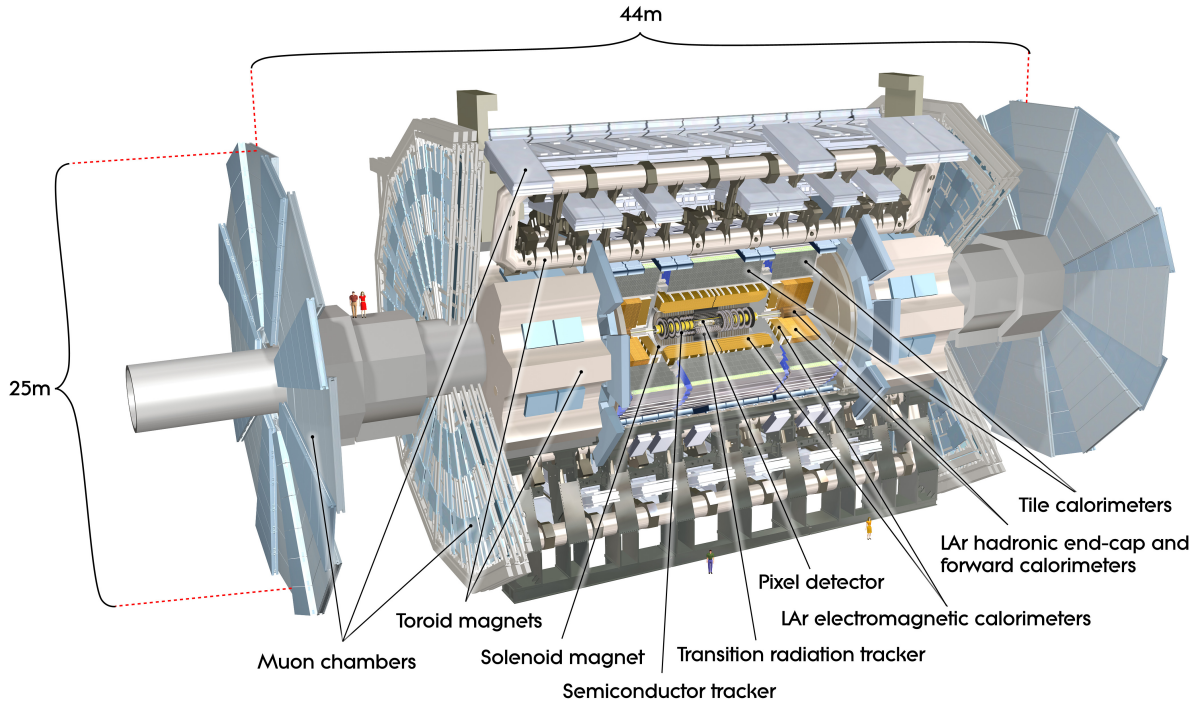

Figure 3.2: View of the ATLAS detector.

The central solenoid magnet surrounds the inner detector and provides a magnetic field strength of 2 T. The solenoid magnet operates at a temperature of 4 K. The solenoid coil extends 5.8 m in length and 2.6 m in diameter. Particles created at the interaction point are deflected by the solenoidal magnetic field in the R-ϕ plane.

Three air-core toroid magnets provide the magnetic field in the muon spectrometer. Each system (one in the barrel and two in the end-caps) is composed of eight coils. The air-core structure is chosen to minimize the contribution of the multiple scattering to the muon momentum resolution. Details about the magnet system in the muon spectrometer are given in Chapter 4.

3.2.3 The Inner Detector

At the design luminosity of $10^{34}\text{cm}^{-2}\text{s}^{-1}$, the LHC proton beams will collide in ATLAS every 25 ns. At each bunch crossing, approximately 1000 tracks will emerge from the interaction point within $|\eta| < 2.5$. In the inner detector, fast and highly granular detectors are used to provide precise momentum measurement of charged particles as well as accurate reconstruction of secondary vertices close to the beam pipe.

The inner detector of ATLAS [22] is 7 m long and 2.30 m in diameter (Fig. 3.4). It is composed of three sub-detectors, namely the silicon pixel detector, the semiconductor tracker (SCT) and the transition radiation tracker (TRT). The goal of this detector is the reconstruction and momentum measurement of charged particle tracks, for transverse momenta $p_T > 0.5$ GeV

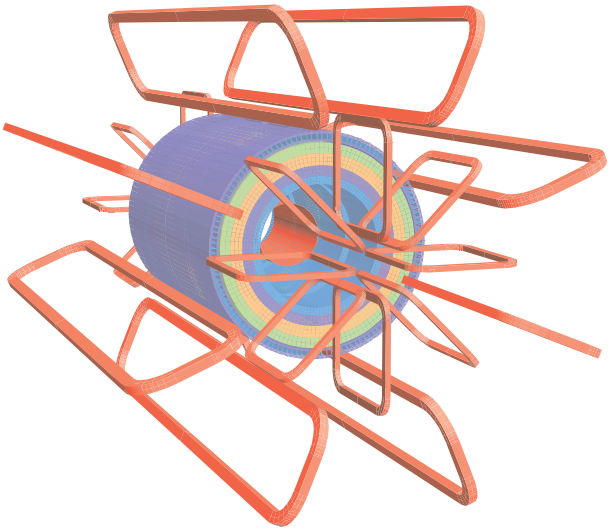

Figure 3.3: View of the ATLAS magnet system.

within $|\eta| < 2.5$. In the solenoidal magnetic field of 2 T, a transverse momentum resolution of

$$\sigma_{\mathrm{p_T}}/\mathrm{p_T} = 0.05\%\mathrm{p_T} \oplus 1\%$$

is achieved. In addition, high precision in the reconstruction of secondary vertices is needed, in particular for the identification of b quark decays.

The pixel sub-detector is mounted close to the interaction point. It has very high granularity to achieve high spatial resolution close to the interaction point. The pixel detector is composed of three barrel layers at radii of 5, 9 and 12 cm, and five disks in each end-cap with radial extension from 11 to 20 cm completing the solid angle coverage. The innermost layer in the barrel, called b-layer, is crucial for the vertex location capabilities of the inner detector, especially for the reconstruction heavy flavor decays. Each pixel is 50 μm wide in R-ϕ and 400 μm long in z. The pixel detector provides an excellent position resolution of 10 μm in R-ϕ and 115 μm in z(R) in the barrel (endcap). Three space points are measured for a typical track crossing the pixel detector.

The pixel detector is surrounded by the semiconductor tracker (SCT) which is composed of four double layers of silicon strip detectors and typically provides four space points per track. Each double layer contains strips aligned along the z direction and strips rotated by a stereo angle of 40 mrad with respect to the beam line providing z coordinate information. The strips have a pitch of 80 μm and are 12 cm long. The spatial resolution achieved by the SCT is 17 μm in R-ϕ and 580 μm in z (R) for the barrel (endcap) region.

The outermost tracking detector, the Transition Radiation Tracker (TRT), is composed of 36 layers of 4 mm diameter straw drift tubes. The small diameter allows for low occupancy and high tracking efficiency and spacial resolution even at the high particle densities and rates at the

LHC. Electron identification is performed by using a $Xe/CO_2/O_2$ gas mixture which is sensitive to the transition radiation photons created in radiator foils between the straws. Ultra-relativistic electrons passing through the numerous dielectric boundaries of these foils produce transition radiation which enhances ionization signal in the gas mixture. The large number of track points provides efficient track reconstruction within the TRT acceptance ($|\eta| < 2.0$). Each straw in the barrel part of the TRT provide an R-ϕ coordinate measurement with a precision of 130 μm.

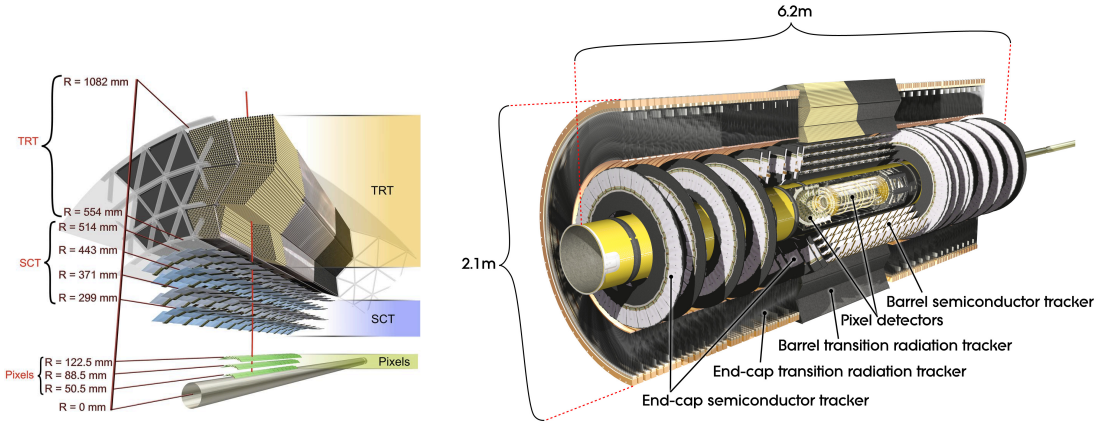

Figure 3.4: Views of the ATLAS inner detector.

3.2.4 The Calorimeter System

The calorimeters are important for the reconstruction of many final states involving electrons, photons and hadron jets. In addition, they provide information about the missing transverse energy of the events and allow for the identification of hadronic τ decays.

The ATLAS detector contains an electromagnetic [23] and an hadron calorimeter [24]. Figure 3.5 gives an overview of the ATLAS calorimeter system. All calorimeters are sampling calorimeters and provide full solid angle coverage up to $|\eta| = 4.9$.

The electromagnetic calorimeter uses liquid Argon as active medium and lead absorber plates which, like the readout electrode boards, are accordion-shaped. The electromagnetic (EM) calorimeter consists of a barrel part extending up to $|\eta| = 1.5$ and two end-caps (EMEC) up to $|\eta| = 3.2$ which are complemented by two forward calorimeters in the region up to $|\eta| = 4.9$. The total thickness of the EM calorimeter is more than 24 radiation lengths (X_0) in the barrel and 26 radiation lengths in the end-caps. In the range $|\eta| < 1.8$, the calorimeter is equipped with a presampling detector in front which provides an estimation of the energy losses of electrons and photons before entering the calorimeter. The EM calorimeter is segmented longitudinally along the particle direction in several layers in order to measure the longitudinal shower profiles. Within $|\eta| < 2.5$ (the inner detector acceptance), there are three principal shower samplings. The first layer is equipped with readout strips with a pitch of 4 mm in η. This assures a precise position measurement in this direction and allows for good particle

Table 3.2: Parameters for the ATLAS calorimeters. The energy resolutions are from test beam measurements [25, 27].

Name	η range	Absorber / active material	Energy resolution (stochastic)	(constant)
EM	<1.5	lead / LAr	$(10.1\pm0.4)\%/\sqrt{E}$	$(0.2\pm0.1)\%$
EMEC	1.5 - 3.2	lead / LAr	$(10.1\pm0.4)\%/\sqrt{E}$	$(0.2\pm0.1)\%$
Tile	<1.7	steel / scint	$(52.0\pm1.0)\%/\sqrt{E}$	$(3.0\pm0.1)\%$
HEC	1.5 - 3.2	copper / LAr	$(70.6\pm1.5)\%/\sqrt{E}$	$(5.8\pm0.2)\%$
FCal1	3.2 - 4.9	copper / LAr	$(28.5\pm1.0)\%/\sqrt{E}$	$(3.5\pm0.1)\%$
FCal2+3	3.2 - 4.9	tung. / LAr	$(94.2\pm1.6)\%/\sqrt{E}$	$(7.5\pm0.14)\%$

identification. This layer acts as "preshower" detector with a thickness of 6 X_0. The second layer is segmented into towers of size $\Delta\eta \times \Delta\phi = 0.025 \times 0.025$. With a thickness of 16 X_0, this is the largest which absorbs most of the electromagnetic energy of a shower. The third layer has coarser granularity and a thickness varying from 2 X_0 to 12 X_0. This layer is used to estimate energy leakage of the EM showers into the subsequent hadron calorimeter. In the range $2.5 < |\eta| < 3.2$, the electromagnetic end-cap (EMEC) calorimeters have a coarser granularity and only two samplings. In the forward range $|\eta| > 3.2$, a different type of liquid Argon calorimeters (FCAL) measures both the electromagnetic and the hadronic components of showers. They are longitudinally segmented into three different layers, each with a granularity of $\Delta\eta \times \Delta\phi \approx 0.2 \times 0.2$.

The hadron calorimeters (HCAL) surround the electromagnetic calorimeter. Their thickness of 11 interaction lengths is important to minimize the punch-through of hadrons into the muon spectrometer. Different technologies are used in different η-regions. For $|\eta| < 1.6$, an iron-scintillating-tile calorimeter is used in the barrel and extended barrel. The scintillation light is read out by photomultiplier tubes located behind each calorimeter module. In the region $1.5 < |\eta| < 3.2$, liquid Argon is used as active material in combination with copper absorber plates used to increase the stopping power of the hadron calorimeter. The forward calorimeter uses Argon as active material embedded in a tungsten absorber matrix and extends the acceptance up to $|\eta| = 4.9$. The hadron end-cap and the forward calorimeter is placed in the same cryostat together with the EMEC calorimeter.

3.2.5 The Muon Spectrometer

The muon spectrometer [28] has been designed to fulfill the following requirements:

- Stand-alone identification and reconstruction of muons with high efficiency and a momentum resolution of better than 10% up to energies of 1 TeV. Multiple scattering is minimized by employing air-core toroid magnets.
- Coverage up to $|\eta| = 2.7$.

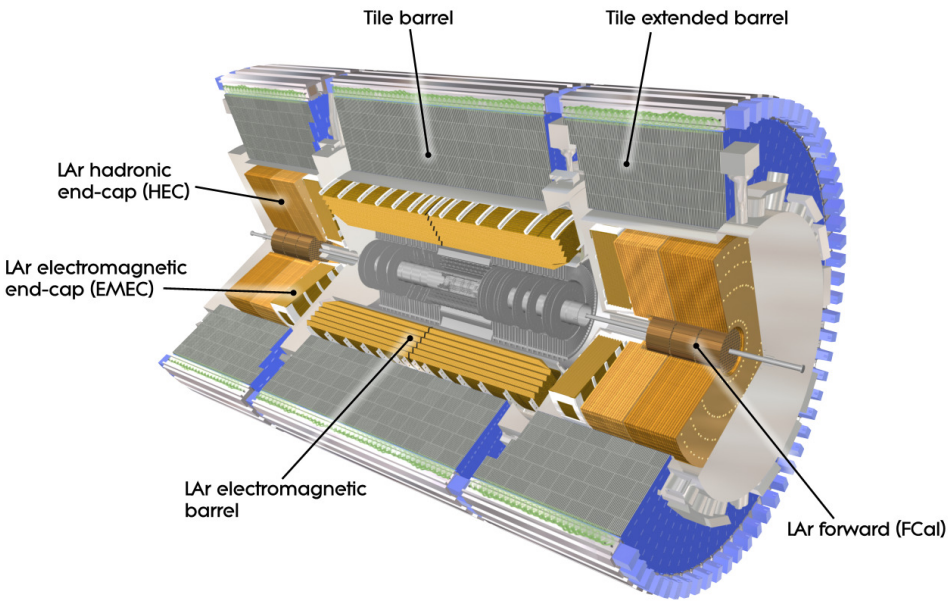

Figure 3.5: View of the ATLAS calorimeter system.

- Single and multiple muon trigger information with programmable momentum thresholds.
- Reliable operation and stable performance over a long period in a high irradiation environment.

Details about the muon spectrometer are given in Chapter 4.

3.3 Trigger and data acquisition

The majority of collisions at the LHC at a rate of 40 MHz is not interesting for the physics program and cannot be stored. On the other hand, interesting events must be kept.

The trigger selects interesting events out of the overwhelming background. The trigger selection proceeds in three consecutive levels, namely L1, L2 and the Event Filter. Each level refines the trigger decision of the previous step. The first level (L1) is completely hardware based and uses only limited amount of detector information in order to provide decisions within less than 2.5 μs. It uses information provided by the muon spectrometer and the calorimeters exploiting not the full granularity. Events with high-p_T muons, electrons, photons, jets and hadronically decaying τ leptons as well as with large total and missing transverse energy are selected. The associated Regions-of-Interest (RoI), i.e. the regions in the detector where interesting patterns have been identified, are passed to the second trigger level (L2) at a rate of 75 kHz. The L2 selection criteria are chosen such that the event rate is reduced to 3.5 kHz at an event processing time of 40 ms. For events selected by the L2 trigger, the full detector information is collected by

the Event Builder and passed to the Event Filter (EF). This last step is entirely software based. Offline event reconstruction algorithms are employed and the final trigger decision is provided at an event processing time on the order of four seconds leading to a final event rate of 200 Hz recorded on mass-storage devices for further processing and physics analyses. The data volume recorded by the experiments at the LHC cannot be stored and processed at one local computing center alone. Therefore, after initial processing at CERN, the recorded data are distributed to many computing centers outside of CERN which together form the LHC Computing Grid (LCG), a worldwide computing framework [29].

3.4 Luminosity monitoring

The measurement of the cross sections of physics processes requires the knowledge of the luminosity delivered by the LHC. An ATLAS run contains several Luminosity Blocks (LBs). A LB is a time interval (on the order of a minute) for which the integrated luminosity is determined. By dividing a run into several LBs, ATLAS can process data more efficiently by removing any LBs affected by failures of detector components. Over each LB, the instantaneous luminosity is essentially constant.

The main detector for the ATLAS luminosity monitoring is LUCID (LUminosity measurement using Čerenkov Integrating Detector). LUCID also identifies individual bunch crossings. LUCID detectors are placed at $z = \pm 17$ m from the interaction point. The detectors consist of twenty 15 mm diameter drift tubes filled with C_4F_{10}. The drift tubes are arranged around the beam pipe at a radial distance of 10 cm.

The absolute luminosity is measured by ALFA (Absolute Luminosity For ATLAS) which is located at a distance of 240 m from the interaction point. ALFA measures the elastic scattering rate of proton-proton collisions which is related to the total cross section.

Chapter 4

The ATLAS Muon Spectrometer

Muon final states provide a clean and robust signature for many physics processes including those involving decays of new heavy particles. The muon spectrometer is a stand-alone detector which allows for the trigger and track measurement of the muons independently of the inner detector.

The acceptance of the muon spectrometer is $|\eta| < 2.7$.

Three superconducting air-core toroid magnets deflect the muons in the R-η plane.

The muon spectrometer is equipped with three layers of Monitored Drift Tube (MDT) chambers in the barrel region, arranged in cylindrical layers around the beam axis. In the end-caps, MDT chambers are used together with Cathode Strip Chambers (CSC), arranged in wheels perpendicular to the beam axis.

Resistive Plate Chambers (RPC) in the barrel middle and outer layers, and Thin Gap Chambers (TGC) in the end-cap inner and middle layers, complement the precision tracking chambers to provide measurement of the non-bending coordinate ϕ and to trigger on high-momentum muons. The acceptance of the muon trigger system is $|\eta| < 2.4$.

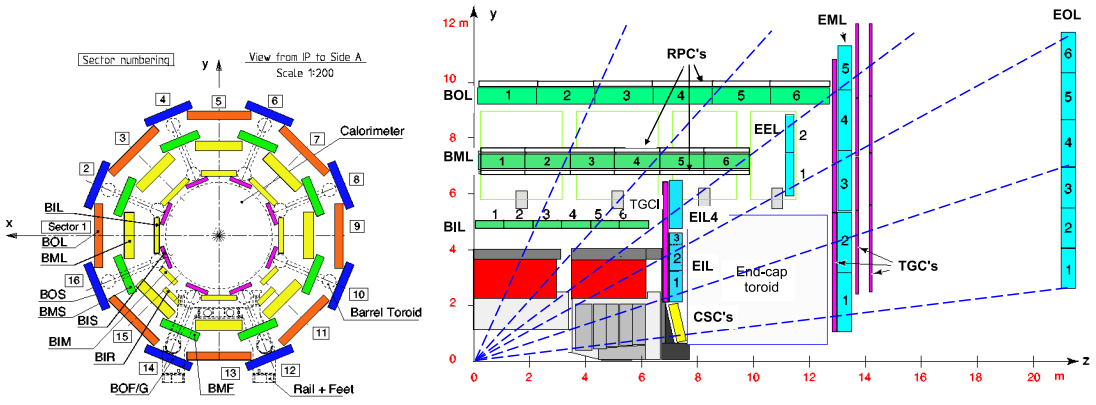

Figure 4.1: Cross sections of the muon spectrometer in the x-y plane (left) and in the y-z bending plane in the magnetic field (right).

4.1 The toroid magnets

High momentum resolution is important for the precise reconstruction of muon final states. At low p_T values, the muon momentum resolution is still dominated by multiple scattering (see Fig. 4.2) which is minimized by using air-core magnets for the muon spectrometer.

The magnet system is composed of three superconducting toroid magnets and covers the pseudorapidity range $|\eta| < 2.7$. The barrel toroid is 25 m long with an inner (outer) diameter of 9.4 (20.1) m. The end-cap toroids are placed at the ends of the barrel. They are 5 m long with an inner (outer) diameter of 1.65 (10.7) m. The toroidal magnetic fields provide a bending power of 3 Tm in the barrel and of 6 Tm in the end-caps.

4.2 The muon precision tracking chambers

The precision tracking chambers in the barrel are mounted in three cylindrical layers at radii of 5, 7.5 and 10 m. The overall coverage of the barrel detectors is $|\eta| < 1$. In the end-caps, the precision chambers are arranged in four disks at distances of 7, 10, 14 and 22 m from the interaction point. The coverage of the end-caps is $1 < |\eta| < 2.7$. The precision chambers provide uniform coverage up to $|\eta| = 2.7$ within a gap at $\eta = 0$ where cables and services for the inner detector and the calorimeters are placed.

Figure 4.2 shows the different contributions to the muon momentum resolution. At high p_T values, the chamber resolution and alignment are the dominant contribution.

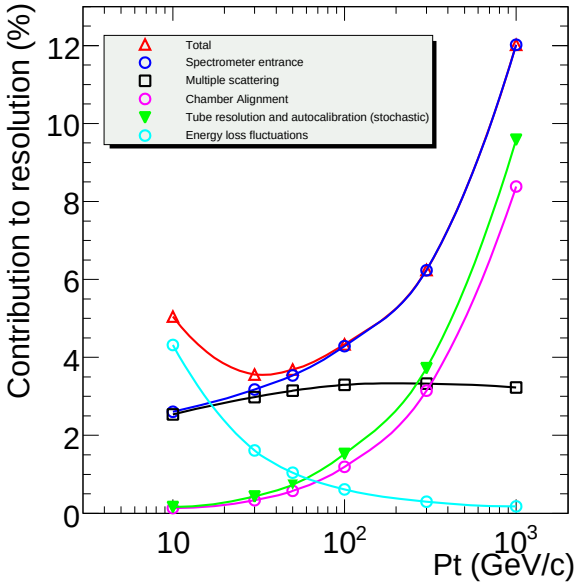

Figure 4.2: Contributions to the muon momentum resolution as a function of the transverse momentum.

4.2.1 Monitored Drift Tube (MDT) Chambers

The MDT chambers are the main muon tracking chambers both in the barrel and end-caps regions. A total of 1150 chambers covers an active area of 5500 m^2.

The basic elements of the MDT chambers are drift tubes with a diameter of 29.97 mm. The tube consists of aluminum with a wall thickness of 400 μm. The drift tubes are filled with Ar/CO_2 (93/7) gas mixture at a pressure of 3 bar. At the center of each tube, a gold-plated tungsten-rhenium anode wire of 50 μm of diameter is located at a potential of 3080 V with respect to the tube wall creating a radial electric field.

When a muon traverses the drift gas, ion-electron pairs are created along its path. Secondary ionization is caused by the electrons produced in the primary ionization. Since secondary interactions happen very close to the primary ionization, ion-electron pairs are grouped in clusters along the muon path. In the applied electric field, the electrons and ions drift towards the anode (wire) and cathode (tube wall), respectively, with average drift velocities. Near the wire, the electric field is high enough to accelerate the drifting electrons such that they ionize the Argon atoms of the gas creating an avalanche process. The electron amplification factor, the gas *gain*, depends on the gas mixture and pressure, and on the electric field strength near the wire. Since the avalanche is produced very close to the wire, the electron signal induced on the anode is very short and cannot be detected by the read-out electronics. Only the current signal induced by the secondary ions drifting from the avalanche region to the tube wall can be measured.

The determination of the position of a track in a drift tube is based on the measurement of the drift time of the primary ionization charge to the sense wire. It is defined as the time difference between the rising edge of the induced signal and the proton bunch crossing time of the LHC with corrections applied for the muon flight time from the interaction point to the muon detector and the signal propagation time along the wire. The drift time is converted into the drift radius, the distance of minimum approach between the muon trajectory and the anode wire, through the relation drift-time-space (*r-t relation*).

Gas mixture, pressure and the voltage applied to the drift tubes lead to a maximum drift time of about 700 ns. The corresponding gas gain is 2×10^4 which is chosen to prevent aging of the drift tubes.

The drift tubes are arranged in several layers grouped into two multilayers mounted on an aluminum support frame. Each multilayer contains three tube layers in the middle and outer stations and four layers in the inner stations. Figure 4.3 shows the structure of an MDT chamber.

Each drift tube is read out at one end by a low-impedance preamplifier with programmable threshold, a shaper and a discriminator. An ADC measured the integrated signal charge. The drift tubes provide an average spatial resolution of 80 μm. The corresponding chamber resolution is 35 μm.

4.2.2 Cathode Strip Chambers (CSC)

The CSCs are gas ionization chambers consisting of four layers measuring the position of charged particles via currents induced on pickup strips. They are installed in the region $2.0 < |\eta| < 2.7$

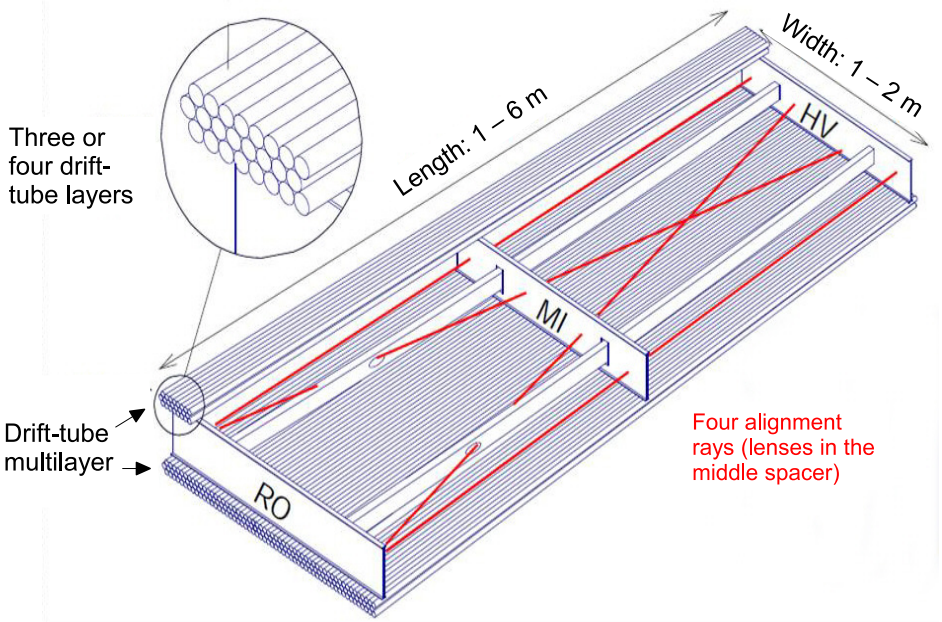

Figure 4.3: Schematics of an MDT chamber.

where the counting rate reaches 1700 Hz/cm^2. The ionization electron clusters are accelerated towards the anode wires, where the avalanche process occurs. The charge avalanche induces currents on two sets of cathode strips (192 strips orthogonal and 48 strips parallel to the wires) for each chamber. Each strip carries a fraction of the total induced current. The centroid of the charge of the affected adjacent strips measures the track coordinate. The drift time is 30 ns. Spatial resolutions of 40 μm and 5 mm are achieved in R and ϕ, respectively.

4.3 Muon trigger chambers

The trigger chambers have to fulfill the following requirements:

- Bunch crossing identification requires a time resolution of better than the LHC bunch spacing time of 25 ns.
- High momentum muons are selected using a programable p_T threshold.
- Measurement of the bending and the non-bending coordinates with a resolution of 1 cm.

The ATLAS muon spectrometer employs Resistive Plate Chambers (RPC) in the barrel and Thin Gap Chambers (TGC) in the end-caps. Figure 4.4 shows the ATLAS muon trigger scheme.
In the barrel region ($|\eta| < 1.05$), three layers of RPCs are used, two (RPC1 and RPC2) beneath and above the MDT chambers in the middle stations and the third (RPC3) together with the outer MDT chambers. The trigger requires coincidences within predefined regions pointing to

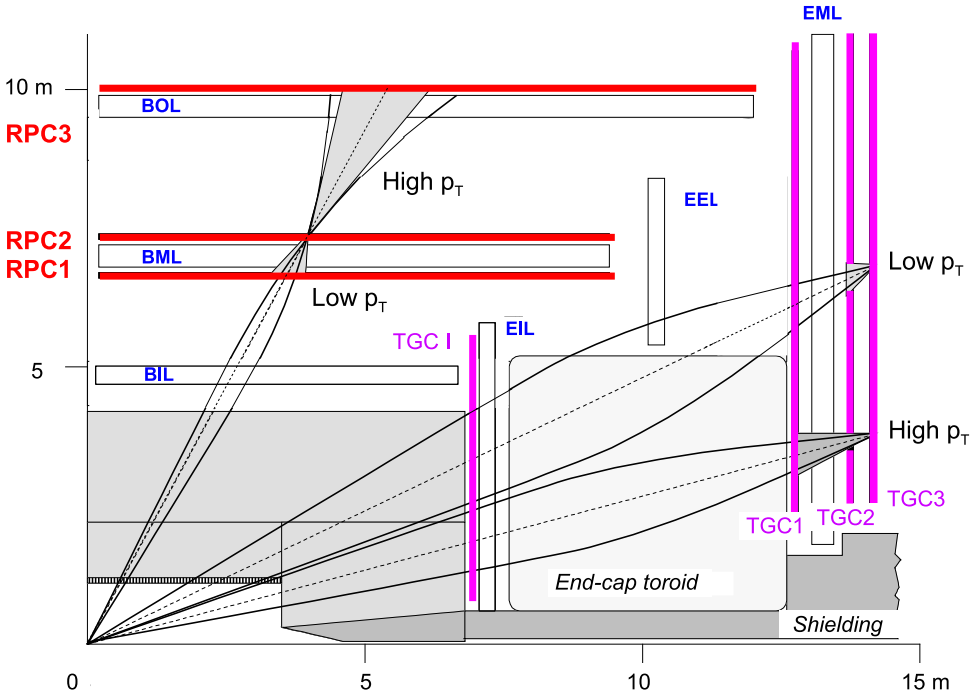

Figure 4.4: The ATLAS muon trigger scheme.

the interaction region in both projections: coincidences in RPC1 and RPC2 for the low p_T trigger and with RPC3 in addition for the high p_T trigger. In the end-cap region ($1.05 < |\eta| < 2.4$), three TGC trigger layers are installed in the middle chamber layer. The TGC layer in the inner end-cap layer is not used for the muon trigger but only for the measurement of the second coordinate.

Table 4.1 shows the performance of the four different sub-systems in the muon spectrometer. Precision and trigger chambers provide the measurement of the position of muon tracks with good resolution in three dimensions.

Table 4.1: Performance of the chambers in the muon spectrometer.

Type	Function	Chamber resolution			Measurements/track		Number of
		z/R	ϕ	Time	Barrel	End-cap	chambers
MDT	tracking	35 μm (z)	-	-	20	20	1150
CSC	tracking	40 μm (R)	5 mm	7 ns	-	4	32
RPC	trigger	10 mm (z)	10 mm	1.5 ns	6	-	606
TGC	trigger	2-6 mm (R)	3-7 mm	4 ns	-	9	3588

4.3.1 Resistive Plate Chambers (RPC)

The RPCs consist of a gas gap between two resistive Bakelite plates at a relative potential of 9.8 kV covered by two orthogonal series of pick-up strips. The η strips run parallel to the MDT wires and measure the track bending coordinate. The ϕ strips are orthogonal to the wires and provide the second coordinate.

The two Bakelite plates of 2 mm thickness are kept parallel using polycarbonate spacers of 12 mm diameter and 2 mm thickness. The gas mixture is $C_2H_2F_4$/Iso-C_4H_{10}/SF_6 (94.7/5/0.3). A uniform electric field of 4.9 kV/mm creates a discharge for a passing muon track.

4.3.2 Thin Gap Chambers (TGC)

The TGCs are multi-wire proportional chambers operating in saturation mode at a voltage of 2.9 kV. The distance between the wires is larger than the cathode-to-anode distance like in the CSCs. The wire-to-wire distance is 1.4 mm. The gas used is a mixture of 55% CO_2 and 45% n-C_5H_{12} (n-pentane). The anode wires are arranged parallel to the MDT wires. Pickup strips provide the trigger information and the measurement of the non-bending coordinate.

Chapter 5

Reconstruction of physics observables

In this chapter, the main observables used for the ATLAS data analyses are described. Main emphasis is given to observables relevant for the $Z \to \tau\tau$ event selection.

5.1 Monte Carlo event generators and detector simulation

Several Monte Carlo generators are available to generate the physics processes as input for the ATLAS detector simulation. The simulation of physics processes in proton-proton collisions starts with the simulation of the hard scattering process followed by parton showering and the hadronization. In addition to the primary hard interaction also the underlying event, i.e. interactions between the proton-remnants, are simulated. The events generated by the Monte Carlo generators are passed through the detailed simulation of the ATLAS [30] detector based on the GEANT4 [31] package for the description of the detector response.

Three Monte Carlo generators are employed for the analysis:

PYTHIA [32] is a general-purpose leading order (LO) generator for interactions in proton-proton collisions. This generator includes leading order matrix elements and simulates initial and final state QCD radiation as well as the underlying event and hadronization.

MC@NLO [33] is a Fortran package which combines a Monte Carlo event generator including next to leading order (NLO) corrections for QCD processes. MC@NLO makes use of the Fortran HERWIG event generator [34] for the simulation of parton shower and hadronization processes.

ALPGEN [35] is a leading-order generator for physics processes at hadron colliders involving multi-parton interactions.

5.2 Pile-up simulation

The cross section for inelastic pp interactions at the LHC at the center-of-mass energy of 7 TeV is 70 mb [36]. At the design luminosity of 10^{34} $cm^{-2}s^{-1}$, the average number of minimum-bias events per bunch crossing is 23. Most of the particles produced in such interactions do not come from interesting physics processes. Due to the large number of protons per bunch, at each bunch crossing multiple inelastic pp interactions overlay the interesting physics processes selected by the trigger system. This effect is referred to as in-time pile-up.

The average number of interactions per bunch crossing scales linearly with the luminosity. In addition, the electronic signals are integrated over several bunch crossings leading to the so called out-of-time pileup. The out-of-time pile-up depends on the time between bunch crossings and on the electronic integration times which differs for the different detector subsystems.

The effect of the in-time pile-up increases the observed energy measured in the calorimeters. The out-of-time pileup decreases the observed energy in the calorimeters, due to the negative tail in the LAr pulse shape and also increases the noise.

Usually, Monte Carlo samples are produced before or during a given data taking period. By that design, only a best-guess of the data pileup conditions can be put into the simulation. Since 2011 data taking, LHC is running with bunch trains with an in-train bunch separation of 50 ns, then also the out-of-time pile-up effect needs to be taken into account.

At the analysis level, simulated events need to be re-weighted according to the pile-up conditions found in data. The commonly used variables for the re-weighting procedure in Monte Carlo are:

- number of primary vertices to measure the activity in the current bunch-crossing: sensitive only to in-time pileup.
- average interaction per bunch-crossing (μ) calculated from luminosity for each luminosity block (LB): average of in-time and out-of-time pileup. The μ value is calculated with the average across all bunch crossing IDs (BCIDs) in the LB. An alternative procedure calculates the μ values for each BCID.

5.3 Particle reconstruction and identification

5.3.1 Electrons

Reconstruction and identification of electrons is needed in many physics analyses. A good understanding of the combined performance of the inner detector and calorimeters allows a good rejection against jets and background electrons from photon conversion. The definition of electrons is performed in two steps: reconstruction of the electron track and calorimeter deposition and identification. Three different algorithms have been developed for the electron reconstruction. The main algorithm is dedicated to high p_T isolated electrons and requires measurements both in the inner detector and LAr calorimeter. A second algorithm is mostly dedicated to low p_T electrons and electrons in jets. This algorithm is seeded by inner detector

tracks. The third algorithm is used for the reconstruction of forward electrons where no track matching is required due to the limited coverage of the inner detector.

In the following, only the first algorithm is described, since this is used for the electron selection in the $Z \to \tau\tau$ analysis presented in this thesis.

Reconstruction The main reconstruction algorithm for isolated electrons is based on clusters in the electromagnetic calorimeter associated to tracks reconstructed in the inner detector. Seed clusters with energies greater than 2.5 GeV are formed by a sliding window algorithm. A window of size $N_\eta \times N_\phi$ (3×5) cells is slid across the η-ϕ grid of the LAr calorimeter to find energy depositions above a predefined threshold. Those seeds are used to build clusters by scanning the calorimeter layers for associated energy deposits and determining their energy and position. Reconstructed tracks are matched to the seed clusters by extrapolating the last point measured in the inner detector to the second layer of the LAr calorimeter. The match is performed comparing η and ϕ coordinates of the track and cluster candidates. If the track candidate has no hits in the silicon tracker, the match with the cluster is performed only in the ϕ coordinate, since the η coordinate measured by the TRT is not accurate enough. Matching tracks and clusters are considered as electron candidates. The electromagnetic cluster is then redetermined using a 3×7 (5×5) sliding window in the barrel (end-cap). The energy of the electron candidate is calculated as the weighted average of the cluster energy and the observed track momentum. The ϕ and η are taken from the track parameters. If there is no silicon detector hits, the η coordinate is taken from the reconstructed cluster position.

Identification The identification procedure aims at a good separation of isolated electrons and jets (faking electrons). The variables used for the identification are taken from track and cluster parameters. According to the signal efficiency and background rejection required for specific physics analyses, loose, medium or tight selection criteria are used. The loose identification is performed using the shower profile of the cluster in the second layer of the calorimeters and the energy deposition leakage into the hadronic calorimeter. The medium identification uses in addition information from the first layer of the calorimeter and track quality and tighter track-cluster matching requirements. The tight selection further applies cuts on the ratio between the energy deposition in the calorimeter and the momentum of the electron track and requires b-layer hits and the electron identification in the TRT using multivariate analysis methods.

Details on the electron identification together with performance of the identification algorithms can be found in [37].

5.3.2 Muons

The ATLAS muon spectrometer is designed to reconstruct and identify muons with better than 95% efficiency over a wide transverse momentum and solid angle range ($|\eta| < 2.7$) and with a muon momentum resolution of better than 10% for transverse momenta up to 1 TeV.

The so-called stand-alone muon reconstruction uses only track segments in the muon spectrometer up to $|\eta| < 2.7$. The muon trajectory in the bending plane (R-η) is calculated from

the hits in the precision chambers. The direction of flight and the impact parameter at the interaction point are determined by extrapolation of the measured track to the beam axis taking into account the multiple scattering in the calorimeters.

The so-called combined reconstruction starts from tracks measured independently in the inner detector and in the muon spectrometer. The parameters of the combined muon tracks are a statistical combination of the inner detector and the muon spectrometer track parameters. The acceptance for the combined muon reconstruction is limited to the acceptance of the inner detector ($|\eta| < 2.5$).

So-called segment tagged muon tracks are inner detector tracks to which track segments in the muon spectrometer can be associated. This method extends the muon acceptance to detector regions where the stand-alone reconstruction is difficult and lower momenta.

Calorimeter tagged muons are defined as inner detector tracks with energy deposition in the calorimeters compatible with that of a minimum ionizing particle. This method improves the muon reconstruction efficiency in the acceptance gap at $\eta = 0$ (for services for the inner detector and calorimeters).

Two reconstruction algorithms exist for the track reconstruction in the muon spectrometer which use different pattern recognition strategies and different definition of combined tracks.

The reconstruction of muon tracks starts in the first case with track segments reconstructed in the muon precision chambers. The coordinates in the bending plane are measured by the precision chambers while the trigger chambers measure the ϕ coordinate. If more than two segments are found in different layers in a η-ϕ region of interest (RoI), a stand-alone muon track is reconstructed which is then extrapolated to the interaction point and combined with a matching inner detector track [38]. In the second algorithm, global pattern recognition is performed in the full muon spectrometer using Hough transformations [39] in the bending and the non-bending plane. The two patterns are combined and track segments are formed compatible with a curved track. Combined tracks are determined from a global fit to inner detector and muon spectrometer hits belonging to the identified track candidates.

5.3.3 Jets

The ATLAS calorimeters have high granularity (about 187000 cells) and high particle stopping power over the whole detector acceptance. The reconstruction of hadron jets starts from the energy deposits in the calorimeter cells. The cell energies are adjusted to the electromagnetic energy scale (EM) to correctly reproduce the energy deposition of electrons and photons as determined from test beam measurements. Additional corrections are needed to reproduce the energy deposition of jets.

The cell energies are connected to a three dimensional topological calorimeter clusters representing the full energy deposit of the particles in the calorimeter. For the seed of the cluster a signal-to-noise ratio $\Gamma > 4$ is required. Neighboring cells with $\Gamma > 2$ are associated to the clusters. Remaining cells close to the cluster with $\Gamma > 0$ are associated to the seed too.

Several algorithms are used to reconstruct jets from topological clusters. The anti-k_T algorithm [40] is used by the ATLAS Collaboration.

5.3.4 Hadronic τ decays

The mean lifetime of τ leptons is 2.9 x 10^{-13} seconds, corresponding to a mean free path ($c\tau$) lower than 100 μm. The branching fraction for τ decays into hadrons and ν_τ is 65%, the remaining 35% of the decays are into muons or electrons and neutrinos [14]. Hadronic τ decays can be divided in 1-prong and 3-prong final states depending on the number of charged pions in the decay.

The reconstruction and identification of hadronic τ decays is challenging at hadron colliders due to confusion with hadron jets. The probability that jets are misidentified as hadronic τ decays is significant and needs to be understood very well since jets production in proton-proton collisions has a much higher cross section than electroweak processes producing τ leptons.

Several properties allow to distinguish hadronic τ decay candidates from jets: low track multiplicity and relatively narrow clustering of tracks and energy deposition in the calorimeters.

The selection of hadronic τ decays is performed in two steps. First the reconstruction of the τ jets from the calorimeter and inner tracker information then the identification of the τ candidates and the discrimination against the background (mainly hadron jets).

Reconstruction of τ jets Hadronic τ decays are reconstructed from jets reconstructed in the calorimeters using the anti-k_T algorithm [40] within a cone of radius $\Delta R = 0.4$ in the η-ϕ plane. Inner detector tracks are associated to the calorimeter clusters if their distance from the axis of the seed jet is less than $\Delta R = 0.2$. Quality criteria are applied to each track associated to the seed jet:

- $p_T > 1$ GeV,
- number of pixel detector b-layer hits ≥ 1,
- number of pixel detector hits ≥ 2,
- number of pixel detector hits + number of SCT hits ≥ 7,
- $|d_0| < 1.0$ mm,
- $|z_0 sin\theta| < 1.5$ mm,

where d_0 (z_0) is the transverse (longitudinal) distance of closest approach of the track to the primary vertex.

The pseudorapidity η and the azimuthal angle ϕ of the hadronic τ candidates are calculated from the seed jet. The energy of the τ candidate is determined as the sum of the uncalibrated cell energies (EM scale) of the topological clusters of the seed jet within $\Delta R = 0.4$. The energy calibration is performed by applying corrections with the response function, determined from Monte Carlo simulation

$$R(p_T^{EM}) = \frac{p_T^{EM}}{p_T^{gen}}$$

where p_T^{gen} is the transverse momentum of the generated τ lepton and p_T^{EM} the reconstructed transverse momentum of the τ candidate at the EM scale. The corrected transverse momentum p_T^{TES} is then calculated as

$$p_T^{TES} = \frac{1}{R(p_T^{EM})} p_T^{EM}.$$

Several discriminating variables are used for τ identification combining information from the inner detector and the calorimeters.

In the following, only the variables used in Chapter 7 are defined (the complete set of discriminating variables used for the hadronic τ identification is given in [41]):

- **The electromagnetic radius** is defined as the transverse energy-weighted shower width in the electromagnetic calorimeter:

$$R_{EM} = \frac{\sum_i^{\Delta R_i<0.4} E_{T,i} \Delta R_i}{\sum_i^{\Delta R_i<0.4} E_{T,i}}. \tag{5.1}$$

  The index i runs over the cells of the first three layers of the EM calorimeter (pre-sampler, layer 1 and layer 2), within a cone of radius $\Delta R = 0.4$ around the axis of the τ candidate.

  The distribution of this variable after the selection of $Z \to \tau\tau$ events is shown in Fig. 7.16(a).

- **The track radius** is defined as the transverse momentum-weighted track width of the track associated to the τ candidate:

$$R_{track} = \frac{\sum_i^{\Delta R_i<0.4} p_{T,i} \Delta R_i}{\sum_i^{\Delta R_i<0.4} p_{T,i}}. \tag{5.2}$$

  The index i runs over the tracks of the τ candidate within a cone of radius $\Delta R = 0.4$.

  The distribution of this variable after the selection of $Z \to \tau\tau$ events is shown in Fig. 7.16(b).

- **The core energy fraction** is the fraction of the transverse energy within a cone of radius $\Delta R = 0.1$ around the axis of the hadronic τ jet in the calorimeter:

$$f_{core} = \frac{\sum_i^{\Delta R_i<0.1} E_{T,i}}{\sum_i^{\Delta R_i<0.4} E_{T,i}}. \tag{5.3}$$

  The index i runs over all cells associated to the τ candidate which are calibrated to the EM scale.

  The distribution of this variable after the selection of $Z \to \tau\tau$ events is shown in Fig. 7.16(c).

- **The leading track momentum fraction** is the ratio between the transverse momentum carried by the leading track and the transverse momentum of the τ candidate calibrated at the EM energy scale:

$$f_{track} = \frac{p_{T,1}^{track}}{p_T^{\tau}}. \tag{5.4}$$

The distribution of this variable after the selection of $Z \rightarrow \tau\tau$ events is shown in Fig. 7.16(d).

- **The electromagnetic fraction** is the transverse energy fraction deposited in the EM calorimeter:

$$f_{EM} = \frac{\sum_i^{\Delta R_i<0.4} E_{T,i}}{\sum_j^{\Delta R_j<0.4} E_{T,j}}. \tag{5.5}$$

The index i runs over the cells of the EM calorimeter. The index j runs over all the cells of the calorimeters.

τ identification Once a τ candidate is reconstructed, the τ identification procedure is performed since hadron jets represent a significant background even after the reconstruction step. The performance of the τ identification is evaluated in terms of efficiency and jet rejection rate. Three identification methods are in use: simple cut-based selection, projective likelihood identification and identification using boosted decision trees (BDTs). The identification of reconstructed τ candidates is performed separately for 1-prong and multi-prong candidates.

- The cut-based identification was mainly used during the initial phase of ATLAS data analysis since this method relies on well controlled variables with low systematic uncertainties: R_{EM}, R_{track} and f_{track}. The cut values are parametrized as a function of $\mathrm{p_T}$ of the τ candidate (corresponding to loose, medium or tight identification) and depend on the signal efficiency desired for a specific physics analysis.

- The projective likelihood function L used for the τ identification is the product of the probability density functions $p_i(x_i)$ of N discriminating variables x_i

$$L = \prod_{i=1}^{N} p_i(x_i)$$

and defined for both signal and background τ candidates. The logarithmic of the ratio of the likelihood functions of signal and background is used as discriminant:

$$d = ln\left(\frac{L_S}{L_B}\right) = \sum_{i=1}^{N} ln\left(\frac{p_i^S(x_i)}{p_i^B(x_i)}\right).$$

The likelihood functions are determined depending on the τ $\mathrm{p_T}$ ($\mathrm{p_T} < 45$, 45-100, > 100 GeV), the track multiplicity (1-prong or multi-prong), track quality criteria (with or without a track with $\mathrm{p_T} > 6$ GeV) and on the pileup conditions. In order to reduce the systematic uncertainties, not all discriminating variables are included in the likelihood function.

Some of the variables are correlated and introduce systematic errors without significant improvement of the jet rejection. Only three variables are used for the identification of 1-prong and five variables for multi-prong τ candidates.

- The boosted decision tree (BDT) method [42] is a multivariate technique optimizing simultaneously selection cuts in a series of observables in order to classify events as signal or background. A decision tree [43] can effectively find a continuous cut separating the signal region in the multidimensional space of the discriminating variables. Candidates that do not pass a certain set of cuts are not discarded but are further processed by the algorithm. A tree is built by training on signal and background samples. At the beginning, all data are on one node (*root* node). The best discriminating variable is found and applied at the root node. At this step, two nodes (called *leaves*) are created. A second discriminating variable is applied on these new nodes: the process is repeated on these new nodes until a stopping condition is satisfied (desired purity or, in this case, a minimum number of τ candidates contained in the leaf). The response of the decision tree is then the signal purity of the leaf node. Further, "boosted", decision trees are used to increase the purity of the sample by increasing the weights of the misclassified candidates and modifying the selection cuts. At the end of the training procedure a score between 0 and 1 is assigned to each leaf depending on its number of signal and background events. Background events have low BDT scores while high BDT scores more likely correspond to signal events. BDT for jet rejection are trained separately for 1-prong and 3-prong τ candidates. In addition, BDT are trained for different pileup conditions. In order to compensate the p_T dependence of the discriminating variables used for the decision tree, the cut values are parametrized as a function of the transverse momentum. The cut on the BDT score is set to achieve an identification efficiency of τ candidates of 60%-45%-30% corresponding to loose-medium-tight selection.

The performance of the three identification methods is compared in Fig. 5.1.

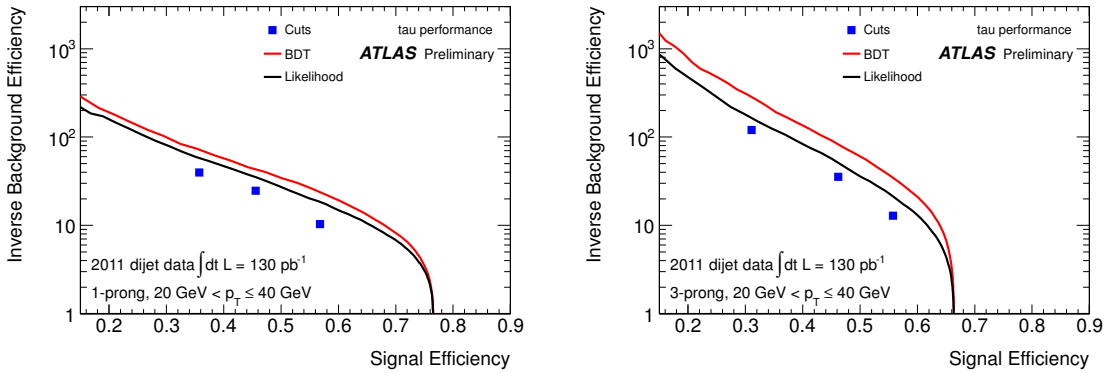

Figure 5.1: Jet rejection (inverse background efficiency) as a function of the signal efficiency for different τ identification of 1-prong and 3-prong τ candidates [41].

5.3.5 Missing transverse energy

The missing transverse energy is equal to the total transverse energy reconstructed from the energy deposits in the calorimeter taking into account reconstructed muon tracks. By definition, $\sum \vec{p}_T^{\,miss}$ and $\sum \vec{p}_T$ point in opposite direction in the transverse plane. The events from hard collisions contribute to the transverse energy, as well as underlying events, pileup and particles not originating from the collisions. The different contributions at a proton collider make the measurement of the transverse missing energy challenging.

The reconstruction of the missing transverse energy (E_T^{miss}) starts with the energy deposit in the calorimeter cells. It is crucial to suppress noise contribution to the energy measurement in each calorimeter cell. This is achieved by using only cells belonging to three-dimensional topological clusters for the transverse energy measurement.

The transverse momentum of isolated muons measured in the muon spectrometer has to be taken into account in the E_T^{miss} measurement. Muons contribute to the total transverse momentum balance but deposit little energy in the calorimeters. Muons are called isolated if the distance ΔR between the muon and the closest jet is greater than 0.3. The energy deposits of isolated muons in the calorimeters are subtracted from the measured transverse energy.

Chapter 6

Muon identification performance

The leptonic decays of Z and W bosons are the main processes used for understanding and measuring the detector performance. In particular, the Z decay into two muons gives an unbiased and pure sample of high-energy muons.

Muon efficiencies are determined using the so-called "tag-and-probe" method. Events are selected by applying very strict selection criteria on one of the two muons of the Z decay, the tagging muon, and loose criteria on the second, probe muon. Due to the clean signature of these events, there is only very small background. The muon reconstruction efficiency is the fraction of probe muons which can be matched to a reconstructed muon.

The description of the efficiency in collision data by the Monte Carlo simulation is evaluated by relative scale factors defined as

$$\mathrm{SF} = \frac{\epsilon_{\mathrm{data}}}{\epsilon_{\mathrm{MC}}},$$

where $\epsilon_{\mathrm{data(MC)}}$ is the efficiency measured in experimental data (Monte Carlo). Monte Carlo estimations are corrected by applying the scale factors in order to describe the data.

The subject of this chapter is the measurement of the efficiency scale factors to be applied to the Monte Carlo samples used for the $Z \rightarrow \tau\tau$ analysis. Muons can be reconstructed in ATLAS with two different algorithms: STACO and MUID. Muons for the Z$\rightarrow \tau\tau$ analysis are reconstructed with the former algorithm and the muon reconstruction performance studies in this chapter apply for the STACO algorithm although very similar performance is achieved with the MUID algorithm [44]. The muon isolation and trigger efficiencies are determined for the requirements used for the $Z \rightarrow \tau\tau$ analysis.

The muon efficiencies are measured using a part of the data collected in 2011 (periods D-H) with similar beam conditions corresponding to an integrated luminosity of 1.03 fb^{-1}. In the measurement of the muon trigger efficiency, periods I-J with an integrated luminosity of 0.52 fb^{-1} are included to test different trigger requirements, not used in previous runs.

6.1 The $Z \rightarrow \mu\mu$ tag and probe method

In this section, the tag-and-probe method used for the following efficiency measurement is described:

- The inner detector (ID) track reconstruction efficiency is defined as the fraction of probe muons (muon spectrometer tracks) that are also reconstructed in the ID.
- The muon reconstruction efficiency is defined as the fraction of probe muons (ID tracks) that are also reconstructed in the muon spectrometer and combined successfully.
- The efficiency of the muon isolation criteria is defined as the fraction of reconstructed muons that passed the isolation cuts.
- The muon trigger efficiency is defined as the fraction of reconstructed and isolated muons that fired the required trigger.

The efficiency is calculated both in data and Monte Carlo simulation. Due to the high purity of the data sample, no background subtraction to the data sample is applied.

6.1.1 Signal and background

The goal for the tag-and-probe method is to select a clean sample of muons from $Z \rightarrow \mu\mu$ decays. The following signal and background processes are taken into account (see Table 6.1):

- $Z \rightarrow \mu\mu$ signal events with two muons in the final state. If the Z boson is not boosted, the muons in the final state are produced back-to-back.
- The background contribution of $Z \rightarrow \tau\tau$ decays is strongly reduced because of the branching ratio of the $\tau \rightarrow \mu\nu\nu$ decays of 0.17.
- The cross section for $W \rightarrow \mu\nu$ background production is one order of magnitude higher than for $Z \rightarrow \mu\mu$ production. In this case, the tag is a real muon while the probe is a non-isolated muon from jets in underlying events.
- The $W \rightarrow \tau\nu$ background is again reduced due to the $\tau \rightarrow \mu\nu\nu$ branching ratio. Also in this case, the tag is a real muon while the probe is a non-isolated muon coming from jets in underlying events.
- $b\bar{b}$ production with semileptonic decays of the two b quarks into muons is the dominant background due to the high cross section. It contributes to the selected tag-and-probe muon pairs only at low transverse momenta.
- $c\bar{c}$ production with subsequent charm decays into muons is also a dominant background due to high cross section. It contributes only at even lower transverse momenta.

- $t\bar{t}$ production with two real muons in the final state is a small background due to the relatively small cross section.

Isolation is required to reduce the multi-jet contribution. In order to reduce the $W \to \mu\nu$ background, the requirement of back-to-back muons of opposite charge is used. The Monte Carlo samples used for this analysis are generated by PYTHIA [32] followed by the full detector simulation [30]. Electroweak cross sections are scaled according to the ATLAS measurements in [45]. The cross sections for the QCD processes generated at lowest order perturbation theory are rescaled to NNLO.

Table 6.1: Signal and background processes relevant for the tag and probe method.

Dataset	Events	NNLO Cross Section [nb]
$Z \to \mu\mu$	4985129	0.99 ± 0.05
$Z \to \tau\tau$	1997042	0.99 ± 0.05
$W \to \mu\nu$	6955568	10.5 ± 0.5
$W \to \tau\nu$	998868	10.5 ± 0.5
$b\bar{b}$ ($\geq 1\mu$ with $p_T > 15$ GeV)	4473784	37.0
$c\bar{c}$ ($\geq 1\mu$ with $p_T > 15$ GeV)	1498511	14.2
$t\bar{t}$	198870	0.16 ± 0.01

6.1.2 Tag and probe selection

In this section, the selection criteria of the tag-and-probe method are described. The selection is performed in four steps: selection of collision events, tag selection, probe selection, muon matching.

All tracks in the ID measurements are required to have a minimum number of hits in the silicon detectors to suppress fake tracks and discriminate against muons from hadron decays. Dead or missing sensors crossed by a track are counted as hits. At least 1 hit in the b-layer, if within the acceptance, and the sum of hits in the pixel detector to be greater than 1 is required. The number of SCT hits has to be greater than 5 while the sum of missing pixel and SCT hits on the track (holes) has to be less then 3. A successful extension of the muon trajectory into the TRT, within the geometrical acceptance, is required based on the number of associated good TRT hits and outliers.

Collision event selection Events are used in runs where the ID, the muon spectrometer and the magnet systems were fully operational. They have to pass the single muon trigger with $p_T > 20$ GeV at the Event Filter level. A reconstructed primary vertex with at least three associated tracks is required.

Tag muon definition The tag muon track is required to be a combined muon track. Several requirements are used to reduce fake muons and non-isolated muons (mainly from pion decays):

Table 6.2: Inner detector track quality requirements.

b-layer	N hit > 0 within acceptance
Pixel detector hits	N(hit) ≥ 2
SCT hits	N(hit) ≥ 6
Pixel detector and SCT holes hits	pixel N(holes) + SCT N(holes) ≤ 2
TRT requirements: $\eta \leq 1.9$	(Hit + Outliers) > 5 , $\frac{\text{outliers}}{\text{hits + outliers}} < 0.9$
TRT requirements: $\eta > 1.9$	if (Hit + Outliers > 5) : $\frac{\text{outliers}}{\text{hits + outliers}} < 0.9$

high transverse momentum $p_T > 20$ GeV within the acceptance of the muon trigger ($|\eta| < 2.4$). The reconstructed muon has to point to the primary vertex within 10 mm along the beam axis.

The associated inner detector track has to fulfill the ID track quality criteria summarized in Table 6.2. *Loose* isolation criteria are used to reduce the QCD background. The sum of the transverse momenta of the inner detector tracks within a cone of $\Delta R = 0.4$ around the track axis relative to the momentum of the selected muon track, is required to be less than 0.2. The reconstruction efficiency is independent of the isolation cut as was confirmed by varying the isolation requirement. The tag muon selection requirements are summarized in Table 6.3.

Table 6.3: Selection criteria for the tag muon.

Tag muon selection	
Kinematical requirements	$p_T \geq 20$ GeV, $\|\eta\| \leq 2.4$, $\|z_0\| < 10$ mm
ID track quality requirements	see Table 6.2
Loose Isolation	$\sum_{\Delta R=0.4} p_T^{ID}/p_T < 0.2$
Trigger requirement	$p_T \geq 20$ GeV at Event Filter level

Probe muon definition The probe muon is required together with a tag muon. It can be a tagged inner detector, a standalone or a combined muon track: the muon reconstruction efficiency is measured with respect to ID tracks (see sections 6.2.2 and 6.2.3) and MS tracks (see section 6.2.1) while the isolation cut and trigger efficiencies are measured with respect to the reconstructed muon tracks (see sections 6.3 and 6.4). Loose cuts are applied to the probe muons to avoid bias in the efficiency measurement.

In Table 6.4, the selection cuts applied to the different types of probe muons are shown. The kinematical cuts select probe muon tracks with high transverse momentum $p_T > 20$ GeV and $|\eta| < 2.4$ pointing to the primary vertex within 10 mm along the beam axis. The criteria of the tag and probe association are given in Table 6.4.

Figure 6.1 shows the invariant mass distribution of the tag and inner detector probe muon pairs after different selection criteria.

Muon matching The investigated muon tracks are matched with the probe muons by requiring the same charge and small spatial distance ΔR between them.

Table 6.4: Selection of probe muons.

Inner Detector probe muon	
Kinematical requirements	$p_T \geq 20$ GeV, $\lvert\eta\rvert \leq 2.4$, $\lvert z_0\rvert < 10$ mm
Loose Isolation	$\sum_{\Delta R=0.4} p_T^{ID}/p_T < 0.2$
ID track quality requirements	
Opposite charge	$q_{tag} \cdot q_{probe} < 0$
Opening angle (tag, probe)	$\Delta\phi > 2.0$
Dimuon invariant mass	$\lvert M_Z - M_{TP}\rvert < 10$ GeV
Common vertex (tag, probe)	
Muon Spectrometer probe muon	
Kinematical requirement s	$p_T \geq 20$ GeV, $\lvert\eta\rvert \leq 2.4$, $\lvert z_0\rvert < 10$ mm
Opposite charge	$q_{tag} \cdot q_{probe} < 0$
Opening angle (tag, probe)	$\Delta\phi > 2.0$
Dimuon invariant mass	$\lvert M_Z - M_{TP}\rvert < 10$ GeV
Common vertex (tag, probe)	
Combined probe selection	
Kinematical requirements	$p_T \geq 15$ GeV, $\lvert\eta\rvert \leq 2.4$, $\lvert z_0\rvert < 10$ mm
ID track quality requirements	
Opposite charge	$q_{tag} \cdot q_{probe} < 0$
Opening angle (tag, probe)	$\Delta\phi > 2.0$
Dimuon invariant mass	$\lvert M_Z - M_{TP}\rvert < 10$ GeV
Common vertex (tag, probe)	

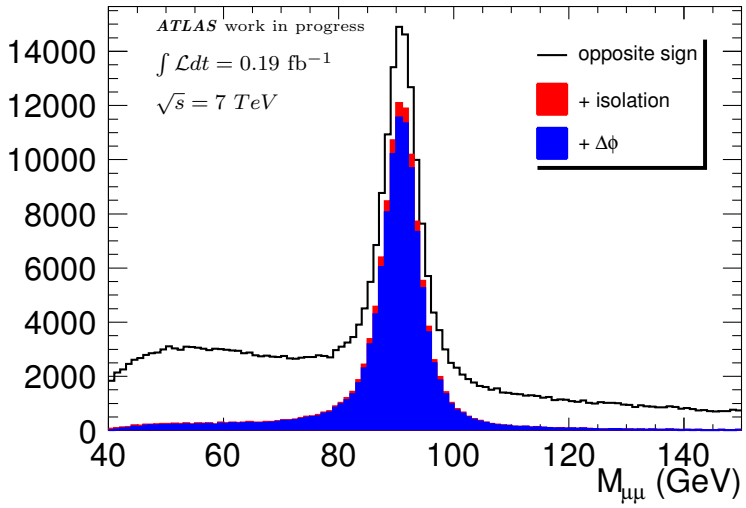

Figure 6.1: The invariant mass distribution for tag and ID probe muons in collision data after the full selection criteria for the tag muon and using only the opposite charge requirement for the probe muon (black), after additional probe isolation requirement (red) and after the additional $\Delta\phi$ cut on the tag and probe association (blue).

6.2 Muon reconstruction and identification efficiency

In this section, the results of the tag-and-probe method applied for the muon efficiency measurements are shown. The muon reconstruction efficiency is the product of three efficiencies, namely:

- Reconstruction efficiency ϵ_{ID} of the inner detector tracks,
- reconstruction efficiency ϵ_{MS} of the muon spectrometer tracks (stand-alone reconstruction),
- efficiency ϵ_{comb} of the combination of ID tracks with MS tracks (combined muon tracks).

The reconstruction efficiency is determined in ten regions in η and ϕ (see Fig. 6.2):

- Large barrel sectors.
- Small barrel sectors.
- Overlap between small and large barrel sectors.
- The region of the detector feet not covered with chambers which makes the muon reconstruction more difficult.
- The transition region between barrel and endcap MS.
- Small endcap sectors with MDT chambers.
- Large endcap sectors with MDT chambers.
- Sectors containing BEE chambers mounted on the endcap toroid cryostat without optical alignment sensors.
- Large endcap sectors with CSC chambers (outside of the TRT acceptance).
- Small endcap sectors with CSC chambers (outside of the TRT acceptance).

6.2.1 Measurement of the reconstruction efficiency of inner detector tracks

The ID track reconstruction efficiency is measured with the tag-and-probe method with respect to MS tracks. The selection criteria of the muon spectrometer probe muons are given in Table 6.4. Tracks reconstructed in the inner detector (see the quality cuts defined in Table 6.2) have to match MS tracks within $\Delta R = 0.05$ and with the same electric charge.

Table 6.5 shows the number of probe muons in signal and background events: the number of muons from Monte Carlo simulation is normalized to the data sample. Figure 6.3 shows the transverse momentum distribution of the probe muons. The observed p_T spectrum is well

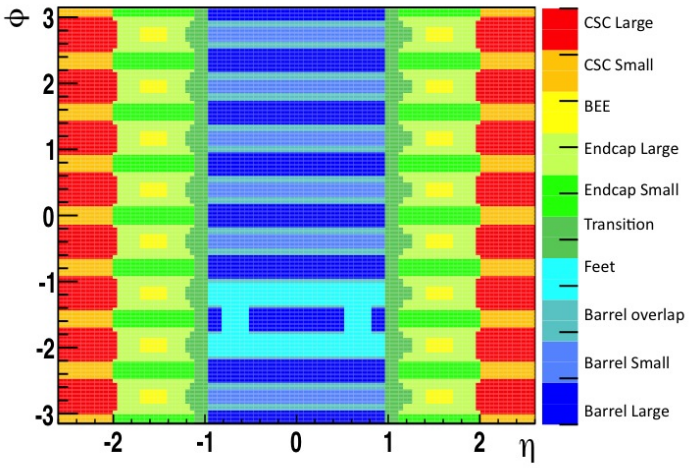

Figure 6.2: η-ϕ regions in the muon spectrometer defined by the same color for the muon efficiency measurement.

reproduced by the Monte Carlo simulation. The largest background is from $t\bar{t}$ events with two real muons in the final state.

Table 6.5: Number of muon spectrometer probe muons in data and in the Monte Carlo simulation of signal and background processes.

Process	No. probe muons
Data	670398
$Z \to \mu\mu$	670082
$Z \to \tau\tau$	69
$W \to \mu\nu$	25
$W \to \tau\nu$	0
$b\bar{b}$	64
$c\bar{c}$	30
$t\bar{t}$	129

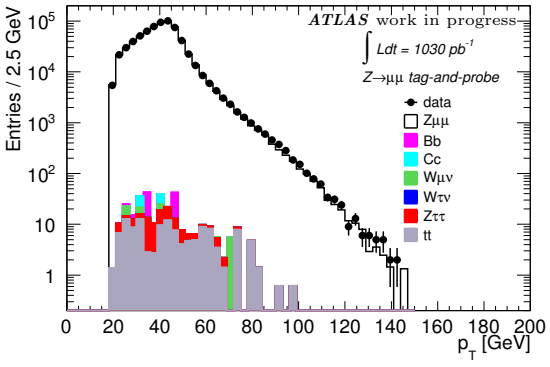

Figure 6.3: Transverse momentum distributions of MS probe muons.

In Figure 6.4, the ID track reconstruction efficiency and the corresponding scale factor is given as a function of p_T (left) and η (right). The efficiency for Monte Carlo simulation and data is independent of the transverse momentum for $p_T > 20$ GeV and varies slightly with η. The track quality requirements in Table 6.2 lower the efficiency at $\eta \approx 0$ and $|\eta| \approx 1.2$. At $\eta \approx 0$, the tracks pass through the insensitive region at the middle of the barrel TRT straws. At $|\eta| \sim 1.2$ there is a small region in the transition between the barrel and endcap of the ID where the tracks cross less than 6 SCT sensors. The Monte Carlo simulation reproduces η-variations very well: the scale factors agree with 1 within 1%.

The average efficiency (98.58 ± 0.01)% measured from collision data is slightly different from the efficiency (98.81 ± 0.01)% measured for the simulated data. The difference mainly comes from the region at $\eta > 1$.

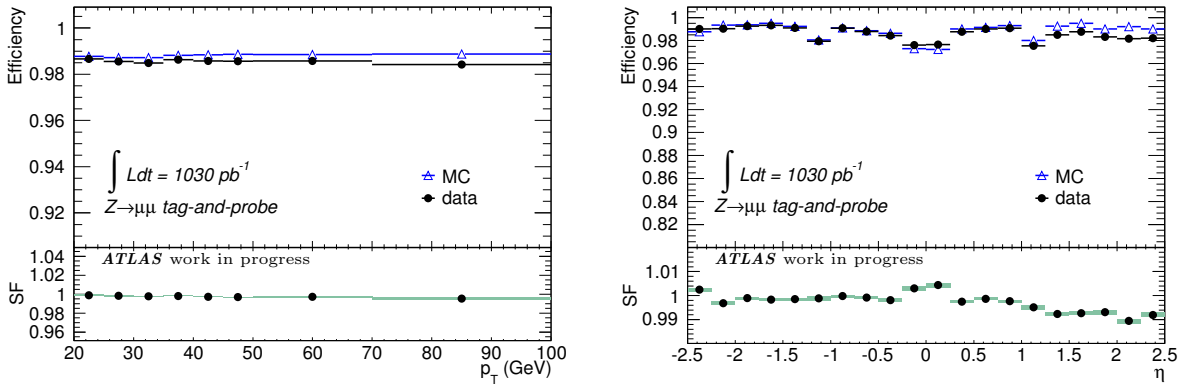

(a) Data and Monte Carlo efficiency as a function of the muon p_T.

(b) Data and Monte Carlo efficiency as a function of the η of the muon track.

Figure 6.4: Measured reconstruction efficiency of inner detector tracks from Monte Carlo simulation (blue triangles) and data (black dots) as a function of p_T and η. The corresponding scale factors (SF) between Monte Carlo simulation and data are also given.

6.2.2 Measurement of the reconstruction efficiency of combined muon tracks

The combined muon track reconstruction is used in many physics analysis since it allows for good background rejection at high efficiency. The combined muon efficiency is calculated with respect to ID probe muons selected as in Table 6.4. The matching between ID probe and the combined muons requires the same electric charge and ΔR (probe-muon) < 0.01 between the track directions.

Table 6.6 shows the number of ID probe muons for signal and background events normalized to the number of ID probe muons found in data. The efficiency measured from data is (93.04 ± 0.03)%, while the signal efficiency measured from Monte Carlo simulation is (94.87 ± 0.01)%. The total Monte Carlo efficiency including the background contributions, mostly $W \to \mu\nu$ and $b\bar{b}$ events at low p_T (see Fig. 6.5), is (94.52 ± 0.01)%.

Table 6.6: Number of inner detector probe muons in data and in Monte Carlo simulation of signal and background processes.

Process	No. probe muons
Data	626328
$Z \to \mu\mu$	623761
$Z \to \tau\tau$	150
$W \to \mu\nu$	1398
$W \to \tau\nu$	220
$b\bar{b}$	385
$c\bar{c}$	159
$t\bar{t}$	255

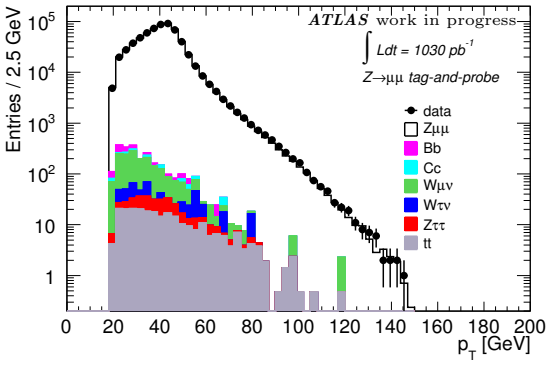

Figure 6.5: Transverse momentum distributions of ID probe muons.

The reconstruction efficiency of combined muons does not depend on the muon transverse momentum for $p_T > 20$ GeV (see Fig. 6.6a). Tag-and-probe measurements for $J/\psi \to \mu\mu$ decays showed that the muon reconstruction efficiency is independent of the transverse momentum even at lower p_T [46]. A small p_T-dependence is found at high values where the efficiency measured in data drops faster than in the Monte Carlo expectations. The reconstruction efficiency is shown for different muon spectrometer regions in Fig. 6.6c and as a function of pseudorapidity in Fig. 6.6b. The efficiency is smaller in three of the regions. In the large barrel sectors at $\eta \approx 0$, the muon spectrometer is only partially equipped with muon chambers to provide space for services for the inner detector and the calorimeters which strongly reduces the reconstruction efficiency in this region. In the transition region between barrel and endcap at $|\eta| \approx 1.2$, only one muon chamber layer is traversed by the muons due to still missing endcap chambers. The feet regions could not be fully equipped with chambers preventing stand-alone muon momentum measurement and decreasing the combined muon efficiency. The efficiency losses can be recovered by using muons which are tagged by only one muon station as described in detail in section 6.2.3. The Monte Carlo simulation reproduces the data well except for the transition region where a 5% difference in the efficiency is observed. This difference can be explained by misalignment of the muon chambers which is not taken into account in the Monte Carlo simulation.

6.2.3 Measurement of the reconstruction efficiency of segment tagged muon tracks

The efficiency of segment tagged muons is expected to be higher than for combined muons as the former include muons which do not cross enough precision chambers to form a track in the muon spectrometer. In the following efficiency measurement, segment tagged and combined muons are combined. The reconstruction efficiency measured in data is $(97.20 \pm 0.02)\%$, in good agreement with the efficiency $(97.30 \pm 0.01)\%$ measured in the Monte Carlo simulation.

In Fig. 6.7a, the reconstruction efficiency is shown as a function of the muon transverse momentum. The reconstruction efficiency is flat in both collision data and Monte Carlo simulation. The efficiency is recovered in particular in the transition region (Fig. 6.7c) where the segment-tag reconstruction allows for the reconstruction of muons with one segment station.

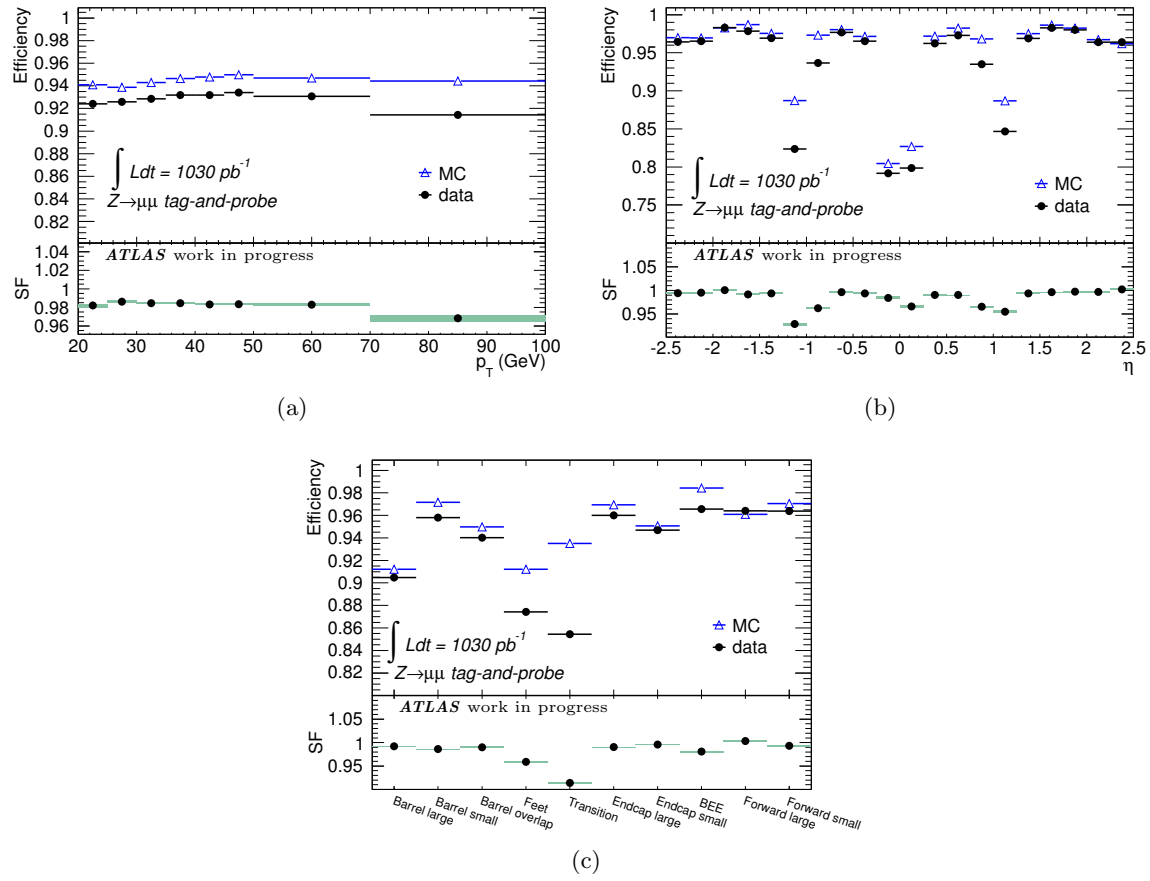

Figure 6.6: Combined muon efficiency in Monte Carlo simulation (blue triangles) and data (black dots) as a function of p_T (a) and η (b) of the muon and depending on the detector regions (c).

The agreement between data and Monte Carlo simulation is achieved in all the detector regions, with scale factors close to 1.

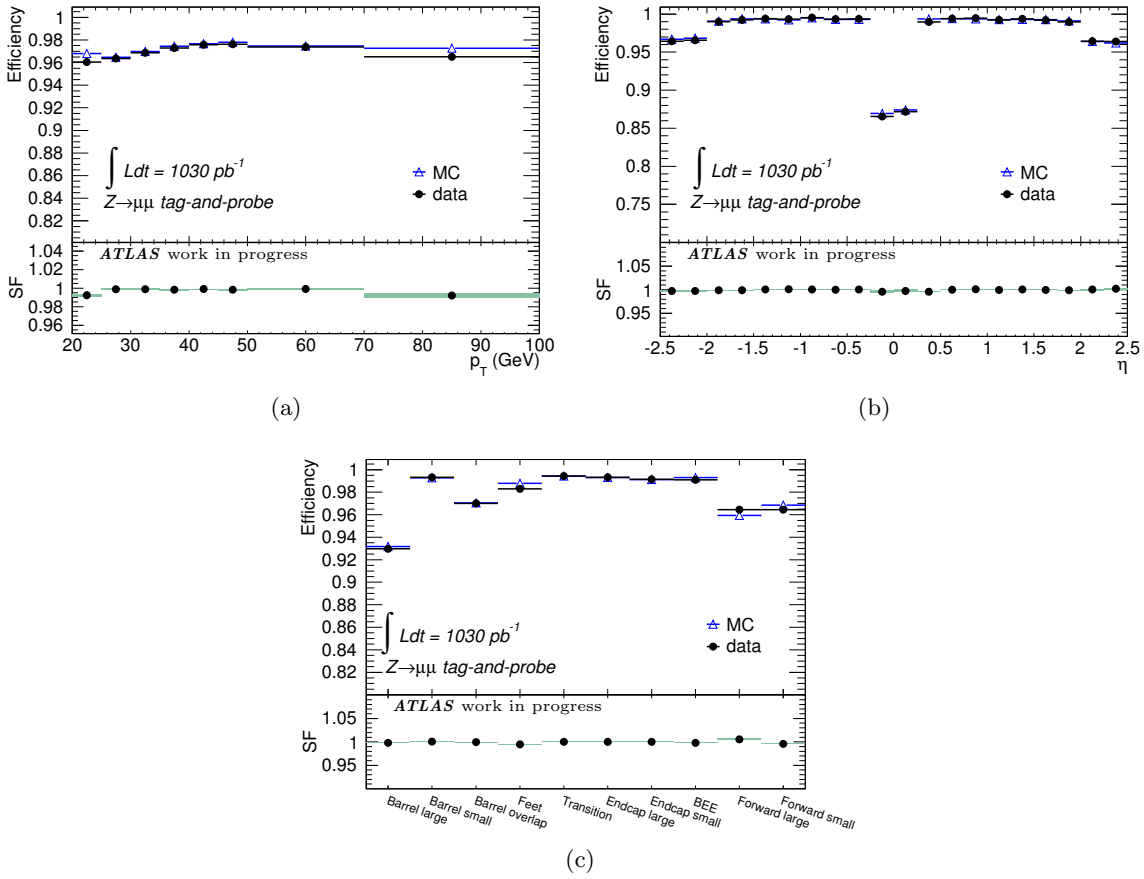

(a) (b)

(c)

Figure 6.7: Combined and segment-tagged muon efficiency in Monte Carlo simulation (blue triangles) and data (black dots) as a function of p_T (a) and η (b) of the muon and depending on the detector regions (c).

6.3 Measurement of the muon isolation efficiency

Muons from W and Z bosons are isolated, in contrast to muons arising from jets. Isolation criteria are used to suppress background. To verify the reliability of the Monte Carlo prediction on the isolation efficiency, the tag-and-probe method described in the previous section is used. The probe is a segment-tagged muon defined as in Table 6.4.

The isolation criteria for muons rely on both calorimeter and tracking variables:

- Track isolation is quantified by

$$\sum_i p_{T,i}(\Delta R = 0.4)$$

  where the sum extends over all inner detector tracks within a cone of radius $\Delta R = 0.4$ around the probe muon excluding the probe muon itself.

- Calorimeter isolation is quantified by

$$\sum_i E_{T,i}(\Delta R = 0.3)$$

  where the transverse energy deposition in the calorimeter is calculated in a cone of $\Delta R = 0.3$ around the muon direction, corrected for the muon energy loss.

Figure 6.8 shows the calorimeter isolation (left) and the track isolation (right) variables depending on the average number of interactions per bunch crossing μ (see section 5.2). Both variables depend on in-time and out-of-time pileup. The effect of the pileup is clearly visible in the calorimeter isolation variable where a shift towards higher values in $\sum_i E_{T,i}$ is observed as μ increases.

The muon isolation efficiency is defined as the fraction of reconstructed muons that satisfy the isolation cuts. The isolation cuts applied to muons to reduce the multi-jet contribution to the $Z \to \tau_\mu \tau_{\mathrm{had}}$ decays is studied in details in section 7.4.4. A combination of calorimeter and track isolation cuts are used to optimize signal efficiency and background rejection.

The muon isolation efficiency as a function of the muon $\mathrm{p_T}$ and η is shown in Fig. 6.9. The efficiency measured in the Monte Carlo simulation is slightly higher than the one determined from data. Scale factors are used to correct the Monte Carlo simulation.

The dependence of the isolation cut on the data taking periods is shown in Figure 6.10. A small decrease of the efficiency is observed in period I and J where the pile-up was largest.

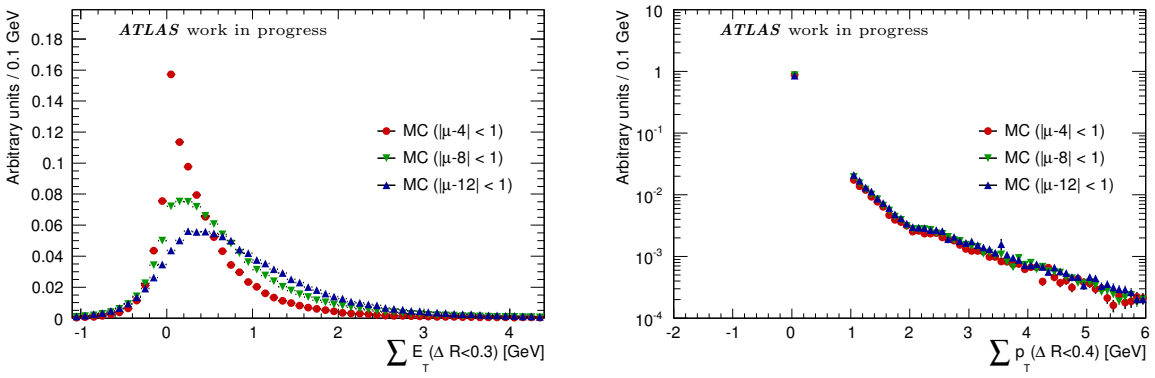

(a) Transverse calorimeter energy around the muon within $\Delta R = 0.3$.

(b) Sum of the ID transverse momenta around the muon within $\Delta R = 0.4$.

Figure 6.8: Muon isolation variables for $Z \rightarrow \mu\mu$ Monte Carlo events for different numbers of simulated average interactions per bunch crossing μ per event.

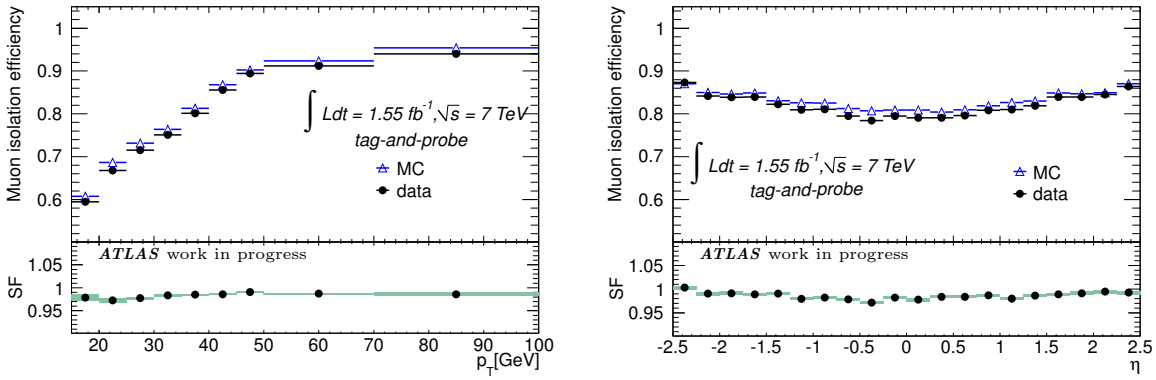

(a) Muon isolation efficiency as a function of $\mathrm{p_T}$.

(b) Muon isolation efficiency as a function of η.

Figure 6.9: Measured isolation efficiencies of reconstructed muons from Monte Carlo simulation (blue triangles) and data (black dots). Muons are isolated in this example if $\sum_i p_{T,i}(\Delta R = 0.4)/\mathrm{p_T} < 0.03$ and $\sum_i E_{T,i}(\Delta R = 0.3)/\mathrm{p_T} < 0.04$.

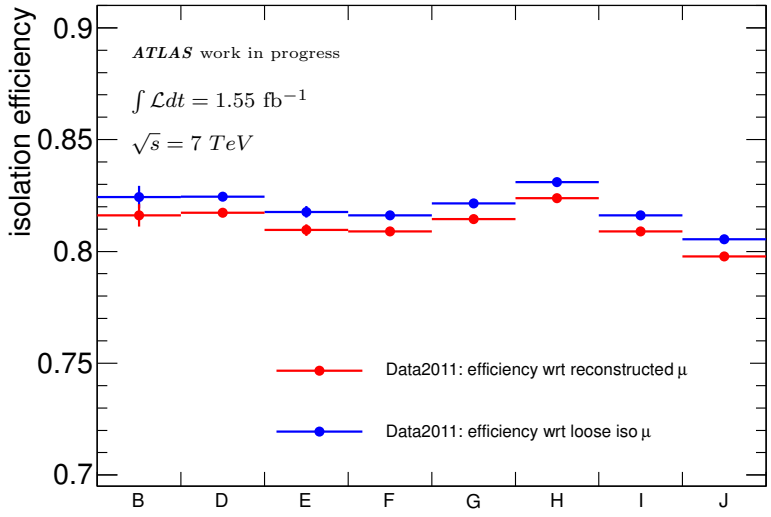

Figure 6.10: Isolation efficiency depending on the data taking periods B-J. The efficiency is calculated with respect to reconstructed and to so called loose isolated muons (defined as for the calculation of the reconstruction scale factors).

6.4 Measurement of muon trigger efficiency

The muon trigger efficiency is measured with respect to reconstructed and isolated muons with the $Z \rightarrow \mu\mu$ tag-and-probe method. The measurement shown here refers to the single-muon triggers (`EF_mu15i` and `EF_mu15i_medium`) used for the $Z \rightarrow \tau\tau$ analysis (see section 7.3.2). The triggers select at Event Filter level events with a muon with $p_T > 15$ GeV fulfilling isolation criteria[1] required by the Level 2 trigger to reduce the rate of events at the Event Filter input.

Two different triggers are used in the analysis since `EF_mu15i` was available only until period I. From period J, `EF_mu15i` was replaced by `EF_mu15i_medium` which uses a slightly tighter p_T cut at Level 1. The corresponding Level 1 trigger requirements are $p_T > 10$ GeV (`L1_MU10`) for `EF_mu15i` and $p_T > 11$ GeV (`L1_MU11`) for `EF_mu15i_medium`.

The stability of the trigger efficiency over the data taking periods is shown in Fig. 6.11(a). The trigger (`EF_mu15i`) efficiency is evaluated separately for each period. Lower efficiency is found in period B only, where matching criteria in the trigger combination were not yet optimized at the beginning of 2011 data taking.

Figure 6.11(b) shows that the trigger efficiency depends only very weakly on the pile-up conditions, i.e. the number of interactions per bunch crossing calculated independently for each luminosity block.

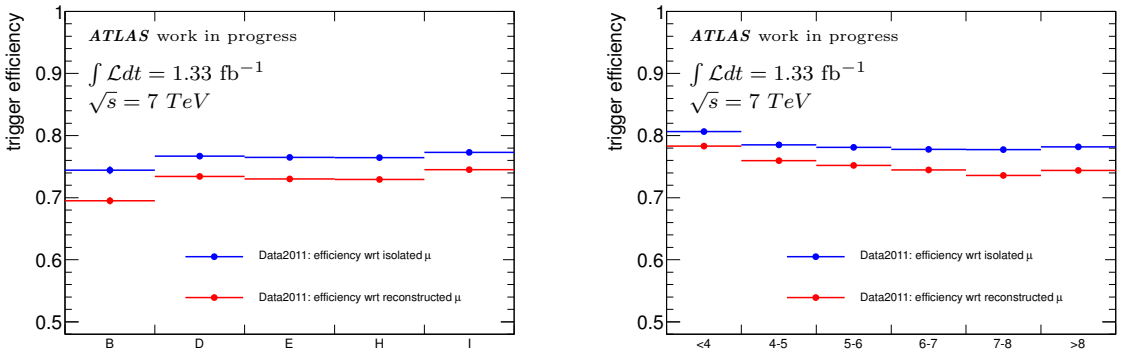

(a) Muon trigger (`EF_mu15i`) efficiency depending on the data taking period.

(b) Muon trigger (`EF_mu15i`) efficiency as a function of the average number of interactions per bunch crossing (pile-up).

Figure 6.11: Dependence of the trigger efficiency on the data taking period and on the average number of interactions per bunch crossing (μ).

Fig. 6.12 shows the trigger efficiency as a function of the muon p_T for both triggers. The efficiency reaches the plateau region for $p_T > 17$ GeV. In the plateau region, the measured efficiencies of the `EF_mu15i` and the `EF_mu15i_medium` triggers are (78.19 ± 0.05)% and (75.89 ± 0.15)%, respectively, in data, while the efficiencies are (77.76 ± 0.03)% and (74.89 ± 0.03)% in the Monte Carlo simulation.

[1] $\sum_i p_{T,i}(\Delta R = 0.2)/p_T < 0.05$ and $\sum_i E_{T,i}(\Delta R = 0.3) < 5$ GeV.

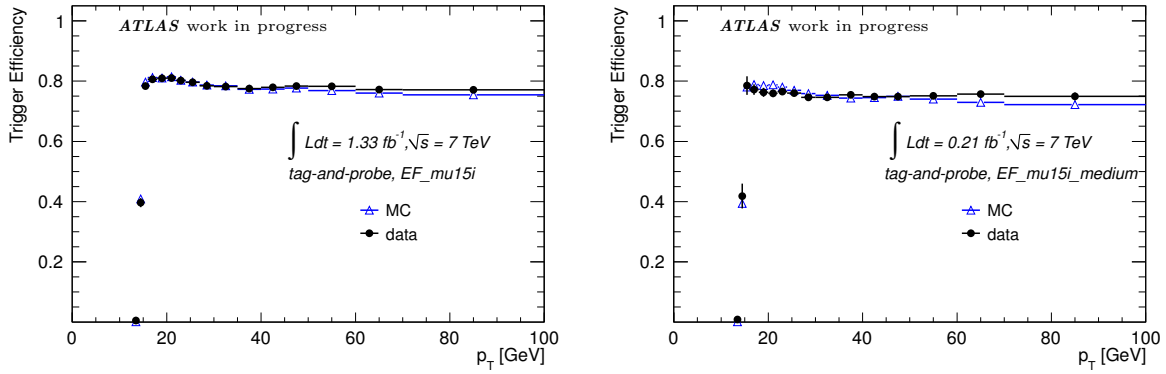

(a) `EF_mu15i` muon trigger efficiency as a function of p_T.

(b) `EF_mu15i_medium` muon trigger efficiency as a function of p_T.

Figure 6.12: Trigger efficiency as a function of the muon transverse momentum for the Monte Carlo simulation (blue triangles) and the data (black dots). The efficiency is determined with respect to reconstructed and isolated muons.

Differences between the efficiencies measured in Monte Carlo simulation and data arise in different η-ϕ regions.

Fig. 6.13 shows the η-ϕ distributions of the trigger efficiency scale factors for both triggers. The binning is adapted to particular detector regions. In particular, scale factors different from unity are observed in the barrel-endcap transition region.

Scale factors as a function of η-ϕ are used in the $Z \rightarrow \tau_\mu \tau_{\text{had}}$ analysis to correct the Monte Carlo simulation to match the collision data.

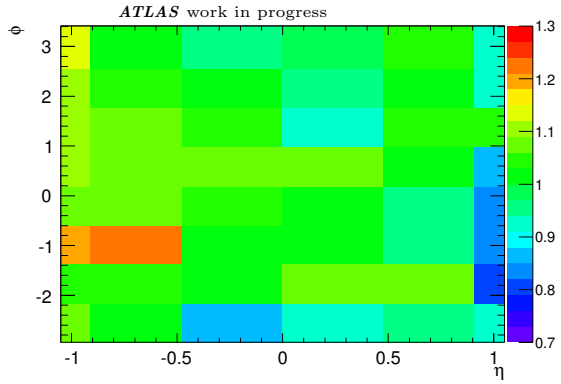

(a) `EF_mu15i` trigger scale factors in the barrel region.

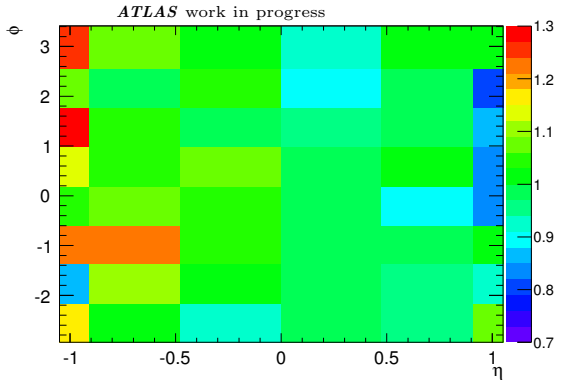

(b) `EF_mu15i_medium` trigger scale factors in the barrel region.

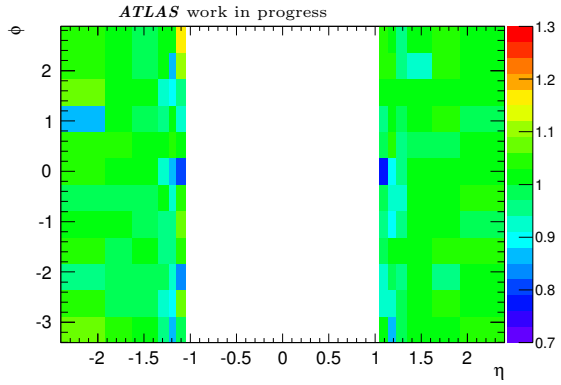

(c) `EF_mu15i` trigger scale factors in the endcap region.

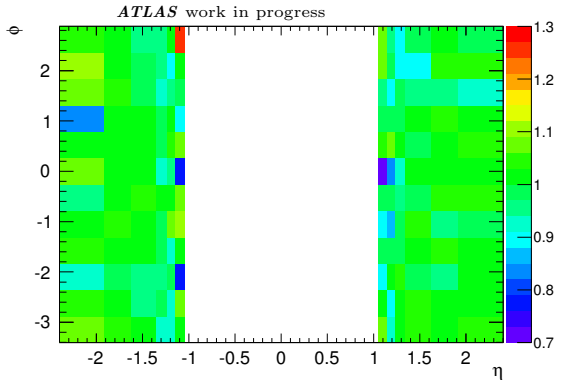

(d) `EF_mu15i_medium` trigger scale factors in the endcap region.

Figure 6.13: Measured trigger efficiency scale factors between data and Monte Carlo simulation as a function of η-ϕ.

6.5 Systematic uncertainties of the tag-and-probe method

There are systematic uncertainties associated with the scale factors. Two sources of systematic errors are considered due to the

- residual background composition in the probe muon sample which is not properly modeled by the simulation. The variation of the background composition in simulation is applied to evaluate differences in the scale factors results.
- $Z \rightarrow \mu\mu$ tag-and-probe association requirements which are varied in both data and simulation to evaluate the sensitivity of the scale factors results to them.

Systematic uncertainties of the muon reconstruction efficiency scale factor The difference between the efficiency measured with respect to calorimeter muon probes and the one measured with respect to ID probes is used as an estimate of the systematic uncertainty associated with the background contribution.

Calorimeter muons are inner detector tracks with a deposit in the calorimeter compatible with the one of a minimum ionizing particle. The measurement of the muon reconstruction efficiency with respect to calorimeter muons further reduces the background contribution. The background is reduced from 0.41% to 0.07% when using calorimeter muons.

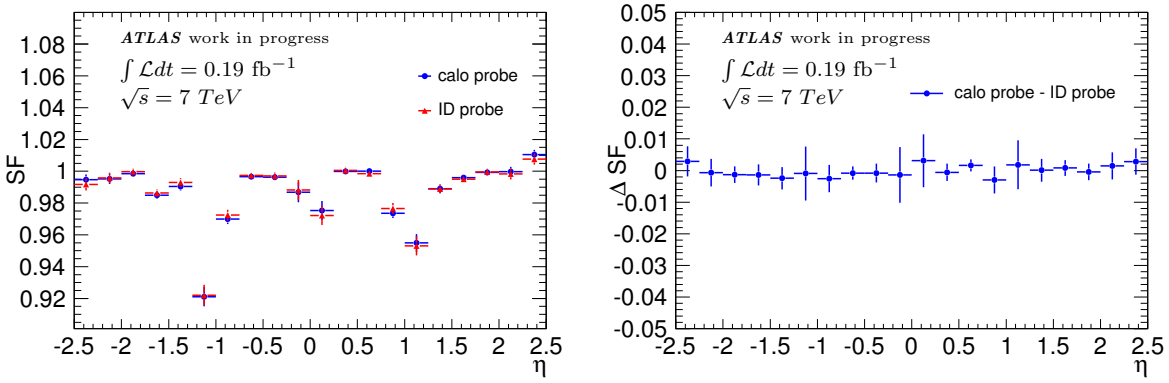

(a) Scale factors to the combined muon reconstruction efficiency for calorimeter muon probes (blue) and ID muon probes (red).

(b) Difference between the efficiency scale factors using calorimeter probes and ID probes.

Figure 6.14: Comparison between the scale factors determined with respect to ID and to calorimeter muon probes as a function of η.

The second source of systematic uncertainties is due to the tag-and-probe definition. The uncertainty due to the finite resolution of the detector is estimated by varying the muon selection cuts. The cuts on the mass window around the Z mass and the cut on the transverse momentum of the tag are varied within their resolution. Other cuts are varied by ± 10%. The resulting change in the scale factors is quoted as systematic uncertainty. The systematic uncertainties on the efficiency scale factor for combined muon reconstruction are summarized in Table 6.7. The

Table 6.7: Contributions to the systematic uncertainty on the measurement of the muon reconstruction efficiency scale factors.

Source	Variation range	ΔSF
Probe isolation	0.20 → 0.22	0.0001
Probe isolation	0.20 → 0.18	-0.0001
Mass window (tag-probe)	10 GeV → 12 GeV	0.
Mass window (tag-probe)	10 GeV → 8 GeV	0.0003
$\Delta\phi$ (tag-probe)	2.0 → 2.2	-0.0003
$\Delta\phi$ (tag-probe)	2.0 → 1.8	-0.0001
Tag p_T	20 GeV → 22 GeV	-0.0003
Tag p_T	20 GeV → 18 GeV	-0.0001
Background	ID probe → Calo probe	0.0001
Total		0.0005

individual systematic uncertainties are assumed to be uncorrelated and are added in quadrature to obtain the total systematic uncertainty. For different up and downward variations the larger value is used. The largest uncertainty arises from the variation of mass window cut followed by the variation of the background contamination and the variation of the probe isolation.

Systematic uncertainties of the muon isolation efficiency scale factor Table 6.8 shows the different contributions to the systematic uncertainty in the isolation efficiency scale factors. The background is low due to the requirement of two reconstructed muons for the isolation measurement. The main contribution to the systematic uncertainty is due to the isolation requirement on the probe muon which affects the background contribution.

Table 6.8: Contributions to the systematic uncertainty on the measurement of the muon isolation efficiency scale factors.

Source	Variation range	ΔSF
Probe isolation	no iso → 0.2	0.0013
Mass window (tag-probe)	10 GeV → 12 GeV	-0.0002
Mass window (tag-probe)	10 GeV → 8 GeV	0.0002
$\Delta\phi$ (tag-probe)	2.0 → 2.2	0.0001
$\Delta\phi$ (tag-probe)	2.0 → 1.8	-0.0001
Tag p_T	20 GeV → 22 GeV	-0.0001
Tag p_T	20 GeV → 18 GeV	0.0001
Total		0.0013

Systematic uncertainties of the muon trigger efficiency scale factors Table 6.9 shows the different contributions to the systematic uncertainty of the trigger efficiency scale factors. As in the previous case, the systematic variations are small due to the low background.

Source	Variation range	ΔSF (EF_mu15i)	ΔSF (EF_mu15i_medium)
Probe isolation	0.20 → 0.22	0	0.0001
Probe isolation	0.20 → 0.18	0	0.0001
Mass window (tag-probe)	10 GeV → 12 GeV	0.0002	0.0003
Mass window (tag-probe)	10 GeV → 8 GeV	0.0001	0.001
$\Delta\phi$ (tag-probe)	2.0 → 2.2	0	0
$\Delta\phi$ (tag-probe)	2.0 → 1.8	0.0002	0.0002
Tag p_T	20 GeV → 22 GeV	-0.0001	0.0003
Tag p_T	20 GeV → 18 GeV	0	0
Total		0.0003	0.0005

Table 6.9: Contributions to the systematic uncertainty on the measurement of the muon trigger efficiency scale factors.

6.6 Muon momentum resolution

The ATLAS detector is designed to provide a measurement of the muon momentum with a resolution of better than 3% for $p_T < 200$ GeV and 10% for $p_T \sim 1$ TeV. The muon momentum resolution is measured in both data and Monte Carlo simulation. Correction factors are applied to simulated events to match the resolution measured in data.

In Fig. 4.2, the contributions to the muon momentum resolution of the muon spectrometer are shown. The relative momentum resolution $\sigma(p)/p$ depends on the amount of material along the muon path, the spatial resolution of the track measurements and the alignment of the muon detector [47].

For a given range of η values, the relative resolution can be parametrized as a function of p_T as:

$$\frac{\sigma(p)}{p} = \frac{p_0^{MS}}{p_T} \oplus p_1^{MS} \oplus p_2^{MS} p_T$$

where p_0^{MS}, p_1^{MS} and p_2^{MS} are the contributions due to the energy loss in the calorimeter, the multiple scattering and the intrinsic detector resolution and alignment, respectively, added in quadrature.

The measurement of the curvature of the ID tracks depends on the length of the muon track in the active material which is reduced at the borders of the TRT fiducial volume and leads to degradation of the resolution for η values beyond this region:

$$\frac{\sigma(p)}{p} = p_1^{ID} \oplus p_2^{ID} p_T \qquad |\eta| < 1.9,$$

$$\frac{\sigma(p)}{p} = p_1^{ID} \oplus p_2^{ID} p_T \frac{1}{\tan^2(\theta)} \qquad |\eta| > 1.9.$$

The resolution strongly depends on the pseudorapidity. For this reason, it is calculated separately

in different η regions, namely in

- the barrel region, $0 < |\eta| < 1.05$,
- the transition region, $1.05 < |\eta| < 1.7$,
- the endcaps, $1.7 < |\eta| < 2.0$,
- and the CSC region (without TRT hits), $2.0 < |\eta| < 2.5$.

Since the tracking performance in the barrel region has been extensively studied by means of cosmic rays, the resolution is supposed to be best understood in that region.

The width of the Z$\rightarrow \mu\mu$ invariant mass distribution provides information both on the momentum resolution and the momentum scale. The same is true for the difference between the muon momentum measured in the ID and the MS in W$\rightarrow \mu\nu$ events. Correction factors are applied to the Monte Carlo resolution to match the data. The combined ID and MS track fit provides the different contributions to the muon momentum resolution separately for ID and MS tracks. Alignment constraints are needed in order to determine the intrinsic resolution term (p_2). In Figure 6.15, the muon momentum resolution is shown as a function of the muon transverse momentum for ID and MS tracks in the barrel region.

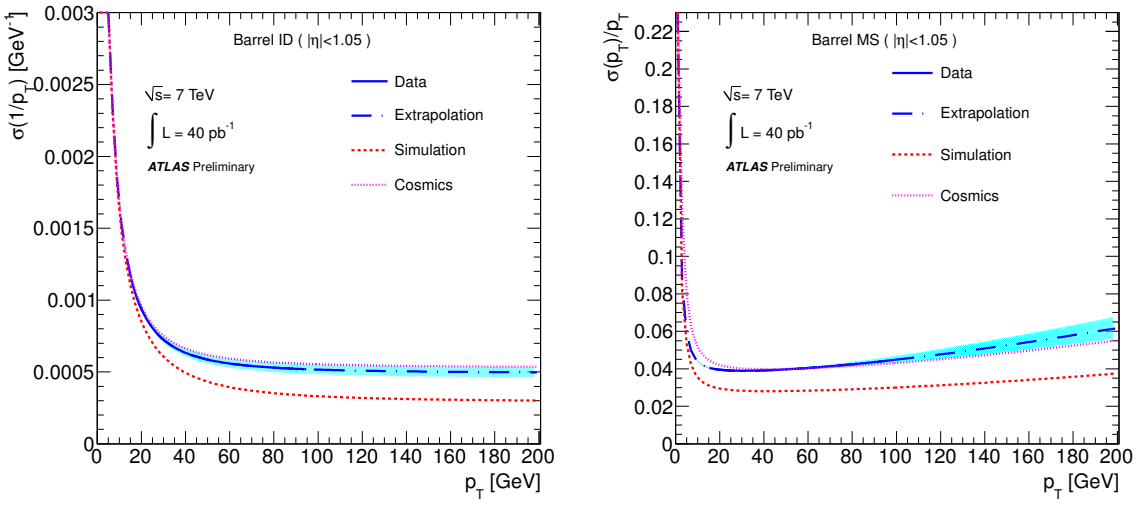

Figure 6.15: Muon momentum resolution in the barrel region for ID (left) and MS (right) tracks as a function of the transverse momentum [47].

Chapter 7

Measurement of the $Z \to \tau\tau$ production cross section

The measurement of the $Z \to \tau\tau$ production cross section is important for several reasons. First, the measurement of the Z production cross section in the $\tau\tau$ final state can confirm the measurements in the final states with electron and muon pairs. In addition, $Z \to \tau\tau$ decays are an irreducible background for the search for new heavy particles involving taus in the final states. The search for such new particles decaying into τ pairs requires an accurate measurement of the $Z \to \tau\tau$ background. $Z \to \tau\tau$ decays are also important for performance studies. The τ identification efficiency can be measured using the tag-and-probe technique.

Measurements of the $Z \to \tau\tau$ production cross section have been made previously by both ATLAS [48] and CMS [49] using collision data collected in 2010. In this thesis, an updated measurement of the cross section for $Z \to \tau\tau$ production is presented using data collected by the ATLAS experiment in 2011. The cross section is measured in the invariant mass range $66 < m_{\tau\tau} < 116$ GeV at a centre-of-mass energy of 7 TeV. The final state depends on the decay mode of the τ leptons. In particular, semi-leptonic final states are studied where one τ decays hadronically and the other one into an electron or muon with the accompanying neutrinos. The electron and muon channels are studied separately. The selection of signal events can be divided into three steps:

- Selection of collision events: good detector operating conditions, primary vertex and trigger requirements.
- Selection of physics objects for the analysis (mainly electrons, muons and hadronic τ decays).
- Selection of $Z \to \tau\tau$ events combining the objects (leptonic and hadronic τ decays).

Finally, the cross section is calculated with systematic uncertainties.

7.1 Introduction

τ leptons have a lifetime of $2.9{\cdot}10^{-13}$ seconds, corresponding to a mean free path of $c\tau \sim 100$ μm. This means that τ leptons decay before leaving the beam pipe. This makes it impossible to distinguish between electrons (muons) from the τ lepton decays and electrons (muons) emerging from the primary vertex.

The τ decay branching ratios are listed in Table 7.1.

Table 7.1: τ decay branching ratios [14].

Leptonic Modes	($\approx$ 35%)
$e\nu_e\nu_\tau$	18%
$\mu\nu_\mu\nu_\tau$	17%
Hadronic Modes: 1 Prong	($\approx$ 47%)
$\pi^-\nu_\tau$	11%
$\pi^-\pi^0\nu_\tau$	25%
$\pi^-\pi^0\pi^0\nu_\tau$	9%
$\pi^-\pi^0\pi^0\pi^0\nu_\tau$	1%
$K^- + Neutrals$	1.5%
Hadronic Modes: 3 Prong	($\approx$ 15%)
$\pi^-\pi^+\pi^-\nu_\tau$	9%
$\pi^-\pi^+\pi^-\pi^0\nu_\tau$	4.5%
$K^-\pi^+\pi^-\nu_\tau$	0.4%
Other Modes	($\approx$ 3%)

$Z \rightarrow \tau\tau$ decays can be studied in different final states depending on the τ decay modes:

- Fully leptonic final states ($\tau_e\tau_\mu$, $\tau_\mu\tau_\mu$, $\tau_e\tau_e$): While the $\tau_e\tau_e$ final state is difficult to study due to the overwhelming $Z \rightarrow ee$ background, the results for the $\tau_\mu\tau_e$ and $\tau_\mu\tau_\mu$ channels are reported in [48].

- Fully hadronic final states ($\tau_h\tau_h$): Although this final state has the highest branching ratio, the selection of signal events is difficult in proton proton collisions due to the high multi-jet background.

- Semileptonic final states ($\tau_e\tau_h$, $\tau_\mu\tau_h$): In both channels a clean samples of hadronic τ decays can be selected for performance studies. The selection of this final state is described in detail in this chapter.

In the weak decay of τ leptons, neutrinos are produced and contribute to the missing transverse energy of the event. The visible mass of the electron (muon) and the hadronic τ decay is defined as the invariant mass of the visible particles in the final state. This variable depends on the τ energy scale only and does not depend on the missing transverse energy which is used only in the event selection. The visible mass is not affected by uncertainties in the missing transverse energy measurement which is difficult in events with more than one neutrino.

7.2 Data samples

7.2.1 Collision data

Collision data were collected during 2011 at a centre-of-mass energy of 7 TeV. The data are divided to periods with different data taking conditions. In particular there were different pile-up conditions since the luminosity increased over the whole data taking period. Table 7.2 shows the integrated luminosity of each period used for the analysis. The total luminosities used for the $\tau_e\tau_{\mathrm{h}}$ and $\tau_\mu\tau_{\mathrm{h}}$ channel, respectively, are 1.34 fb^{-1} and 1.55 fb^{-1}. The difference between the total luminosities in the two channels is due to different triggers applied (see section 7.3.2).

Table 7.2: Integrated luminosities for the different data taking periods used for the analysis.

run period	run number	$\int \mathcal{L}dt$ (pb^{-1}), $\tau_e\tau_{\mathrm{h}}$	$\int \mathcal{L}dt$ (pb^{-1}), $\tau_\mu\tau_{\mathrm{h}}$
period B	178044 - 178109	-	11
period D	179725 - 180481	-	150
period E	180614 - 180776	-	42
period F	182013 - 182519	123	123
period G	182726 - 183462	464	464
period H	183544 - 184169	240	240
period I	185353 - 186493	305	305
period J	186516 - 186755	212	212
total		1344	1547

7.2.2 Monte Carlo data

Signal and background processes relevant for the $Z \to \tau\tau$ analysis are simulated with the full detector simulation. Pile-up conditions are simulated taking into account multiple interactions per bunch crossing (in-time pile-up) and particles produced in preceding bunches (out-of-time pile-up). Event weights are applied to tune the Monte Carlo samples to the pile-up conditions observed in the collision data.

The different Monte Carlo simulated processes taken into account for the analysis are listed in Table 7.3:

- $\gamma^*/Z \to \tau\tau$ + jets: This is the signal process. The unfiltered sample contains all the possible τ decay modes.
- $\gamma^*/Z \to \ell\ell$ + jets: This background contributes to the $\tau_\ell\tau_{\mathrm{h}}$ final state. A lepton or a jet from Z + jet events can be misidentified as a hadronic τ decay.
- $W \to \ell\nu$ + jets: This background contributes to the $\tau_\ell\tau_{\mathrm{h}}$ final state when a jet is misidentified as hadronic τ decay. Specific cuts are applied in order to suppress this background (see section 7.5.2).

- $W \rightarrow \tau\nu$ + jets: This background contributes to the $\tau_e\tau_{\mathrm{h}}$ and $\tau_\mu\tau_{\mathrm{h}}$ channel depending on the τ decay mode. It contributes most when the τ decays into electron or muon and a jet fakes a hadronic τ decay. This background is negligible for the measurement of the $Z \rightarrow \tau\tau$ cross section because of the small τ branching ratio into leptons and due to the W suppression cuts (see section 7.5.2).

- $t\bar{t}$ background: It contributes to both the $\tau_e\tau_{\mathrm{h}}$ and the $\tau_\mu\tau_{\mathrm{h}}$ channel depending on the leptonic decays of the W bosons produced in the weak top decays. The hadronic τ is simulated by τ misidentified jet. The contribution of this background to the selected event sample is small due to the low cross section.

- Multi-jet background: It contributes to both the $\tau_e\tau_{\mathrm{h}}$ and the $\tau_\mu\tau_{\mathrm{h}}$ channel due to semileptonic quark decays and the misidentification of a jet as a hadronic τ candidate. The multi-jet cross section is high in p-p collisions and Monte Carlo events cannot be simulated with sufficient statistics. In addition, the production cross section and the properties of jets are not correctly described by the simulation. For these reasons, the multi-jet background is estimated directly from collision data collected.

Table 7.3 shows the main Monte Carlo processes used for the analysis. The W and γ^*/Z samples are generated with ALPGEN [35] using the CTEQ6L1 [50] parton distribution functions. The corresponding LO cross sections used by the generator are rescaled to the NNLO calculations. The τ decays are modeled with the TAUOLA package [51] where the effect of QED final state radiation is described by PHOTOS [52]. The Monte Carlo samples generated with ALPGEN with different numbers of additional partons in the final state are combined by weighting them with their cross sections.

The $t\bar{t}$ background is generated with the MC@NLO program [33] where the parton shower and hadronization are simulated with HERWIG [34] and the underlying event with Jimmy [53]. The diboson samples are generated with HERWIG.

Table 7.3: List of the Monte Carlo data.

Generator	Dataset	cross section (pb)
ALPGEN	$\gamma^*/Z \rightarrow \tau\tau$ ($m_{\tau\tau} > 10\ GeV$, 0p-5p)	5063
	$\gamma^*/Z \rightarrow ee$ ($m_{ee} > 10\ GeV$, 0p-5p)	5062
	$\gamma^*/Z \rightarrow \mu\mu$ ($m_{\mu\mu} > 10\ GeV$, 0p-5p)	5063
	$W \rightarrow e\nu$ (0p-5p)	10486
	$W \rightarrow \mu\nu$ (0p-5p)	10483
	$W \rightarrow \tau\nu$ (0p-5p)	10481
MC@NLO	$t\bar{t}$ (no fully hadronic decays)	90
HERWIG	WW	11
	ZZ	1.0
	WZ	3.4

7.3 Event selection

The following requirements are applied in order to select events from proton proton collisions.

7.3.1 Good detector operating conditions

A good run list (GRL) is a list of collision data taking runs with good detector operating conditions for physics analyses. Data Quality (DQ) information allows for the selection of good luminosity blocks in each run. DQ flags indicate correct performance of the sub-detectors.

Several good run lists are produced depending on the final state to be analyzed. For the study of the semi-leptonic $Z \to \tau\tau$ final states, a combined good run list is used. The flags used for the list include global ATLAS stability flags including the correct operation of the solenoid and toroid magnets. The reliability of electron, muon and hadronic τ triggers is ensured by the trigger flags. The quality of data from detector components involved in the measurement of muons, electrons, τ candidates and of E_T^{miss} is verified with specific quality flags both for the barrel and the endcap regions.

The total luminosity is calculated with a web-based tool [54] from the luminosities of each run present in the GRL.

7.3.2 Trigger requirements

Different triggers are used for the $Z \to \tau\tau$ analysis depending on the final state.

Events are required to pass a single muon trigger for the $\tau_\mu\tau_{\text{h}}$ channel which selects events at Event Filter level with an isolated muon with $p_T > 15$ GeV (`EF_mu15i` or `EF_mu15i_medium`). The `EF_mu15i` trigger was used for periods B-I while the `EF_mu15i_medium` trigger was used in period J to cope with the higher event rate at Level 1 due to the increase of the luminosity.

Events are required to pass a combined trigger for the $\tau_e\tau_{\text{h}}$ channel at Event Filter level which selects event with a hadronic τ-jet with $p_T > 16$ GeV in combination with an electron with $p_T > 15$ GeV fulfilling quality requirements (`EF_tau16_loose_e15_medium`). The loose trigger selection for the hadronic τ decay is due to soft cuts in the calorimetric shower shape variables while the medium requirements for the electron trigger are similar to the medium offline reconstruction criteria (see section 5.3.1). A combined trigger is used to increase the signal efficiency since single-electron triggers are possible only with higher electron transverse momentum threshold.

The hadronic τ trigger is not taken into account in the Monte Carlo simulation. The τ trigger efficiency is rather measured in data with the $Z \to \tau\tau$ tag-and-probe method and applied to selected hadronic τ candidates in the simulation as a function of the τ transverse momentum. The method used for the measurement of the τ trigger efficiency is described in detail in [1].

The muon and electron trigger requirements are included in the simulation and scale factors are applied to take into account differences between the trigger efficiency measured in the simulation and the one measured in collision data.

7.3.3 Primary vertex requirement

Proton-proton collision events are required to contain at least one primary vertex with at least four associated tracks in order to reject pile-up events which do not belong to the collisions.

7.3.4 Event cleaning

An additional selection is applied to reduce high-energy deposits in the calorimeter not associated to proton proton collisions (so-called "jet cleaning") and objects that lie in problematic detector regions (so-called "LAr cleaning").

Jet cleaning High-energetic deposits in the calorimeters may be not associated to proton-proton collisions. They can also be due to discharges in the hadronic end-cap calorimeter, to coherent noise in the electromagnetic calorimeter or to cosmic-ray showers resulting in the reconstruction of fake QCD and τ jets and to wrong E_T^{miss} measurement. The impact of such rare events is non-negligible for the E_T^{miss} measurement leading to high E_T^{miss} tails.

Events with fake jets entering in the E_T^{miss} measurement are removed by the jet-cleaning procedure [55] requiring reconstructed jets and τ candidates not to overlap with reconstructed electrons or muons. The cleaning procedure is applied only to data events since many of the variables involved in the cleaning are not well modeled by the Monte Carlo simulation.

LAr cleaning This procedure is applied to specific events with noise bursts and data integrity errors in the LAr calorimeter. The quality of the calorimeter clusters is assured with the help of the Object Quality map.

In addition, reduced reconstruction efficiency in the LAr calorimeter was observed from run 180614 to 185353. Events from that period within the affected LAr calorimeter acceptance region[1] are not used for the analysis. The fraction of events removed from data is taken into account in the simulation by re-weighting the Monte Carlo events.

7.4 Selection of physics objects

The $Z \rightarrow \tau_\ell \tau_{\text{h}}$ analysis depends on several reconstructed objects, electrons, muons, hadronic τ decays and E_T^{miss}. Jets are reconstructed with the anti-k_{T} algorithm [40] and are used only to veto events in the jet cleaning.

Electron, muon and hadronic τ candidates are selected in two steps: preselection and main selection. An overlap removal procedure is applied (for τ leptons) to remove candidates also identified as electrons or muons. In the preselection step, loose criteria are applied. Preselected objects are used for the dilepton veto (see section 7.5.1) and the τ candidate overlap removal. For

[1] for electrons: -0.1< η <1.44 and -0.888< ϕ <-0.492
for jets (with $p_{\text{T}} > 20$ GeV): -0.2< η <1.6 and -0.988< ϕ <-0.392
for taus: -0.1< η <1.55 and -0.9< ϕ <-0.5, using the coordinate of the leading track.

electrons and muons, isolation cuts are applied in order to reduce the contribution of electrons and muons coming from jets.

7.4.1 Muon selection

Preselection Muons are reconstructed with the STACO algorithm with *loose* identification requirements which includes combined and segment-tagged muon candidates. Muons have to fulfill the requirements $p_T > 6$ GeV and $|\eta| < 2.7$. The contribution of fake hadronic τ decays is reduced by the overlap removal which requires the hadronic τ candidates to have a distance from the muon candidate of $\Delta R > 0.4$.

Final selection Further cuts are applied to reduce the contribution of fake muons, mainly from pion decays. The final muon selection requires $p_T > 17$ GeV within $|\eta| < 2.4$ refining the trigger p_T-threshold and acceptance. As discussed in section 6.4, the muon trigger efficiency reaches the plateau at ~ 17 GeV. The longitudinal distance of the muon track from the primary vertex is required to be less than 10 mm. Inner detector track quality criteria (see Table 6.2) are applied.

The preselection and final selection cuts are summarized in Table 7.4.

7.4.2 Electron selection

Preselection Medium identification criteria based on cuts on both calorimeter and inner detector variables are applied to reconstructed electron candidates to reduce the background due to photon and jet misidentification: $E_T > 15$ GeV and $|\eta| < 2.47$, excluding the region between the end-cap and barrel LAr calorimeter ($|\eta| = 1.37$-1.52). In addition, electrons are rejected if their calorimeter clusters are affected by detector problems according to the Object Quality map.

Final selection Electron candidates with $E_T > 17$ GeV are identified with the tight requirements. The increase in the electron transverse energy cut value is due to the electron trigger threshold.

The preselection and final selection cuts are summarized in Table 7.4.

7.4.3 Hadronic τ decay selection

Preselection Hadronic τ decay candidates are required to have $p_T > 20$ GeV and $|\eta| < 2.47$, excluding the region $|\eta| = 1.37$-1.52. The transverse momentum is raised to 25 GeV in the $\tau_e\tau_h$ channel where the τ trigger efficiency turn-on curve is not well modeled by the simulation close to the p_T threshold. A small fraction of the hadronic τ candidates is removed at $|\eta| < 0.03$ because of the high fake rate from electrons in the small crack region of the TRT.

Final selection Hadronic τ candidates are selected if they fulfill the preselection requirements and do not overlap with preselected electrons and muons. 1-prong and multi-prong τ candidates are identified using the Boosted Decision Tree method. A tight electron veto is applied to reduce the number of electrons misidentified as hadronic τ candidates.

The preselection and final selection cuts are summarized in Table 7.4.

7.4.4 Lepton isolation

Electrons and muons from $Z \rightarrow \tau\tau$ events are isolated, in contrast to leptons arising from jets, especially when they are from b-quark decays. Isolation requirements are applied to further reduce the contribution of the multi-jet background after the lepton selection. The transverse energy (from the calorimeters) and the transverse momentum (from the inner detector) in a cone around the lepton direction divided by the lepton $\mathrm{p_T}$ are used as measures of the lepton isolation.

Different isolation variables with different cone sizes $\Delta R = 0.30$ and 0.40 have been studied. Figure 7.1 shows the fake background efficiency as a function of the signal efficiency, for the $\tau_\mu\tau_\mathrm{h}$ (left) and $\tau_e\tau_\mathrm{h}$ (right) channel. The signal efficiency is defined as the fraction of leptons from $Z \rightarrow \tau\tau$ decays that satisfy a particular isolation cut, while the background efficiency is calculated from multi-jet events, estimated from the same sign control region (which is dominated by jet events) and extrapolated to the opposite sign signal region, that passed the isolation cut.

The combination of the transverse energy and the transverse momentum in a predefined cone gives the best discrimination between signal and background.

In the $\tau_\mu\tau_\mathrm{h}$ channel, an isolation cut is applied by the trigger, increasing the multi-jet background rejection. An additional isolation cut on selected muon is anyway needed to increase the signal purity in collision data. The tight isolation is important for the definition of the control regions used for the multi-jet background estimation from data (see section 7.6.3). Indeed, the control regions do not contain many multi-jet events after the trigger requirement. A tighter isolation increases the signal purity in the signal region, as well as the number of multi-jet events in the control regions.

Figure 7.2 shows the lepton isolation criteria used for the analysis:

- Muon isolation: $\frac{1}{p_T}\sum_i p_T(\Delta R = 0.4) < 0.03$, $\frac{1}{p_T}\sum_i E_T(\Delta R = 0.3) < 0.04$.
- Electron isolation: $\frac{1}{p_T}\sum_i p_T(\Delta R = 0.4) < 0.06$, $\frac{1}{p_T}\sum_i E_T(\Delta R = 0.4) < 0.10$.

The cuts correspond to a signal efficiency of 0.76(0.82) for the muon (electron) channel. Scale factors for the specific cuts are applied to the leptons that passed the isolation cuts.

7.4.5 Requirement on Missing Transverse Energy

The calculation of E_T^{miss} takes into account three contributions:

$$E_T^{\mathrm{miss}} = E_T(\text{calorimeter clusters}) + E_T(\text{muon tracks}) - E_T(\text{muon calorimeter energy}). \quad (7.1)$$

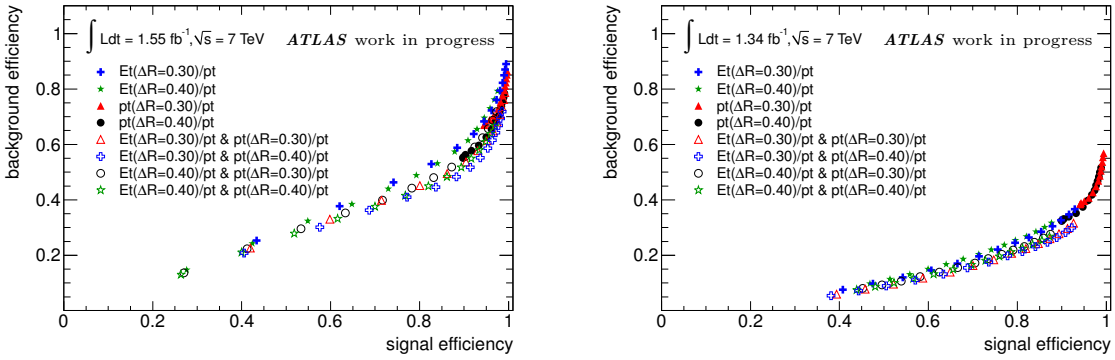

Figure 7.1: Muon (left) and electron (right) signal and background efficiencies for different lepton isolation cone sizes.

The first term is determined from the energy deposits in the calorimeter cells of three-dimensional clusters and with the local hadron calibration [56]. Cluster energies are corrected for losses due to noise suppression thresholds and dead material. The second term is the sum of the transverse energies of all reconstructed and isolated muons. Muons are not taken into account if the distance ΔR to the nearest jet is less than 0.3. The third term corrects for the energy deposit of the isolated muons in the calorimeter avoiding double counting.

Table 7.4 summarizes the particle selection criteria for the $Z \rightarrow \tau\tau$ analysis.

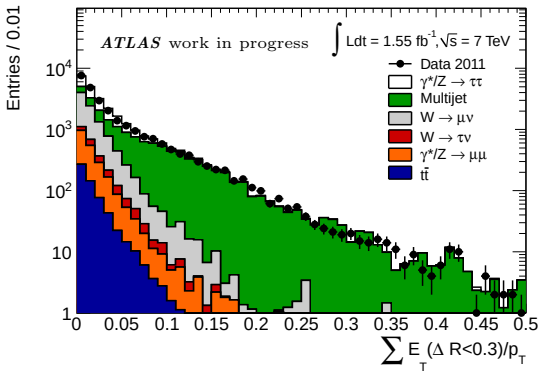

(a) muon isolation, $\frac{1}{p_T}\sum_i E_T(\Delta R = 0.3)$

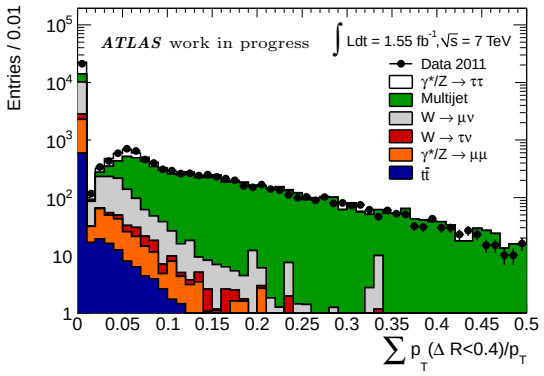

(b) muon isolation, $\frac{1}{p_T}\sum_i p_T(\Delta R = 0.4)$

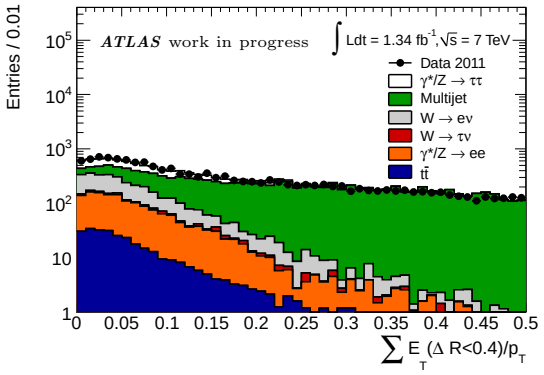

(c) electron isolation, $\frac{1}{p_T}\sum_i E_T(\Delta R = 0.4)$

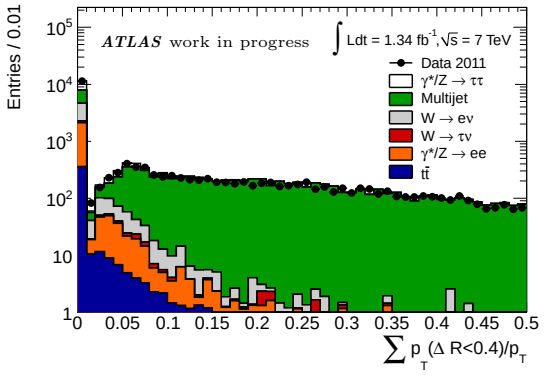

(d) electron isolation, $\frac{1}{p_T}\sum_i p_T(\Delta R = 0.4)$

Figure 7.2: Variables used to estimate the lepton isolation for signal and background processes. Events with one identified lepton and one identified τ candidate are used. The multi-jet background is estimated from same sign lepton-hadronic τ combination.

Table 7.4: Selection criteria for the $Z \to \tau\tau$ production cross section measurement (see text).

Event preselection	
Primary Vertex	$N_{vtx} \geq 1$ with $N_{trk,vtx} \geq 4$
Jet Cleaning	"medium" requirements
Trigger	`EF_tau16_loose_e15_medium` ($\tau_e\tau_{\rm h}$ channel) `EF_mu15i`,`EF_mu15i_medium` ($\tau_\mu\tau_{\rm h}$ channel)
Particle preselection	
Electrons	$p_T > 15$ GeV, $\lvert\eta\rvert < 2.47$, excluding $1.37 < \lvert\eta\rvert < 1.52$, not in bad OQmaps region, medium identification criteria.
Muons	$p_T > 6$ GeV, $\lvert\eta\rvert < 2.7$, loose identification criteria.
Hadronic τ decays	$p_T > 20$ GeV ($\tau_\mu\tau_{\rm h}$ channel), $p_T > 25$ GeV ($\tau_e\tau_{\rm h}$ channel), $\lvert\eta\rvert < 2.47$ excluding $1.37 < \lvert\eta\rvert < 1.52$, veto on leading track in $\lvert\eta\rvert < 0.03$.
Particle selection	
Electrons	$p_T > 17$ GeV, tight identification criteria, isolation requirements: $\sum p_T(\Delta R = 0.40)/p_T < 0.06$; $\sum E_T(\Delta R = 0.40)/p_T < 0.1$.
Muons	$p_T > 17$ GeV, $\lvert z_0\rvert < 10$ mm, inner detector hits, isolation requirements: $\sum p_T(\Delta R = 0.40)/p_T < 0.03$; $\sum E_T(\Delta R = 0.30)/p_T < 0.04$.
Hadronic τ decays	tight electron veto, medium BDT identification criteria, overlap removal with preselected electrons, muons and τ leptons.
Event selection	
Opposite charge τ-lepton	$\text{charge}(\tau_{\rm h}) \times \text{charge}(\ell) < 0$.
Dilepton veto	N(preselected leptons)= 1.
W+jets background suppression	$\sum \cos\Delta\phi > -0.15$, $m_T < 50$ GeV.
Hadronic τ decay requirements	$N_{\rm tracks}(\tau_{\rm h}) = 1$ or 3, $\lvert\text{charge}(\tau_{\rm h})\rvert = 1$, EM calorimeter energy fraction > 0.10 ($\tau_\mu\tau_{\rm h}$ channel).
Visible mass of $\tau_\ell\tau_h$	35 GeV $< m_{\rm vis} <$ 75 GeV.

7.5 $Z \to \tau\tau$ event selection

In this section, the selection criteria for $Z \to \tau\tau$ events in addition to the particle selection are described. At least one hadronic τ decay candidate and one isolated lepton with opposite electric charge is requested.

The discriminating variables in data and Monte Carlo simulation with signal and background contributions are compared after each step in the cut flow in the order shown in Table 7.4. The expected numbers of W and Z background events from Monte Carlo simulation are normalized to data (see sections 7.6.1 and 7.6.2). The multi-jet background is estimated from data using a control region defined by inversion of the charge product requirement (same-sign of the lepton and the hadronic τ decay electric charge) and extrapolating to the signal region (see section 7.6.3).

7.5.1 Di-lepton veto

Events from the $Z \to \tau\tau$ semileptonic final state have one electron or muon. The dilepton veto removes events with more than one preselected lepton. This cut strongly reduces $(Z \to \ell\ell)$+jets events where the hadronic τ is a misidentified jet. In addition, fully leptonic $Z \to \tau\tau$ final states are vetoed.

Figure 7.3 shows the distribution of the numbers of preselected muons (left) and electrons (right). Good agreement is found between data and Monte Carlo simulation.

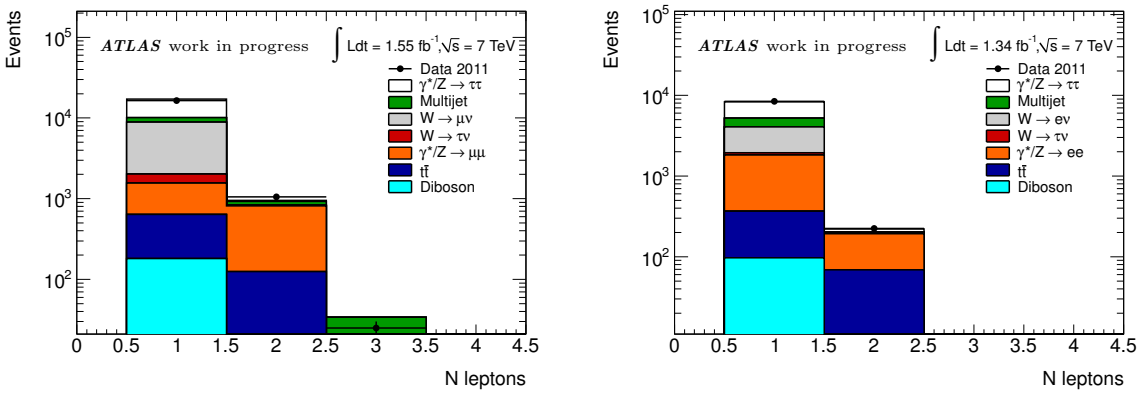

(a) Muons (b) Electrons

Figure 7.3: The numbers of preselected leptons after the opposite sign charge requirement (see Table 7.4). Data and Monte Carlo simulation are compared.

7.5.2 W background suppression cuts

After the dilepton veto, the main background contribution are W decays, mainly $W \to \ell\nu$.

The Z boson mass is much higher than the τ lepton mass. This implies that the τ leptons from Z decays are boosted and their decay products are collimated along the τ direction. The

τ leptons from Z boson decays are mainly produced back-to-back in the transverse plane since the Z bosons are produced with low p_T. In case the Z bosons are produced with a boost in the transverse plane, the E_T^{miss} vector points between the Z decay products as illustrated in Figure 7.4(a).

In $(W \to \ell\nu)$ + jets events, the neutrino, the muon and the jets (misidentified as hadronic τ decays) point in different directions balancing the p_T of the W (Fig. 7.4(b)) in case the jets do not belong to underlying events. The E_T^{miss} due to the missing neutrino energy does not point between the lepton and the fake hadronic τ. The kinematics is similar for $(W \to \tau\nu)$ + jets events where an additional contribution to E_T^{miss} comes from the neutrinos from the τ decay (Fig. 7.4(c)).

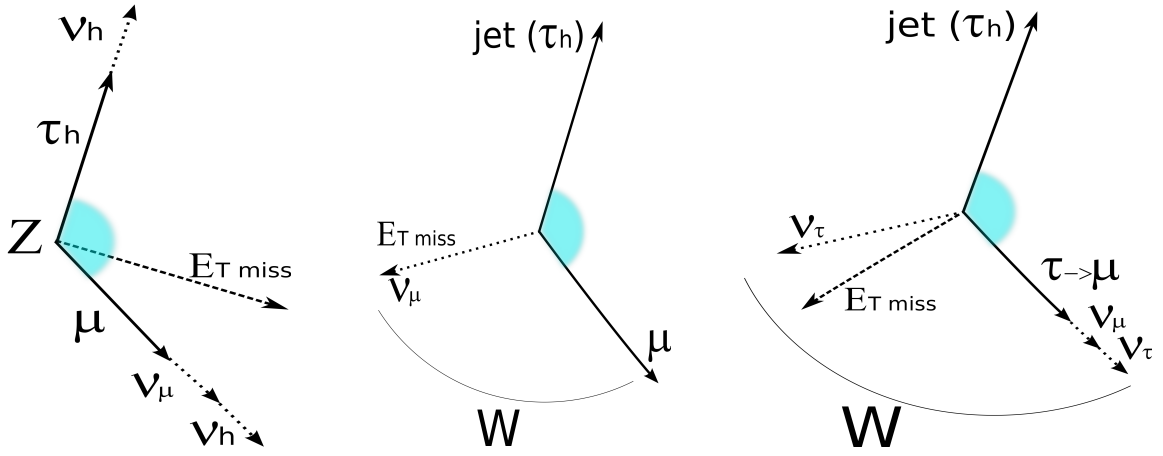

(a) $Z \to \tau\tau \to (\mu\nu_\mu\nu_\tau)(\tau_h\nu_\tau)$. (b) $(W \to \mu\nu_\mu)$ + jet. (c) $(W \to \tau\nu_\tau)$ + jet $\to (\mu\nu_\mu\nu_\tau)\nu_\tau$ + jet.

Figure 7.4: Kinematics of W + jets and $Z \to \tau\tau$ decays in the transverse plane. τ_h is a hadronic τ jet and (τ_h) a fake hadronic τ jet.

Two variables exploiting the kinematical correlation between the lepton and the missing transverse energy are defined in order to suppress the W + jet background. The first variable is

$$\sum \cos\Delta\phi = \cos\left(\phi(\ell) - \phi(E_T^{\text{miss}})\right) + \cos\left(\phi(\tau_h) - \phi(E_T^{\text{miss}})\right) \tag{7.2}$$

(see Figures 7.5(a) and (c)). Signal events are concentrated at $\sum \cos\Delta\phi \approx 0$ corresponding to back-to-back τ decays in the transverse plane. Positive values correspond to E_T^{miss} vectors pointing towards the direction between the decay products while negative values correspond to E_T^{miss} pointing away. Events with $\sum \cos\Delta\phi <$ -0.15 are rejected.

The $\sum \cos\Delta\phi$ variable is robust against mis-measurement of the magnitude of E_T^{miss} and allows for good rejection of W + jets events. It is sensitive only to the direction of E_T^{miss} which is measured with higher accuracy than its magnitude.

The second variable used for W + jets event rejection is the transverse invariant mass of the lepton-E_T^{miss} system:

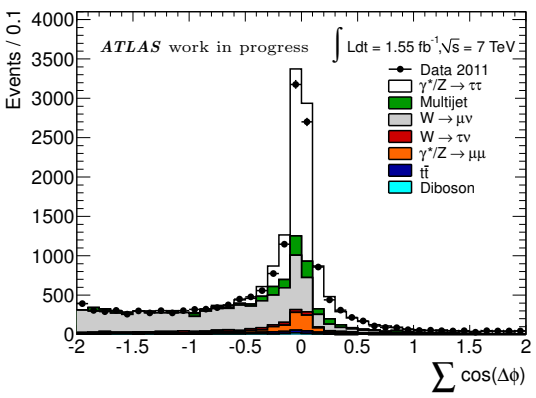

(a) $\tau_\mu\tau_\mathrm{h}$ channel.

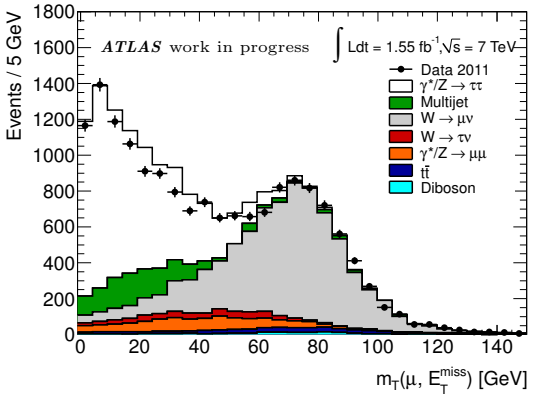

(b) $\tau_\mu\tau_\mathrm{h}$ channel.

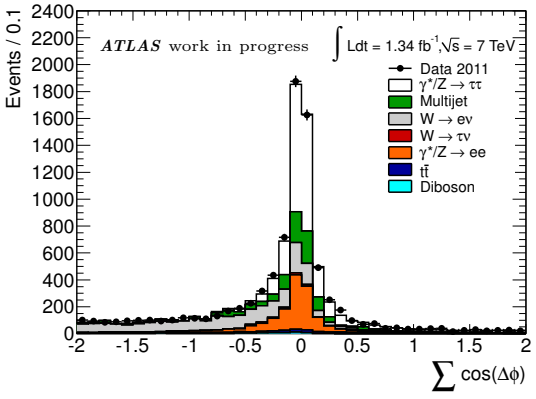

(c) $\tau_e\tau_\mathrm{h}$ channel.

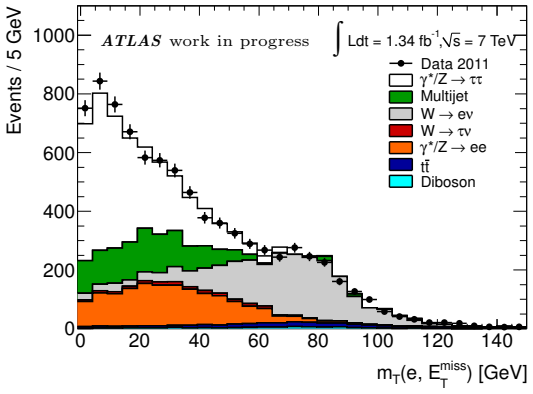

(d) $\tau_e\tau_\mathrm{h}$ channel.

Figure 7.5: The angular correlation (Eq. 7.2) and the transverse invariant mass (Eq. 7.3) after the dilepton veto and the opposite charge sign requirements. The shape of the multi-jet background is taken from the control region obtained by inversion of the charge product sign requirement. It is normalized to the signal region expectation (see section 7.6.3).

$$m_\mathrm{T}(\ell, E_T^\mathrm{miss}) = \sqrt{2\, p_\mathrm{T}(\ell) \cdot E_T^\mathrm{miss} \cdot (1 - \cos\Delta\phi(\ell, E_T^\mathrm{miss}))} \tag{7.3}$$

(see Figures 7.5(b) and (d)). Signal events are concentrated at low values. In particular when the lepton and the hadronic τ jet are back-to-back in the transverse plane, E_T^miss tends towards zero and the $\cos\Delta\phi(\ell, E_T^\mathrm{miss})$ to one leading to $m_\mathrm{T}(\ell, E_T^\mathrm{miss})$ values close to zero. For the $Z \to \tau\tau \to (\ell\nu\nu)(\tau_\mathrm{h}\nu)$ events, E_T^miss points close to the lepton direction because of the two neutrinos produced in that direction. For $W \to \ell\nu$ events, $m_\mathrm{T}(\ell, E_T^\mathrm{miss})$ coincides with the W mass when the neutrino and the lepton have no z-components in the W rest frame. Events are rejected if $m_\mathrm{T}(\ell, E_T^\mathrm{miss}) > 50$ GeV.

7.5.3 Hadronic τ jet cleaning

Hadronic τ decays can be distinguished from QCD jets by selecting candidates with low track multiplicity. Hadronic τ decays have mainly 1 or 3 charge particles (pions or kaons) in the final state. Figure 7.6 shows the number of charged particles and Figure 7.7 the electromagnetic energy fraction (Eq. 5.5) of the τ candidates. The electromagnetic fraction is defined as the ratio between the energy deposit in the EM calorimeter divided by the total calorimeter energy.

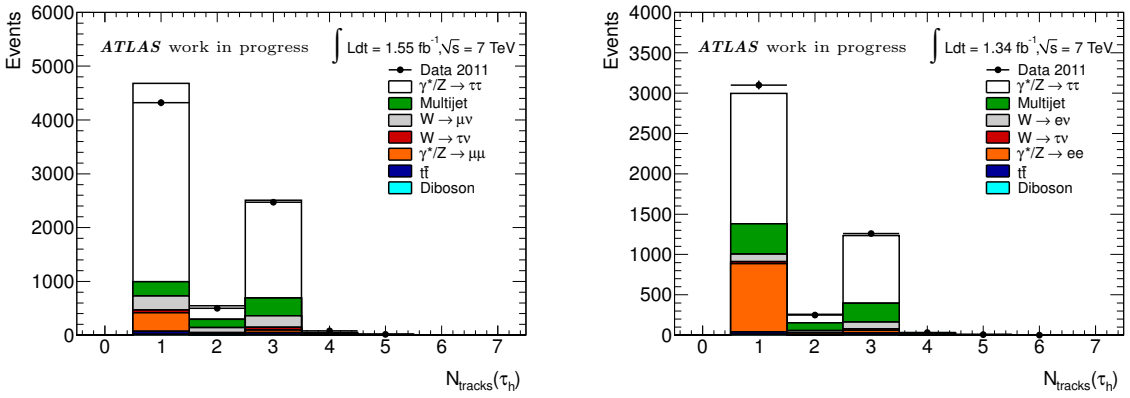

(a) (b)

Figure 7.6: Number of tracks of the hadronic τ decay candidates (a) in the $\tau_\mu\tau_{\mathrm{h}}$ channel and (b) in the $\tau_e\tau_{\mathrm{h}}$ channel.

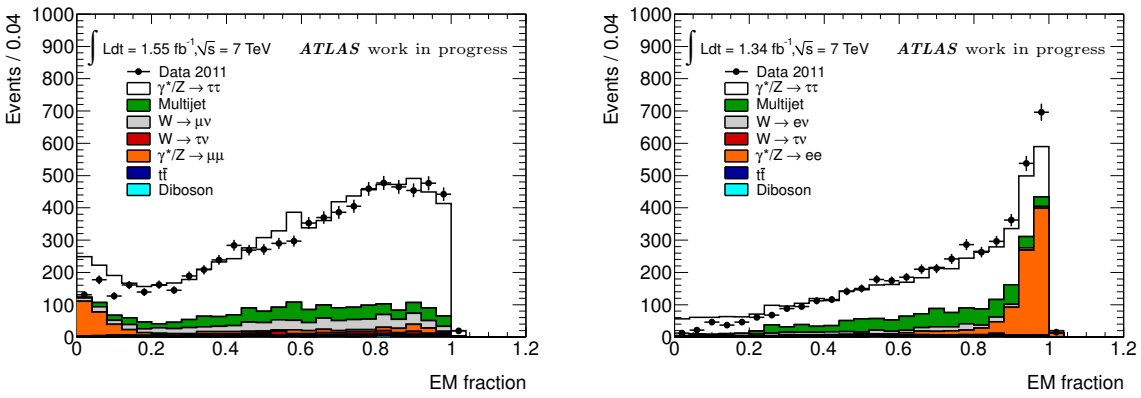

(a) (b)

Figure 7.7: The electromagnetic energy fraction for hadronic τ candidates (a) in the $\tau_\mu\tau_{\mathrm{h}}$ channel and (b) in the $\tau_e\tau_{\mathrm{h}}$ channel.

An excess of events is found at low values in the distribution of the electromagnetic fraction in the $\tau_\mu\tau_{\mathrm{h}}$ channel which is compatible with an excess in the $Z \rightarrow \mu\mu$ contribution where the muon is misidentified as a hadronic τ candidate. The Monte Carlo distribution is shifted with respect to data for the $\tau_e\tau_{\mathrm{h}}$ channel which is due to correlations between the variables used in

the τ trigger requirements which are applied to the data only.

A detailed study has been performed to understand the excess of simulated events in the $\tau_\mu\tau_\mathrm{h}$ channel. Data and simulation are compared in a $Z \rightarrow \mu\mu$ enriched control region defined as follows:

- Main selection up to W suppression cuts,
- 1-prong τ candidate,
- lepton $\mathrm{p_T} > 37$ GeV.

Figure 7.8 shows the number of tracks and the electromagnetic fraction of the τ candidates in the $Z \rightarrow \mu\mu$ control region. The excess of Monte Carlo events is due to the high fake rate of muons as τ leptons in the simulation. In order to get rid of fake τ candidates, a cut on the EM fraction (> 0.10) is applied only to candidates in the $\tau_\mu\tau_\mathrm{h}$ channel. The effectiveness of the cut is confirmed by the distributions of the visible invariant mass of the muon and the hadronic τ candidate shown in Figure 7.9 before and after the cut.

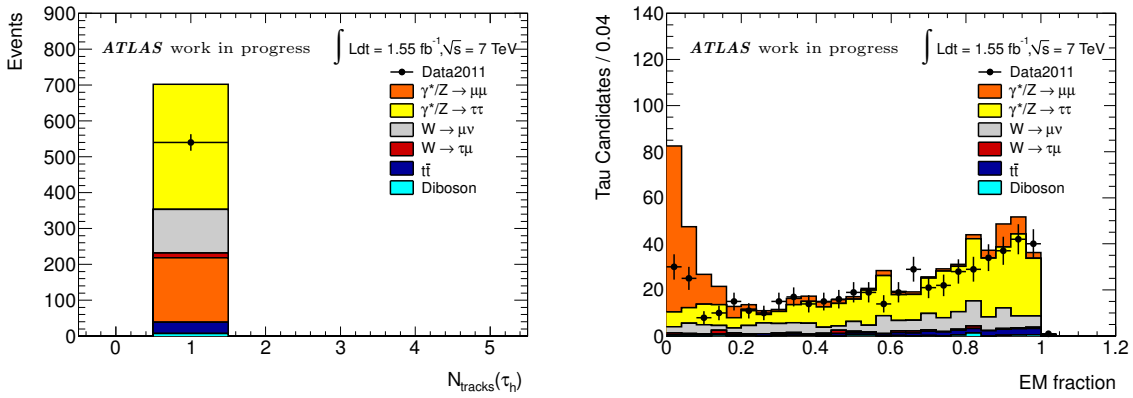

(a) (b)

Figure 7.8: The number of tracks (a) and the electromagnetic energy fraction (b) of the τ candidates in the $Z \rightarrow \mu\mu$ control region.

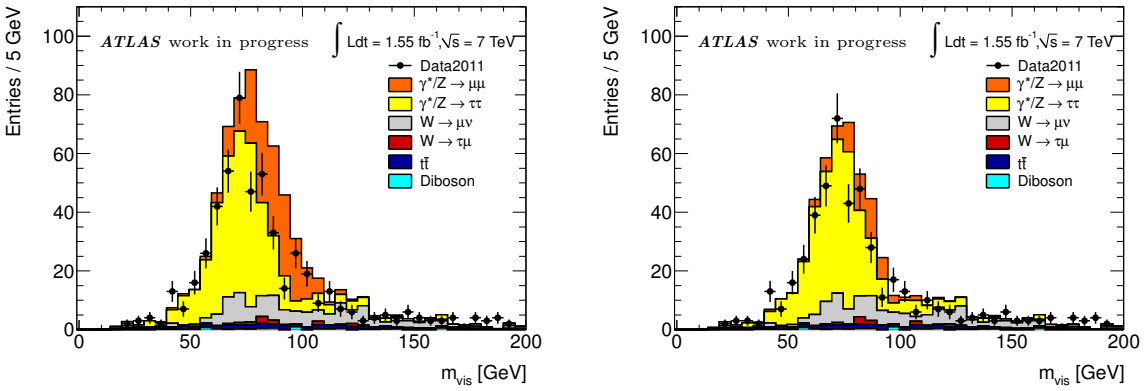

Figure 7.9: Visible μ-τ_{h} mass in the $Z \rightarrow \mu\mu$ enriched control region (a) before and (b) after the cut in the electromagnetic energy fraction. Data and simulation do not agree before the cut on the electromagnetic energy fraction. Acceptable agreement is found after the cut in the electromagnetic fraction.

7.5.4 Visible mass of the $Z \to \tau\tau$ final state

The visible mass m_{vis} is defined as the invariant mass of the muon (electron) and the hadronic τ jet. Signal events are concentrated in the mass window 35 GeV $< m_{\text{vis}} <$ 75 GeV while $Z \to \ell\ell$ events where a lepton is misidentified as a hadronic τ candidate are concentrated close to the Z mass. Within the visible mass window, the dominant background is due to multi-jet events while other electroweak and $t\bar{t}$ processes have lower impact. The Z peak is pronounced in the $\tau_e\tau_{\text{h}}$ channel because of the high fake rate of electrons as hadronic τ candidates.

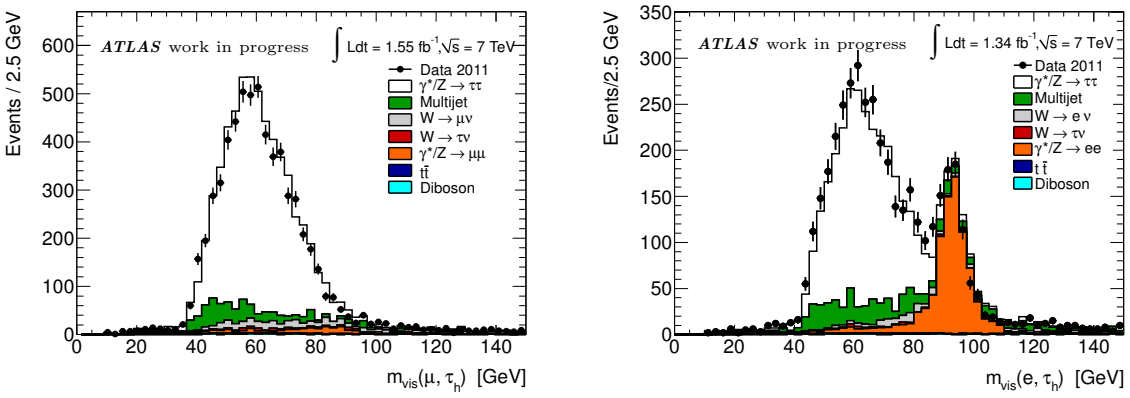

Figure 7.10: The visible mass spectrum in the $\tau_\mu\tau_{\text{h}}$ channel (left) and in the $\tau_e\tau_{\text{h}}$ channel (right). The shape of the multi-jet background is taken from the control region obtained by inversion of the charge product sign requirement and normalized to the signal region expectation (see section 7.6.3).

7.5.5 Results of the selection

The results of the $Z \to \tau\tau$ selection are summarized in Tables 7.5 and 7.6 for the $\tau_e\tau_{\text{h}}$ and $\tau_\mu\tau_{\text{h}}$ channels, respectively. The agreement between data and simulation after the selection is acceptable. The ratio between selected data and simulated events is 1.05 $\pm$ 0.02 (0.97 $\pm$ 0.02) in the $\tau_e\tau_{\text{h}}$ ($\tau_\mu\tau_{\text{h}}$) channel. From the number of selected events the cross section for $Z \to \tau\tau$ decays is determined (see section 7.7).

The distributions of the transverse momentum and the pseudorapidity of the leptons and hadronic τ candidates are shown in Figures 7.11 and 7.12. Differences between data and Monte Carlo simulation are observed in the transverse momentum distribution of the hadronic τ candidates in Fig. 7.11(d) and may be due to different τ trigger efficiencies in data and simulation. In addition, the low-p_{T} part of the spectrum is affected by higher systematic uncertainty compared to higher p_{T}.

Figures 7.13 and 7.14 show the main variables used for the signal selection after all selection cuts excluding the cut on the variable shown.

Figure 7.15 shows the distributions of the E_T^{miss} and the difference between the azimuthal angles of the lepton and the hadronic τ decay.

Figure 7.16 shows the distributions of the hadronic τ decay observables defined in section 5.3.4.

The Monte Carlo simulation describes the data well for all variables after the selection cuts.

Table 7.5: Cut flow table for the $\tau_e\tau_{\mathrm{h}}$ channel: numbers of signal and expected background events after the sequential selection cuts.

	Data 2011	$Z/\gamma^* \to \tau\tau$	$W \to e\nu$	$W \to \tau\nu$	$Z/\gamma^* \to ee$	$t\bar{t}$	Dibosons	Multi-jets
Object selection	15200(123)	3393(38)	4893(69)	306(15)	3525(38)	534(5)	174(6)	
Opposite sign	8675(93)	3087(36)	2267(47)	133(9)	1588(28)	340(4)	103(5)	1136(60)
Dilepton veto	8441(92)	3067(36)	2257(47)	133(9)	1457(27)	271(3)	97(5)	1142(58)
W cuts	4649(68)	2570(33)	221(14)	52(5)	903(22)	59(1)	18(2)	721(36)
$N_{\mathrm{tracks}}(\tau_{\mathrm{h}}) = 1$ or 3	4358(66)	2456(28)	180(11)	41(4)	879(19)	54(1)	16(1)	593(33)
$\lvert\mathrm{charge}(\tau_{\mathrm{h}})\rvert = 1$	4351(66)	2453(28)	179(11)	41(4)	878(19)	53(1)	16(1)	584(32)
$m_{\mathrm{vis}} = 35 - 75$ GeV	2600(51)	2029(25)	45(5)	18(2)	64(4)	17(1)	6(1)	300(21)

Table 7.6: Cut flow table for the $\tau_\mu\tau_{\mathrm{h}}$ channel: numbers of signal and expected background events after the sequential selection cuts.

	Data 2011	$Z/\gamma^* \to \tau\tau$	$W \to \mu\nu$	$W \to \tau\nu$	$Z/\gamma^* \to \mu\mu$	$t\bar{t}$	Dibosons	Multi-jets
Object selection	35020(187)	7857(63)	28341(243)	1862(64)	4205(39)	950(6)	352(8)	
Opposite sign	17550(133)	7059(60)	6886(86)	461(23)	1612(25)	577(5)	198(7)	1363(108)
Dilepton veto	16470(128)	7027(60)	6859(86)	459(23)	921(21)	458(5)	181(6)	1265(100)
$W cuts$	7397(86)	5788(54)	582(22)	129(10)	408(15)	102(2)	32(3)	764(44)
$N_{\mathrm{tracks}}(\tau_{\mathrm{h}}) = 1$ or 3	6445(80)	5208(51)	444(19)	103(8)	187(10)	87(2)	27(2)	564(39)
$\lvert charge(\tau_{\mathrm{h}})\rvert = 1$	6422(80)	5200(51)	442(19)	102(8)	186(10)	87(2)	27(2)	555(39)
$m_{\mathrm{vis}} = 35 - 75$ GeV	5184(72)	4544(49)	186(13)	49(5)	81(7)	31(1)	15(2)	432(30)

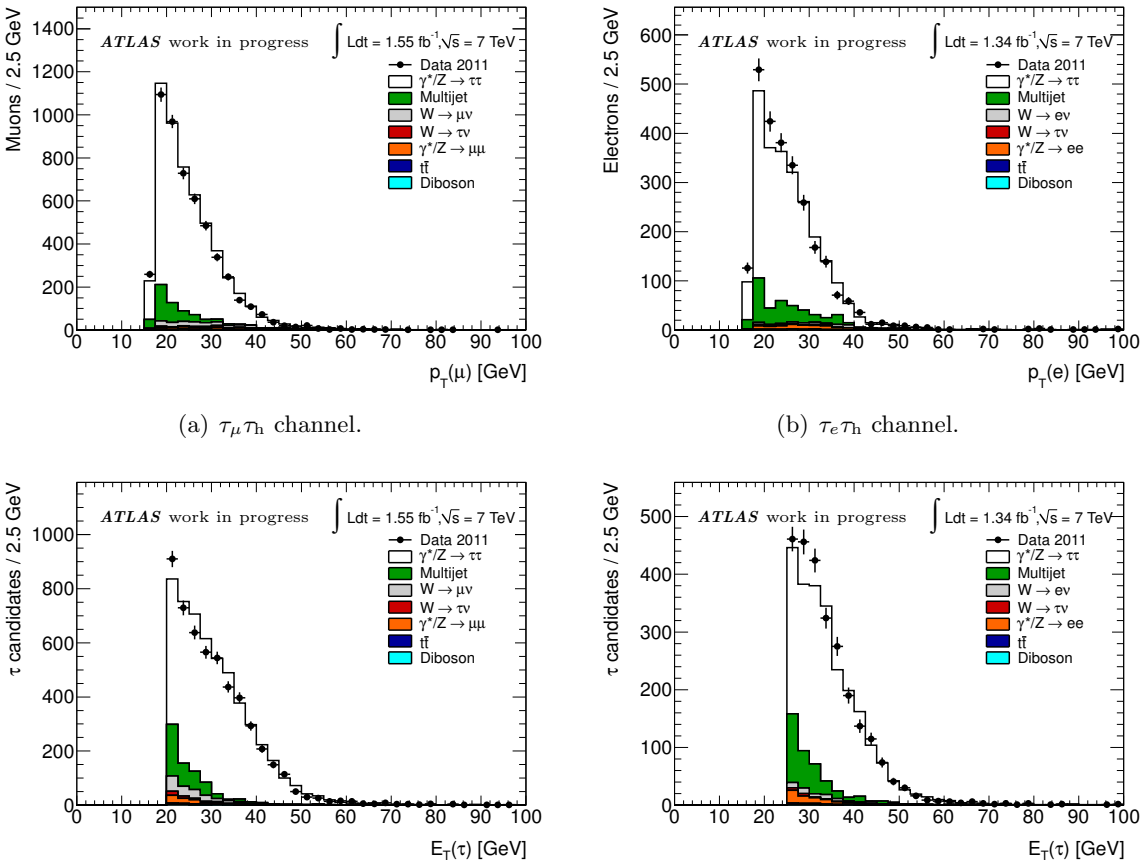

(a) $\tau_\mu\tau_\mathrm{h}$ channel.

(b) $\tau_e\tau_\mathrm{h}$ channel.

(c) $\tau_\mu\tau_\mathrm{h}$ channel.

(d) $\tau_e\tau_\mathrm{h}$ channel.

Figure 7.11: Transverse momentum distributions of leptons (top row) and hadronic τ candidates (bottom row) in the muon (left) and the electron (right) channel. The shape of the multi-jet background is estimated from the control region obtained by inversion of charge product sign requirement. It is normalized to the signal region expectation (see section 7.6.3).

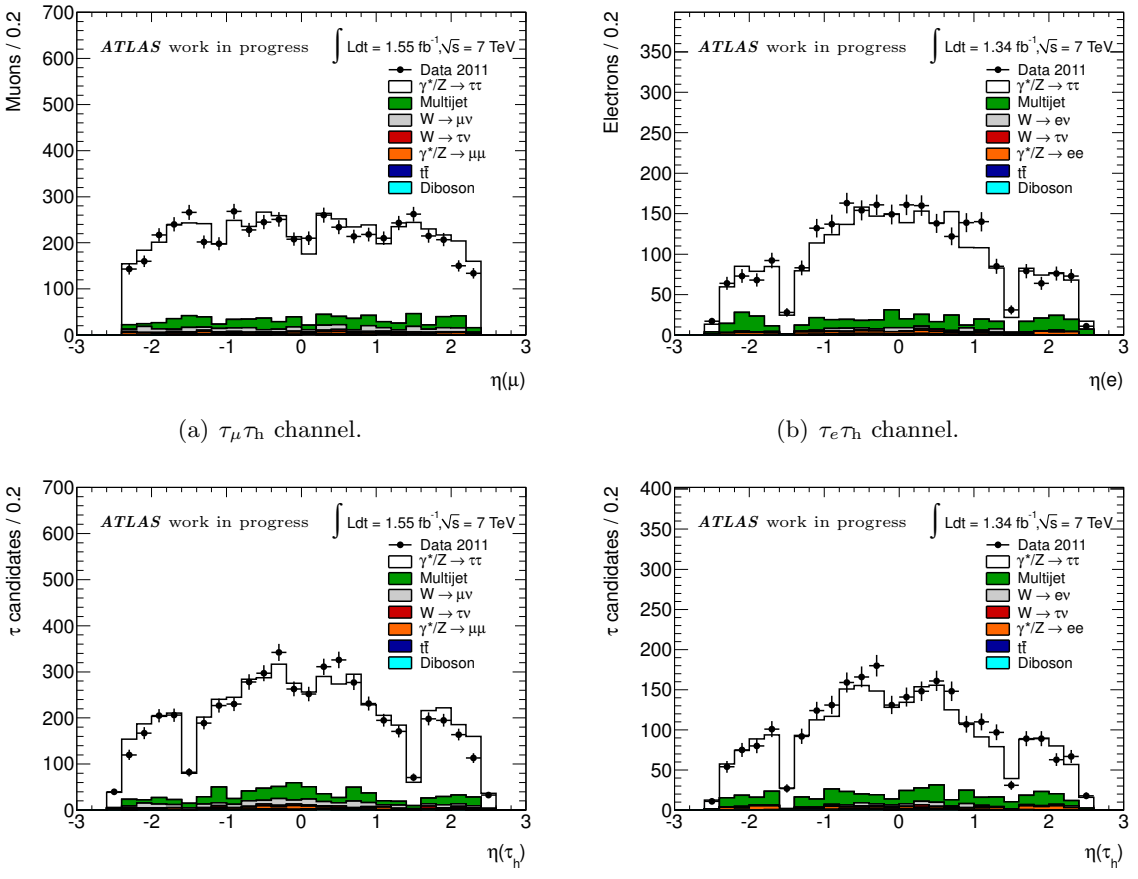

(a) $\tau_\mu\tau_\mathrm{h}$ channel.

(b) $\tau_e\tau_\mathrm{h}$ channel.

(c) $\tau_\mu\tau_\mathrm{h}$ channel.

(d) $\tau_e\tau_\mathrm{h}$ channel.

Figure 7.12: Pseudorapidity distributions of leptons (top row) and hadronic τ candidates (bottom row) in the muon (left) and the electron (right) channel. The shape of the multi-jet background is estimated from the control region obtained by inversion of charge product sign requirement. It is normalized to the signal region expectation (see section 7.6.3).

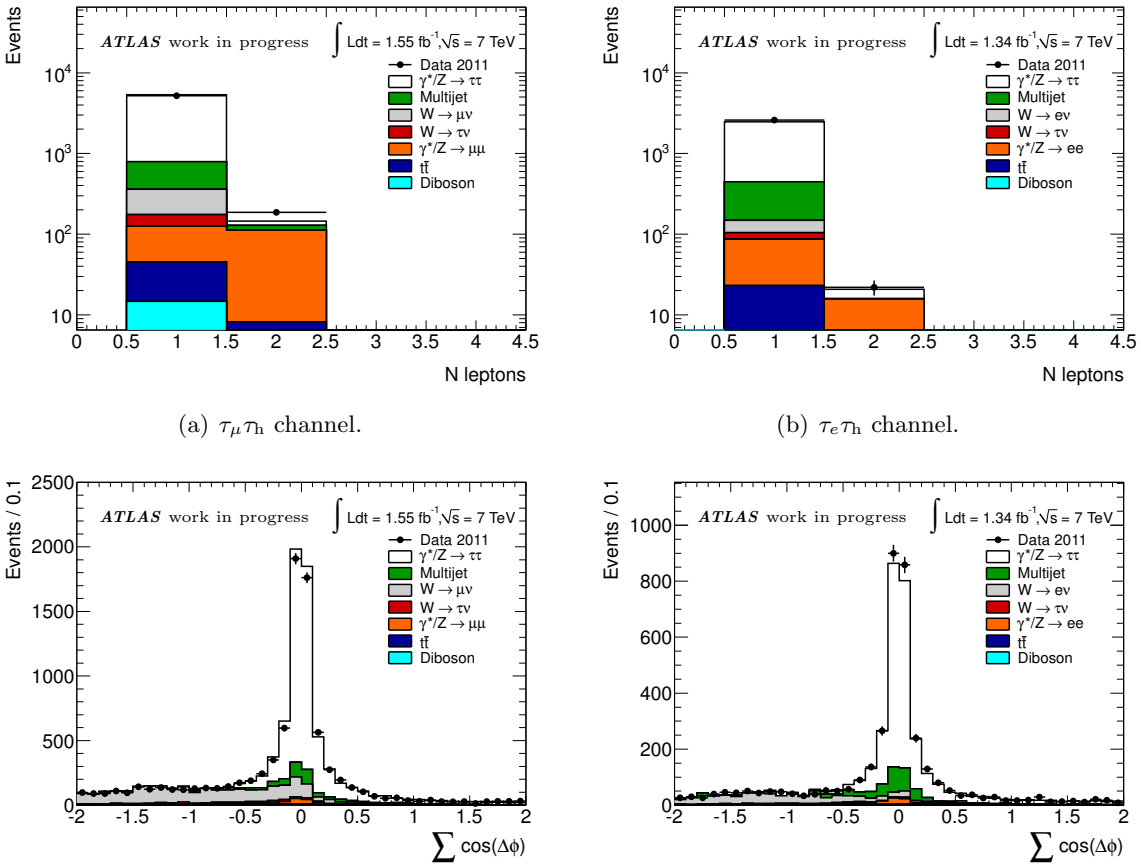

(a) $\tau_\mu\tau_\mathrm{h}$ channel.

(b) $\tau_e\tau_\mathrm{h}$ channel.

(c) $\tau_\mu\tau_\mathrm{h}$ channel.

(d) $\tau_e\tau_\mathrm{h}$ channel.

Figure 7.13: Selection variable distributions after all cuts except the one in the variable shown. The shape of the multi-jet background is estimated from the control region obtained by inversion of charge product sign requirement. It is normalized to the signal region expectation (see section 7.6.3).

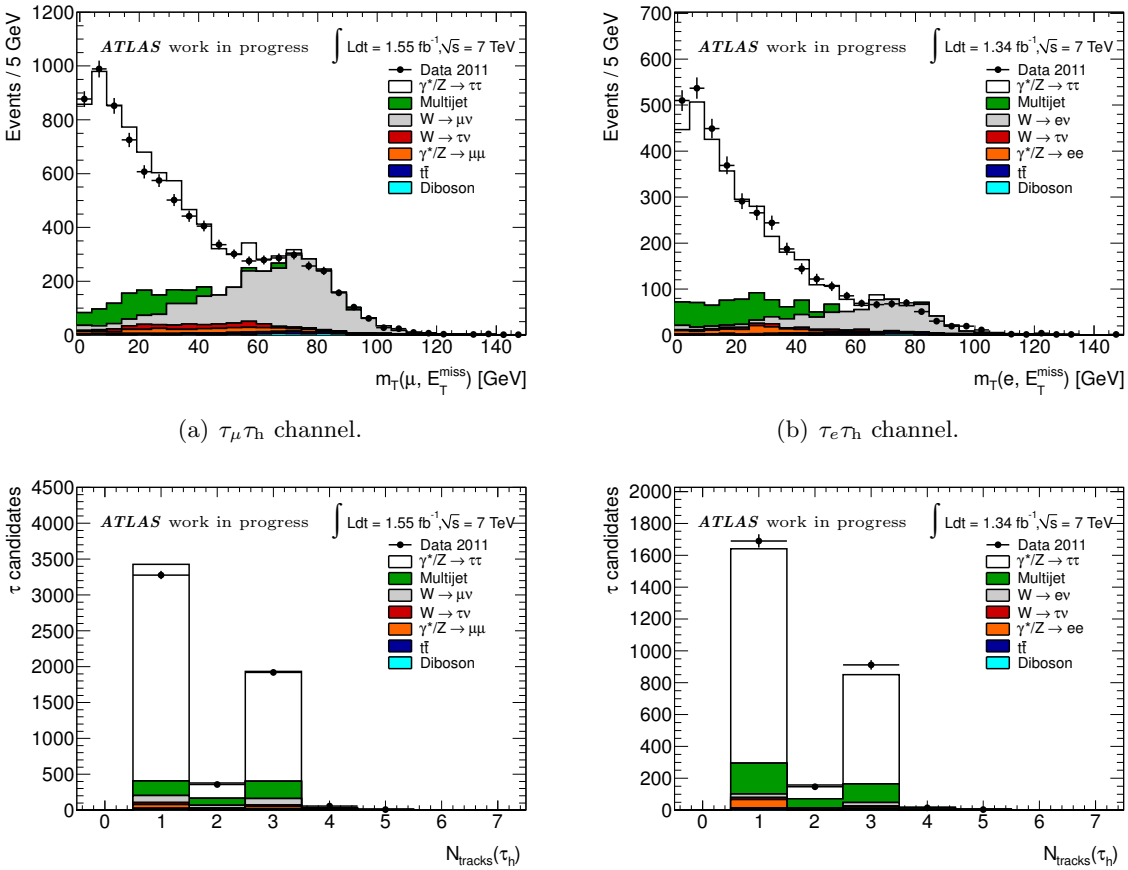

(a) $\tau_\mu\tau_\mathrm{h}$ channel.

(b) $\tau_e\tau_\mathrm{h}$ channel.

(c) $\tau_\mu\tau_\mathrm{h}$ channel.

(d) $\tau_e\tau_\mathrm{h}$ channel.

Figure 7.14: Selection variable distributions after all cuts except the one in the variable shown. The shape of the multi-jet background is estimated from the control region obtained by inversion of charge product sign requirement. It is normalized to the signal region expectation (see section 7.6.3).

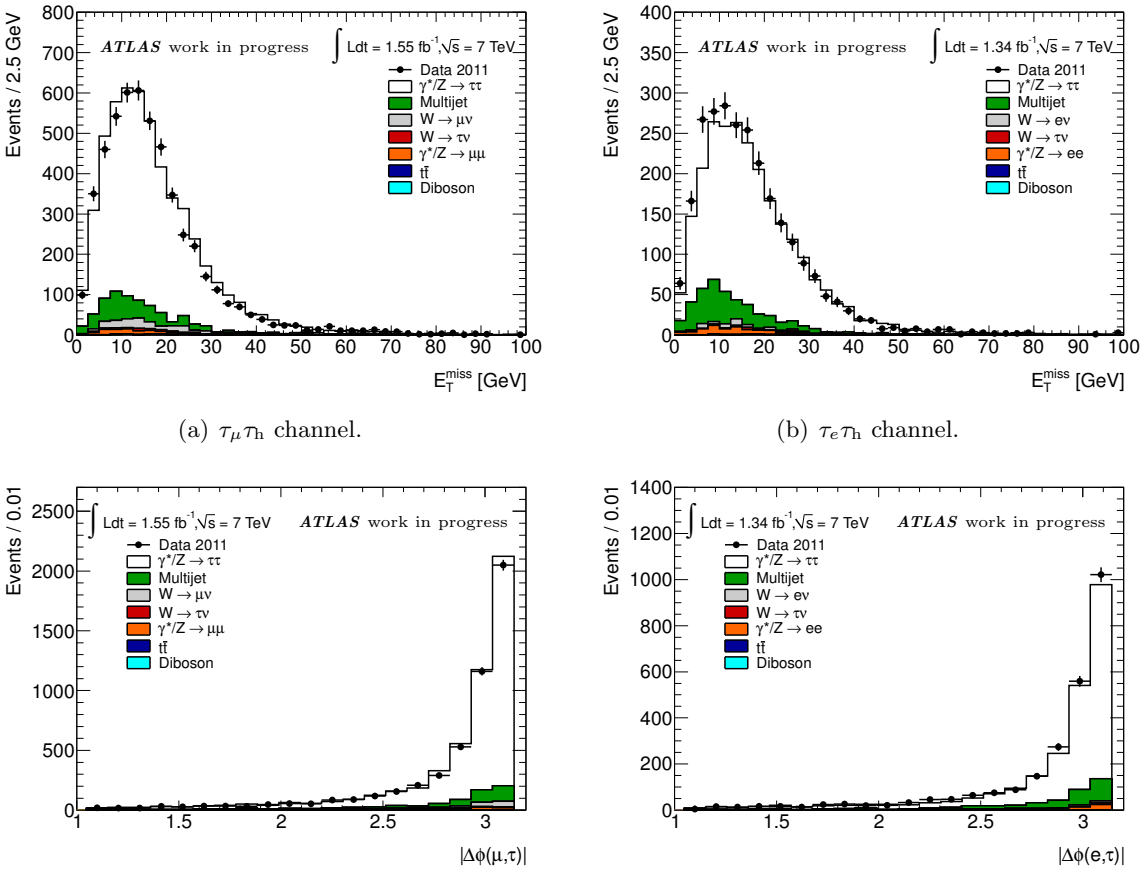

(a) $\tau_\mu\tau_{\mathrm{h}}$ channel.

(b) $\tau_e\tau_{\mathrm{h}}$ channel.

(c) $\tau_\mu\tau_{\mathrm{h}}$ channel.

(d) $\tau_e\tau_{\mathrm{h}}$ channel.

Figure 7.15: Selection variable distributions after all cuts. The shape of the multi-jet background is estimated from the control region obtained by inversion of charge product sign requirement. It is normalized to the signal region expectation (see section 7.6.3).

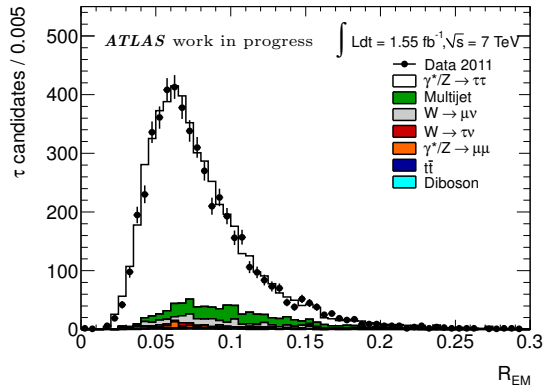

(a) Electromagnetic radius of τ candidates (Eq. 5.1).

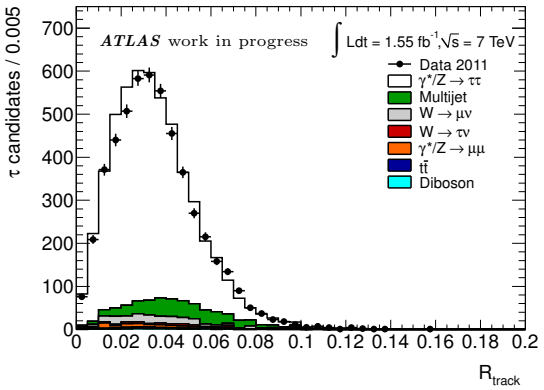

(b) Track radius of τ candidates (Eq. 5.2).

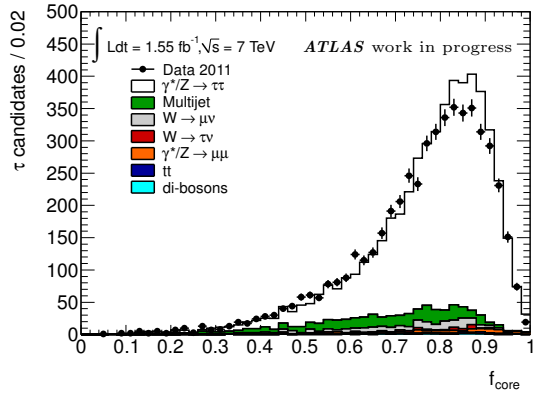

(c) Core energy fraction of τ candidates (Eq. 5.3).

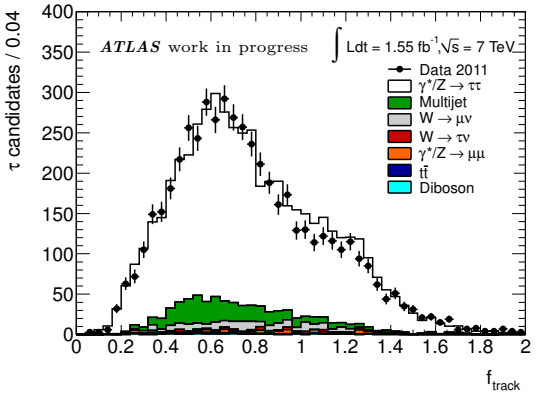

(d) Leading track momentum fraction of τ candidates (Eq. 5.4).

Figure 7.16: Identification variable distributions for the hadronic τ decay candidates after all cuts. The shape of the multi-jet background is estimated from the control region obtained by inversion of charge product sign requirement. It is normalized to the signal region expectation (see section 7.6.3).

7.6 Background estimation

Electroweak ($W \to \ell\nu$, $W \to \tau\nu$, $Z \to \ell\ell$, diboson production) and $t\bar{t}$ backgrounds estimations are obtained from Monte Carlo simulation and normalized using the theoretical prediction for the cross sections at NNLO perturbation theory. The contribution of those backgrounds is found to be small after the full selection. It is, however, important to test the reliability of the Monte Carlo predictions by enriching electroweak processes. Differences between Monte Carlo simulation and data are found in selected events with weak gauge boson production where an additional jet is misidentified as a hadronic τ candidate. Therefore, Monte Carlo event samples with W and Z bosons and jets are normalized to collision data with scale factors described in sections 7.6.1 and 7.6.2, respectively.

The production cross section of multi-jet events is higher than electroweak cross sections by several orders of magnitude. The Monte Carlo statistics is not sufficient for a reliable prediction of the number of multi-jet events. The contribution of the multi-jet background is estimated using a data-driven method described in section 7.6.3.

7.6.1 Normalization of the $W+$ jet background prediction to the data

W boson production is the main background contribution before the W suppression cuts (section 7.5.2). The background events contain a real lepton (in the case of $W \to \tau\nu$ decays, the lepton mainly comes from the τ lepton decay) together with a jet misidentified as hadronic τ candidate.

After applying the hadronic τ identification cuts the simulation overestimates the number of W events with respect to the data. A comparison between data and simulation has been performed in a W-enriched control region where events are required to pass the dilepton veto (section 7.5.1), the cuts on the number of tracks associated to the τ candidate, the charge of the τ candidate, and the charge product sign (opposite or same sign) but to fail both W suppression cuts (section 7.5.2).

Both the simulated $W \to \ell\nu$ and $W \to \tau\nu$ event numbers are rescaled by a factor k_W such that they equal the numbers of events observed in the data after subtraction of the small contamination by $Z \to \ell\ell$, $t\bar{t}$ and diboson backgrounds:

$$k_W N_W^{\mathrm{MC}} = N_{\mathrm{W}}^{\mathrm{data}} - N_{Z\to\ell\ell}^{\mathrm{MC}} - N_{t\bar{t},diboson}^{\mathrm{MC}}. \tag{7.4}$$

Due to the high transverse mass requirement, the multi-jet contamination is found to be negligible in the W control region. The k_W factors are determined separately for opposite sign and same sign charge of the lepton and hadronic τ decay candidate since the misidentification rate of τ candidates is different for jets originating from quarks and from gluons. The fraction of quark jets is higher than the gluon component in the opposite sign selection while the latter is dominant in the same sign selection.

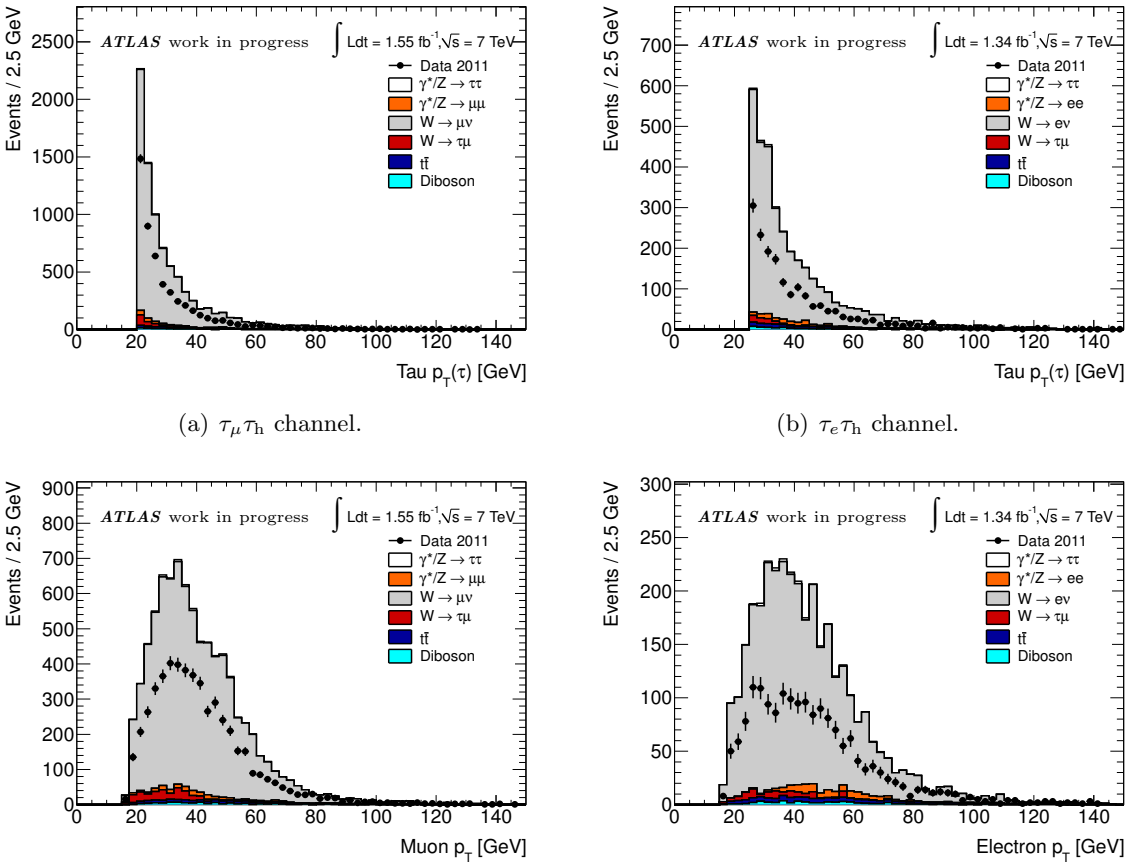

(a) $\tau_\mu\tau_\mathrm{h}$ channel.

(b) $\tau_e\tau_\mathrm{h}$ channel.

(c) $\tau_\mu\tau_\mathrm{h}$ channel.

(d) $\tau_e\tau_\mathrm{h}$ channel.

Figure 7.17: Transverse momentum distributions in the W-enriched control region before the application of the normalization factors.

The k_W factors are

$$k_W = \begin{cases} 0.44 \pm 0.02 \text{ (stat.)} & \tau_\mathrm{e}\tau_\mathrm{h} \text{ channel, opposite sign}, \\ 0.56 \pm 0.04 \text{ (stat.)} & \tau_\mathrm{e}\tau_\mathrm{h} \text{ channel, same sign}, \\ 0.54 \pm 0.01 \text{ (stat.)} & \tau_\mu\tau_\mathrm{h} \text{ channel, opposite sign}, \\ 0.74 \pm 0.03 \text{ (stat.)} & \tau_\mu\tau_\mathrm{h} \text{ channel, same sign}. \end{cases} \tag{7.5}$$

As can be seen, there are differences between the values observed in the $\tau_\mu\tau_\mathrm{h}$ and in the $\tau_e\tau_\mathrm{h}$ channel which can likely be attributed to the τ trigger requirements in the $\tau_e\tau_\mathrm{h}$ channel.

7.6.2 Normalization of the Z + jet background prediction to the data

$Z \to \ell\ell$ production is one of the main backgrounds. This process contributes in two different ways depending on the source of the hadronic τ misidentification. Either a jet in ($Z \to \ell\ell$)

+ jets events is misidentified as a hadronic τ candidate or one of the two leptons in $Z \to \ell\ell$ decays is misidentified as a hadronic τ candidate. The latter background mainly contributes in the electron channel since the τ lepton misidentification probability is much higher for electrons than for muons, even after the electron veto.

As for the W + jet background, the number of simulated $Z \to \ell\ell$ + jet events is normalized to the data in a Z-enriched control sample which is selected by requiring two electrons (muons) with invariant mass close to the Z mass. Figure 7.18 shows the hadronic τ momentum distribution in the Z control region which is dominated by $Z \to \ell\ell$ events such that no background subtraction is needed.

The number of Monte Carlo events is higher than the number of data events which is corrected for by a scale factor k_Z:

$$k_Z = \begin{cases} 0.39 \pm 0.05 \text{ (stat.)}, & \tau_e\tau_h \text{ channel}, \\ 0.57 \pm 0.04 \text{ (stat.)}, & \tau_\mu\tau_h \text{ channel}. \end{cases} \tag{7.6}$$

The k_Z factors are applied only to those simulated $Z \to \ell\ell$ events where the hadronic τ cannot be matched to a true lepton.

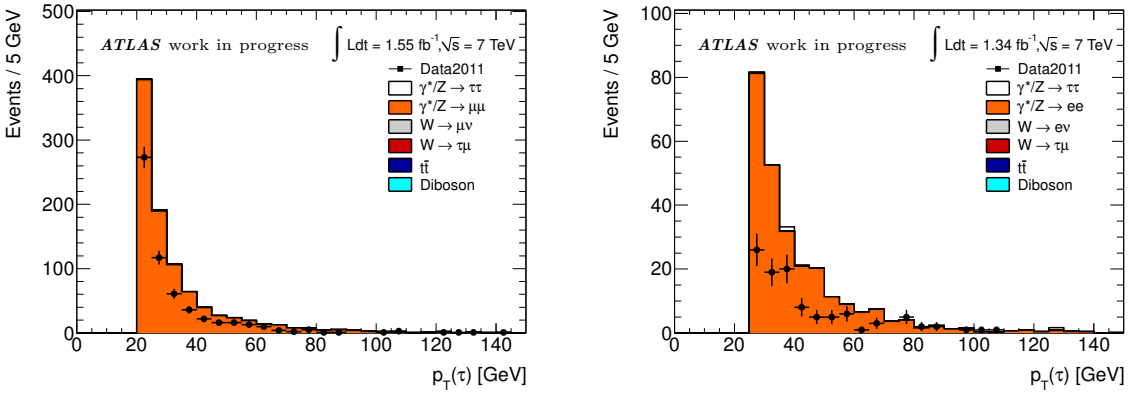

(a) $\tau_\mu\tau_h$ channel. (b) $\tau_e\tau_h$ channel.

Figure 7.18: Transverse momentum distributions of hadronic τ candidates in the Z-enriched control sample. The Monte Carlo simulation overestimates the number of events in the control region compared to the data in both lepton channels after the identification of τ candidates.

7.6.3 Estimation of the multi-jet background from data

Multi-jet events are one of the main backgrounds composed of a real or a fake lepton arising from a jet and a jet misidentified as a hadronic τ candidate. Lepton isolation cuts are applied to reduce this background but due to the high cross section the residual background cannot be neglected and needs to be estimated. An entirely data-driven technique (the *ABCD method*) is used since Monte Carlo simulation is not reliable for this purpose due to the incorrect modeling of the τ misidentification rate.

Four selection regions are defined with different signal and background contributions. In all four regions the same cuts are applied except for the opposite charge sign and the isolation requirements:

- A: signal region with isolated lepton and the opposite charge sign requirement.
- B: control region with isolated lepton and the same charge sign requirement.
- C: control region with inverted lepton isolation cuts and opposite charge sign requirement.
- D: control region with inverted lepton isolation cuts and same charge sign requirement.

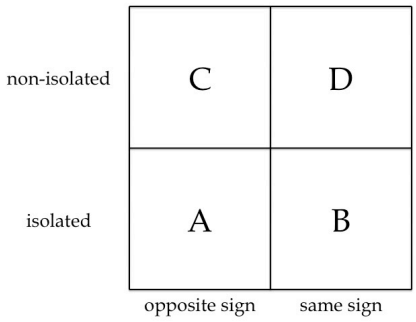

Figure 7.19: Illustration of the ABCD method.

The contributions of the different processes to the signal and control regions are shown in Table 7.7. The numbers of multi-jet data events in the control regions are calculated by subtracting the residual electroweak and $t\bar{t}$ backgrounds contributions:

$$N^i_{\text{Multi-jet}} = N^i_{\text{Data}} - N^i_{Z\to\tau\tau} - N^i_{Z\to\ell\ell} - N^i_{t\bar{t},\text{diboson}} - N^i_{W\to\ell\nu} - N^i_{W\to\tau\nu}, \quad \text{for } i = \text{B, C, D.} \tag{7.7}$$

The method takes advantage of the fact that the signal events contain almost exclusively isolated leptons with charges opposite to the ones of the τ candidates. Therefore signal contributions can efficiently be excluded in all control regions. A contamination with signal events is present in region C in the $\tau_\mu\tau_\text{h}$ channel (see Table 7.7) due to the requirement of tight muon isolation both at the trigger level and for the muon selection. The signal contribution is subtracted along with the electroweak backgrounds introducing a 5% systematic uncertainty on the normalization which has negligible effect on the measured $Z \to \tau\tau$ cross section.

The number of multi-jet events in the signal region A is calculated according to the relation

$$N^A_{\text{Multi-jet}} = \frac{N^C_{\text{Multi-jet}}}{N^D_{\text{Multi-jet}}} N^B_{\text{Multi-jet}} = R_{\text{OSSS}} N^B_{\text{Multi-jet}} \tag{7.8}$$

using the measured ratios of events in region C and D

$$R_{\mathrm{OSSS}} = \begin{cases} 1.06 \pm 0.03 \text{ (stat.)} & \tau_{\mathrm{e}}\tau_{\mathrm{h}} \text{ channel,} \\ 1.13 \pm 0.04 \text{ (stat.)} & \tau_{\mu}\tau_{\mathrm{h}} \text{ channel,} \end{cases} \tag{7.9}$$

which is compatible for the two lepton channels and close to unity. The method relies on the property of R_{OSSS} to be independent of the lepton isolation requirement. This is verified by calculating the ratio for C' and D' modified control regions by inverting the τ identification requirements for the $\tau_{\mu}\tau_{\mathrm{h}}$ channel.

In the $\tau_e\tau_{\mathrm{h}}$ channel events have to pass the trigger requirement selecting events with one identified τ candidate making the inversion of the τ identification impossible.

Figure 7.20 shows R_{OSSS} as a function of the isolation variables. The modified ratio is still within the statistical error band of the nominal value of Eq. 7.9. The deviation of the last modified points in Fig. 7.20(a) and the average of the other three is used for the evaluation of the systematic uncertainty in the $\tau_{\mu}\tau_{\mathrm{h}}$ channel and also applied to the $\tau_e\tau_{\mathrm{h}}$ channel (Eq. 7.10).

The variation of the R_{OSSS} as a function of the selected cuts was also studied (Fig. 7.21). A small dependence on the cuts is found in the $\tau_e\tau_{\mathrm{h}}$ channel where the ratio drops when the visible mass cut is applied. The associated systematic uncertainty is determined as the difference of the average of the ratios at different stages of the cut flow (excluding the visible mass cut) to the value in Eq. 7.9.

The final result is

$$R_{\mathrm{OSSS}} = \begin{cases} 1.06 \pm 0.03 \text{ (stat.)} \pm 0.02 \text{ (iso sys.)} \pm 0.01 \text{ (cutflow sys.),} & \tau_{\mathrm{e}}\tau_{\mathrm{h}} \text{ channel,} \\ 1.13 \pm 0.04 \text{ (stat.)} \pm 0.02 \text{ (iso sys.),} & \tau_{\mu}\tau_{\mathrm{h}} \text{ channel.} \end{cases} \tag{7.10}$$

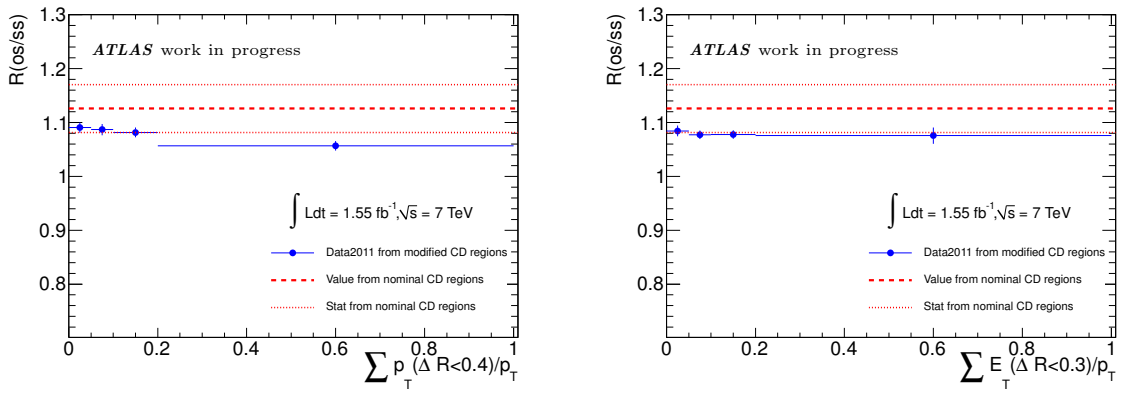

Figure 7.20: Ratio between opposite sign and same sign events for standard (with statistical error band) and modified control regions C and D (see text), as a function of the isolation variables for the $\tau_{\mu}\tau_{\mathrm{h}}$ channel.

Table 7.7: Number of events in the regions ABCD used for the multi-jet background estimation.

	$\tau_\mu\tau_{\text{had}}$		$\tau_e\tau_{\text{had}}$	
	A	B	A	B
data	5184	577	2600	353
$\gamma/Z \to \tau\tau$	4544	44	2029	19
$\gamma/Z \to \ell\ell$	81	57	64	29
$W \to \ell\nu$	186	64	45	15
$W \to \tau\nu$	49	22	18	5
$t\bar{t}$	31	5	17	2
Dibosons	15	1	6	1
Multi-jet	-	384	-	282
	C	D	C	D
data	1728	1352	2626	2403
$\gamma/Z \to \tau\tau$	196	1	71	4
$\gamma/Z \to \ell\ell$	2	4	3	-
$W \to \ell\nu$	12	1	2	-
$W \to \tau\nu$	2	-	1	-
$t\bar{t}$	2	-	3	1
Dibosons	-	-	-	-
Multi-jet	1514	1345	2546	2397

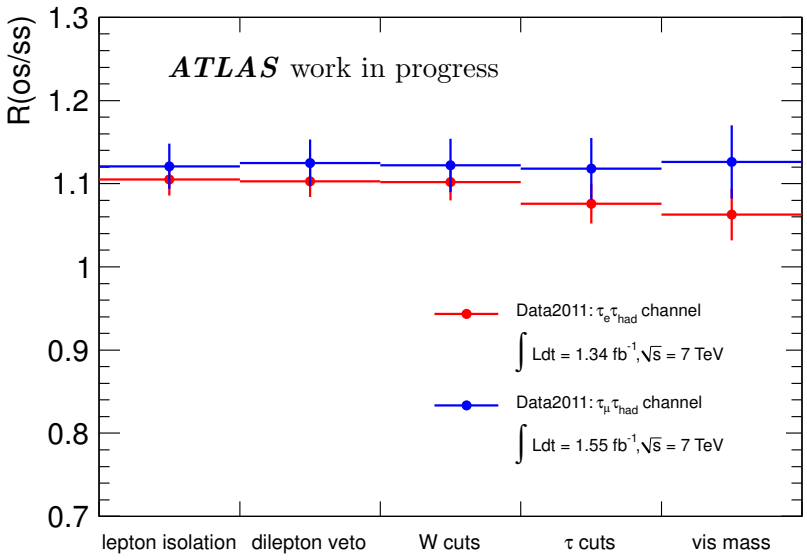

Figure 7.21: R_{OSSS} at different steps of the event selection after lepton isolation, dilepton veto, W background suppression cuts, hadronic τ cleaning and the visible mass cut.

7.7 Calculation of the $Z \to \tau\tau$ cross section

The $Z \to \tau\tau$ cross section is determined from the observed numbers of events according to the relation:

$$\sigma(Z \to \tau\tau) \times BR(\tau \to l\nu\nu) \times BR(\tau \to \tau_{\text{had}}\nu) = \frac{N_{\text{obs}} - N_{\text{bkg}}}{A_Z \cdot C_Z \cdot \mathcal{L}} \tag{7.11}$$

where

- N_{obs} is the number of observed data events,
- N_{bkg} the number of estimated background events,
- A_Z the acceptance of the geometric and kinematic cuts,
- C_Z the efficiency of the signal selection and
- $\mathcal{L}$ the integrated luminosity.

Determination of the acceptance It corrects for the finite pseudorapidity coverage of the detector. The acceptance A_Z is determined using PYTHIA Monte Carlo event generator [32] at lowest order in perturbation theory with the modified LO parton density function MRSTLO*[57] and the ATLAS detector simulation. It is given by the ratio

$$A_Z = \frac{N^{\text{fiducial}}}{N^{\text{generated}}} \tag{7.12}$$

where $N^{\text{generated}}$ is the number of generated $Z \to \tau\tau$ events, with a $\tau\tau$ invariant mass within [66-116] GeV and N^{fiducial} the number of generated events in the fiducial regions summarized in Table 7.8. Photon radiation by the τ leptons and their decay products is taken into account.

Determination of the signal efficiency The signal selection efficiency C_Z is calculated within the fiducial regions in Table 7.8 according to the relation

$$C_Z = \frac{N^{\text{selection}}}{N^{\text{fiducial}}} \tag{7.13}$$

where $N^{\text{selection}}$ is the number of signal events after the full selection simulated with the ALPGEN generator [35] and corrected with the scale factors, determined by the data driven methods, while N^{fiducial} is the same as the numerator of A_Z in Eq. 7.12.

The results for A_Z and C_Z are given in Table 7.9 with statistical errors.

The splitting of the correction factor in acceptance and selection efficiency is done because of the different systematic errors (see below).

Table 7.8: Fiducial regions for the $Z \to \tau\tau$ cross section measurement.

	$\tau_\mu\tau_\mathrm{h}$ channel	$\tau_e\tau_\mathrm{h}$ channel
Lepton	$p_T > 17$ GeV	$E_T > 17$ GeV, $\lvert\eta\rvert < 2.47$
Lepton	$\lvert\eta\rvert < 2.4$	$\lvert\eta\rvert < 2.47$, excluding $1.37 < \lvert\eta\rvert < 1.52$
Tau	$E_T > 20$ GeV	$E_T > 25$ GeV, $\lvert\eta\rvert < 2.47$
Tau	$\lvert\eta\rvert < 2.47$, excluding $1.37 < \lvert\eta\rvert < 1.52$	$\lvert\eta\rvert < 2.47$, excluding $1.37 < \lvert\eta\rvert < 1.52$
Event	$\Sigma \cos\Delta\phi > -0.15$, $m_T < 50$ GeV, M_vis within [35, 75] GeV	

Table 7.9: Acceptance A_Z and efficiency C_Z of the $Z \to \tau\tau$ event selection from [1].

	$\tau_\mu\tau_\mathrm{h}$	$\tau_e\tau_\mathrm{h}$
A_Z	0.0976 ± 0.0002 (stat.)	0.0687 ± 0.0002 (stat.)
C_Z	0.1417 ± 0.0016 (stat.)	0.1009 ± 0.0013 (stat.)

Determination of the luminosity The measurement of the luminosity and the associated uncertainty are described in [58]. The luminosity for the measurement of the $Z \to \tau\tau$ cross section is calculated with a web-based tool [54] from the luminosities of each run present in the GRL.

7.7.1 Results

In this section, the results of the $Z \to \tau\tau$ cross section measurement are presented in the semi-leptonic final states and combined with the results for the leptonic final state $\tau_e\tau_\mu$ from [1].

Fiducial cross section The fiducial cross section is defined as the cross section within the kinematical and geometrical cuts on the particles in the final state. It is calculated using Eq. 7.11 with $A_Z = 1$, i.e. without acceptance correction from the fiducial region to the phase space. The fiducial cross sections for inclusive $Z \to \tau\tau$ production in the semileptonic and leptonic final states are given by

$$\sigma^{fid}(Z \to \tau\tau) \times BR(\tau \to \mu\,\nu\,\nu) \times BR(\tau \to \tau_{had}\,\nu) = 20.0 \pm 0.3(\mathrm{stat}) \pm 2.0(\mathrm{syst}) \pm 0.7(\mathrm{lumi})\ \mathrm{pb} \tag{7.14}$$

for the $\tau_\mu\tau_\mathrm{h}$ channel,

$$\sigma^{fid}(Z \to \tau\tau) \times BR(\tau \to e\,\nu\,\nu) \times BR(\tau \to \tau_{had}\,\nu) = 15.9 \pm 0.4(\mathrm{stat}) \pm 2.0(\mathrm{syst}) \pm 0.6(\mathrm{lumi})\ \mathrm{pb} \tag{7.15}$$

for the $\tau_e\tau_\mathrm{h}$ channel and

$$\sigma^{fid}(Z \to \tau\tau) \times BR(\tau \to e\,\nu\,\nu) \times BR(\tau \to \mu\,\nu\,\nu) = 4.7 \pm 0.2(\mathrm{stat}) \pm 0.4(\mathrm{syst}) \pm 0.2(\mathrm{lumi})\ \mathrm{pb} \tag{7.16}$$

for the $\tau_e\tau_\mu$ channel.

The total cross-section The corresponding total cross sections after additional acceptance corrections, except for the reconstructed Z mass window, are given by

$$\begin{aligned}\sigma(Z \to \tau\tau, m_{inv} = 66 - 116\ GeV) \times BR(\tau \to \mu\,\nu\,\nu) \times BR(\tau \to \tau_{had}\,\nu) = \\ = 205.2 \pm 3.4(\text{stat}) \pm 21.3(\text{syst}) \pm 7.6(\text{lumi})\ \text{pb}\end{aligned} \tag{7.17}$$

for the $\tau_\mu\tau_\text{h}$ channel,

$$\begin{aligned}\sigma(Z \to \tau\tau, m_{inv} = 66 - 116\ GeV) \times BR(\tau \to e\,\nu\,\nu) \times BR(\tau \to \tau_{had}\,\nu) = \\ = 230.9 \pm 5.5(\text{stat}) \pm 30.5(\text{syst}) \pm 8.5(\text{lumi})\ \text{pb}\end{aligned} \tag{7.18}$$

for the $\tau_e\tau_\text{h}$ channel and

$$\begin{aligned}\sigma(Z \to \tau\tau, m_{inv} = 66 - 116\ GeV) \times BR(\tau \to e\,\nu\,\nu) \times BR(\tau \to \mu\,\nu\,\nu) = \\ = 59.8 \pm 2.0(\text{stat}) \pm 5.3(\text{syst}) \pm 2.2(\text{lumi})\ \text{pb}\end{aligned} \tag{7.19}$$

for the $\tau_e\tau_\mu$ channel.

The inclusive cross section The inclusive cross sections are calculated from the corresponding total cross section above using the τ decay branching ratios

$$BR(\tau \to \mu\,\nu\,\nu) \times BR(\tau \to \tau_{had}\,\nu) = 0.1125 \pm 0.0005,$$

$$BR(\tau \to e\,\nu\,\nu) \times BR(\tau \to \tau_{had}\,\nu) = 0.1157 \pm 0.0005,$$

$$BR(\tau \to \mu\,\nu\,\nu) \times BR(\tau \to e\,\nu\,\nu) = 0.0310 \pm 0.0001,$$

from [14] and multiplied by a factor 2 to account for the two possible combinations of the τ decays in the final state

$$BR(\tau_1 \to e\,\nu\,\nu) \times BR(\tau_2 \to \tau_{had}\,\nu) + 1 \leftrightarrow 2\ .$$

The following cross sections are calculated:

$$\sigma(Z \to \tau\tau, m_{inv} = 66 - 116\ GeV) = 912.4 \pm 15.0(\text{stat}) \pm 94.7(\text{syst}) \pm 33.7(\text{lumi})\ \text{pb} \tag{7.20}$$

for the $\tau_\mu\tau_\text{h}$ channel,

$$\sigma(Z \to \tau\tau, m_{inv} = 66 - 116\ GeV) = 998.1 \pm 23.7(\text{stat}) \pm 131.9(\text{syst}) \pm 36.9(\text{lumi})\ \text{pb} \tag{7.21}$$

for the $\tau_e\tau_\text{h}$ channel and

$$\sigma(Z \to \tau\tau, m_{inv} = 66 - 116\ GeV) = 964.4 \pm 32.0(\text{stat}) \pm 85.8(\text{syst}) \pm 35.7(\text{lumi})\ \text{pb} \tag{7.22}$$

for the $\tau_e\tau_\mu$ channel.

7.7.2 Combination of the results and comparison with theoretical predictions

The inclusive cross sections measured in the three different channels can be combined. In this thesis, the results of the combination are shown for completeness. Details can be found in [1].

For the combination the different systematic uncertainties in the three different channels are either assumed to be fully correlated or fully uncorrelated. Table 7.10 shows the correlations for the different sources of systematic uncertainty. The result of the combination is

$$\sigma(Z \rightarrow \tau\tau,\ 66 < m_{\text{inv}} < 116\ GeV) = 920.6 \pm 16.7(\text{stat}) \pm 78.1(\text{syst}) \pm 34.0(\text{lumi})\ \text{pb}\ . \quad (7.23)$$

Table 7.10: Systematic uncertainties in the inclusive $Z \rightarrow \tau\tau$ cross section measurement (see section 7.8) and the assumed correlation between the three channels. 100% correlation between systematic uncertainties is indicated by 'X' and 0% correlation by '–'.

Systematic effect	$\tau_\mu\tau_h$	$\tau_e\tau_h$	$\tau_e\tau_\mu$
muon efficiency scale factors	X	–	X
electron efficiency scale factors	–	X	X
τ identification efficiency	X	X	–
τ trigger efficiency	–	–	–
muon p_T resolution	X	–	X
electron p_T resolution	–	X	X
$e \rightarrow \tau$ misidentification rate	–	–	–
e/τ/jet/MET energy scale	X	X	X
W/Z background normalization factors	–	–	–
Multi-jet background estimation	X	X	X
Monte Carlo background cross sections	X	X	X
Monte Carlo statistics	–	–	–
Luminosity	X	X	X
Acceptance factor A_Z	X	X	X

In Figure 7.22, inclusive cross section measurement for $Z \rightarrow \tau\tau$ production are summarized and compared with the theoretical prediction (960 $\pm$ 50) pb. The central value of the theoretical prediction is determined with the FEWZ package [59][60] using the MSTW 2008 NNLO PDF set [61]. The uncertainty is given by the knowledge on α_S and the PDF set used. The combined cross-section measurement by ATLAS for $Z \rightarrow \mu\mu$ and $Z \rightarrow ee$ production is taken from [62] and is also in good agreement with the measurements here in the semileptonic final states.

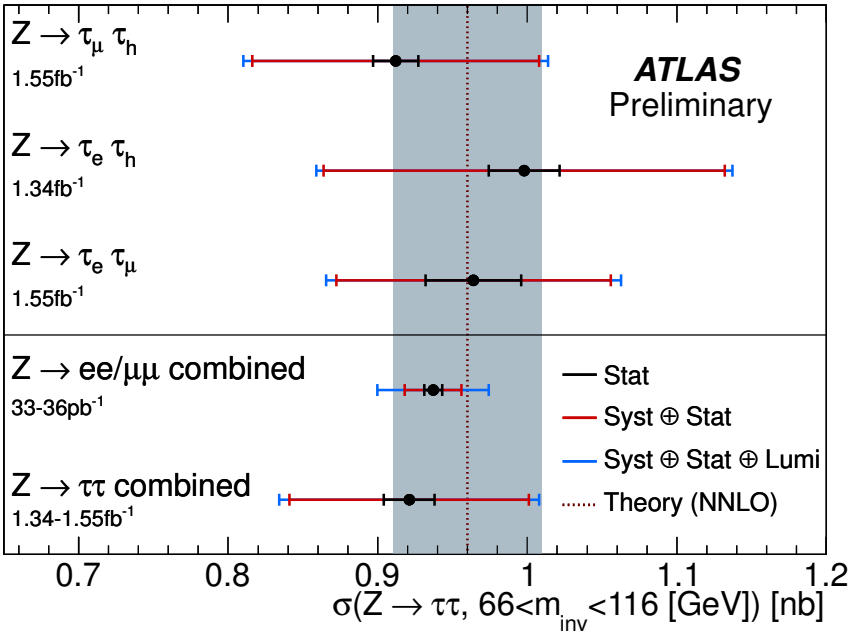

Figure 7.22: Comparison between the inclusive cross section measurements for $Z \to \tau\tau$ production and the theoretical prediction (gray band). The cross section measurement for the $Z \to \mu\mu$ and $Z \to ee$ final states are taken from [62].

7.8 Estimation of systematic uncertainties

The following sources of systematic uncertainties are taken into account for the cross section measurement:

- object reconstruction uncertainties mainly related to efficiency scale factors and energy scale determination and
- systematic uncertainties from the background estimation and the W/Z background normalization.

These systematic uncertainties affect the number of background events (numerator of Eq. 7.11) and the number of signal events via the efficiency term C_Z (denominator of Eq. 7.11).

For each upwards and downwards variation by one standard deviation of these quantities with respect to the nominal values, the cross section is recalculated. The variation of the cross section is the associated systematic error. For each systematic variation, the normalization factors and the multi-jet background are recalculated.

Table 7.12 summarizes the systematic error contributions to the measured cross section. The dominant contribution comes from the energy scale of τ candidates in both lepton channels, as already observed in the analysis using 2010 data [48].

7.8.1 Lepton reconstruction, isolation and trigger efficiency

Leptons selected for the analysis passed different requirements. Lepton reconstruction, isolation and trigger efficiency scale factors are applied to match the Monte Carlo prediction to the data. The total error associated to the product of the scale factors is calculated as the quadratic sum of the statistical and systematic uncertainties of each contribution.

Lepton reconstruction The muon reconstruction efficiency is determined with the $Z \to \mu\mu$ tag-and-probe method. A systematic uncertainty on the muon reconstruction efficiency scale factors of 0.002 [44] is used and it is more conservative than the error estimated in section 6.2.

The electron reconstruction and identification efficiency is determined with systematic errors with the $Z \to ee$ and the $W \to e\nu$ tag-and-probe method (see [37]). Results are combined to reduce the systematic uncertainty.

Lepton isolation The muon isolation efficiency is determined for reconstructed muons using the $Z \to \mu\mu$ tag-and-probe method (see section 6.3). A systematic uncertainty is associated to the muon isolation scale factors.

The electron isolation efficiency is measured including systematic errors as a function of η and E_T with the $Z \to ee$ tag-and-probe method for reconstructed and identified electrons (see [1]).

Lepton trigger The muon trigger efficiency is measured with the $Z \to \mu\mu$ tag-and-probe method for reconstructed and isolated muons. Scale factors are determined for different regions of the η-ϕ plane (see section 6.4) and a constant systematic error is associated taking into account also the small dependence of the efficiency on the data periods.

The electron trigger efficiency is measured with the $W \to e\nu$ tag-and-probe method (see [1]) for reconstructed electrons and scale factors with systematic uncertainties are derived.

7.8.2 τ trigger efficiency

The τ trigger `EF_tau16_loose` is required for the $\tau_e\tau_{\mathrm{h}}$ channel. The trigger efficiency is determined from data as a function of the transverse momentum for 1-prong and multi-prong τ candidates with the $Z \to \tau\tau$ tag-and-probe method for identified hadronic τ candidates. Details of the method and the calculation of the systematic uncertainty can be found in [1].

7.8.3 Hadronic τ identification and misidentification rate

The efficiency and fake rate of the hadronic τ decay identification are measured in $Z \to \tau\tau$ and $W \to \tau\nu$ events in 2011 data [41]. The main backgrounds taken into account are jets and electrons.

A systematic uncertainty of 5.1% has been estimated for the identification efficiency of all processes involving hadronic τ candidates identified with the BDT medium. No systematic uncertainty is assigned to the misidentification probability of jets as τ candidates since the main backgrounds from W/Z and multi-jet events are estimated from data (see section 7.6) with an associated systematic uncertainty already taken into account. The misidentification probability of electrons is reduced using a tight electron veto. $|\eta|$ dependent fake rate correction factors were calculated using the $Z \to ee$ tag-and-probe method and their systematic uncertainty is included.

7.8.4 Lepton momentum resolution

The lepton transverse momentum resolution in the simulation is different from the one measured in data. A smearing procedure is applied to the $\mathrm{p_T}$ distribution for Monte Carlo simulated events. The systematic uncertainty is estimated by varying the smearing parameters $\pm$ 1 standard deviation.

7.8.5 Energy scale uncertainty

The energy scale systematic uncertainties are evaluated simultaneously for electrons, τ candidates and E_T^{miss} in the $\tau_e\tau_{\mathrm{h}}$ channel and for τ candidates and E_T^{miss} only in the $\tau_\mu\tau_{\mathrm{h}}$ channel.

The energy of the electrons is scaled either up and down depending on their energy and pseudorapidity.

The energy of the hadronic τ candidates is shifted upward and downwards using the factors in Table 7.11 according to their energy, pseudorapidity and number of prongs [41].

Table 7.11: Relative systematic errors due to the energy scale uncertainty of τ candidates depending on p_T and η determined separately for 1-prong and multi-prong τ decays.

Systematic uncertainty	Detector Regions		
1-prong	$\|\eta\|$ <1.3	1.3< $\|\eta\|$ <1.6	$\|\eta\|$ >1.6
p_T = 20-30 GeV	4.5%	5%	4.5%
p_T > 30 GeV	3.5%	5%	4.5%
multi-prong	$\|\eta\|$ <1.3	1.3< $\|\eta\|$ <1.6	$\|\eta\|$ >1.6
p_T = 20-30 GeV	6.5%	5.5%	5.5%
p_T = 30-40 GeV	5.5%	5.5%	5.5%
p_T > 40 GeV	4.5%	5%	5%

The E_T^{miss} of the events is also scaled simultaneously with the energy scale of electrons and hadronic τ candidates. The uncertainty on the cluster energy scale is derived from E/p studies by comparing data and Monte Carlo simulation [63]. The effect of the uncertainty on the E_T^{miss} can be estimated by scaling the topological cluster energies that contribute to its measurement. The energy of the topological clusters is multiplied by the following p_T dependent function

$$1 + a\left(1 + \frac{b}{p_T[\text{GeV}]}\right).$$

where p_T is the energy of the cluster. The systematic uncertainty is calculated for $a = \pm 0.07$ and $b = 0.93$ according to [48], which was found to give the maximal shift.

7.8.6 Cross section and luminosity

The Monte Carlo background event samples are normalized according to the integrated luminosity. An uncertainty on the production cross section of ± 5% is estimated for electroweak background [45] and of +7.0%/-9.6% for the $t\bar{t}$ background [64]. The systematic uncertainty in the measured luminosity is 3.7% [58].

7.8.7 Systematic uncertainties on the background estimation

Systematic uncertainties are associated to the normalization factors for the Monte Carlo simulated W/Z+jet backgrounds. The statistical errors of the normalization factors (see Section 7.6.1 and 7.6.2) are used.

The contribution of the multi-jet background is estimates by a data-driven method. The different sources of systematic uncertainty are described in section 7.6.3. Both statistical and systematic errors on the background determination are taken into account. The overall systematic uncertainty on the multi-jet background estimation is less than 10% and has only a minor effect on the cross section measurement since this background is strongly suppressed by the lepton isolation cuts.

7.8.8 Systematic uncertainty on the acceptance

The systematic uncertainty in the calculation of the geometric and kinematic acceptance (Eq. 7.12) is estimated using different sets of parton density functions and different parton shower models. Details can be found in [1].

Table 7.12 shows the systematic uncertainty contributions to the determination of the cross section.

Table 7.12: Relative systematic uncertainties on the inclusive $Z \rightarrow \tau\tau$ production cross section measurement.

Systematic uncertainty $\delta\sigma/\sigma$ (%)	$\tau_\mu\tau_\mathrm{h}$ channel	$\tau_e\tau_\mathrm{h}$ channel
Lepton efficiency scale factors	1.7	5.0
Muon $\mathrm{p_T}$ resolution	< 0.05	-
Electron $\mathrm{p_T}$ resolution	-	0.1
τ id. efficiency	5.2	5.2
e, τ and E_T^{miss} energy scale	8.2	9.3
$e \rightarrow \tau$ misidentification rate	-	0.2
τ trigger efficiency	-	4.7
W/Z background normalization factors	<0.05	<0.05
Multi-jet background estimation	0.8	1.3
MC backgrounds cross sections	0.1	0.2
Monte Carlo statistics	1.2	1.4
Acceptance factor A_Z	3.1	3.4
Total systematic error	10.4	13.2

Conclusion and outlook

During the last two years, the Large Hadron Collider (LHC) delivered an integrated luminosity of more than 5 fb^{-1} of proton-proton collisions at a centre-of-mass energy of 7 TeV. The ATLAS detector is one of the two main detectors designed to fully exploit the discovery potential of the LHC. The searches for the Higgs boson and new phenomena beyond the Standard Model of particle physics require precise knowledge of the detector performance and of the background processes. This thesis presents the measurement of the inclusive $Z \rightarrow \tau\tau$ production cross section in proton-proton collisions at $\sqrt{s} = 7$ TeV with the ATLAS detector using data collected during the year 2011 corresponding to an integrated luminosity of 1.5 fb^{-1}. The majority of the results shown have been already published in [1].

The study of $Z \rightarrow \tau\tau$ production is important for several reasons. First, the measurement of the inclusive $Z \rightarrow \tau\tau$ cross section can confirm the measurements of Z boson production using electron and muon pair decays, providing information of the parton density functions at the energy scale of the Large Hadron Collider. For the search for low-mass Higgs boson decays into τ lepton pairs, the measurement of the $Z \rightarrow \tau\tau$ background production cross section at the LHC is indispensable. Finally, the reconstruction of $Z \rightarrow \tau\tau$ events is necessary for the measurement of the τ lepton identification efficiency and fake rate which are needed for many new physics searches and cannot be reliably determined by Monte Carlo simulation.

$Z \rightarrow \tau\tau$ production can be measured in different final states depending on the decay modes of the two τ leptons. In this thesis, semileptonic final states have been investigated where one τ lepton decays into an electron or muon and neutrinos and the other one into hadrons and a neutrino. The background contributions have been estimated from data either completely (in the case of the QCD multi-jet background) or by normalizing the Monte Carlo simulated background to the data using background enriched control data samples (in the case of the weak gauge bosons contribution). The muon trigger and reconstruction efficiencies have been determined from data as well in this thesis. The results are used for many other ATLAS measurements. The results of the inclusive $Z \rightarrow \tau\tau$ cross section measurement in the semileptonic final state are

$$\sigma(pp \rightarrow Z + X, Z \rightarrow \tau\tau) = 998.1 \pm 23.7(\text{stat}) \pm 131.9(\text{syst}) \pm 36.9(\text{lumi}) \text{ pb} \quad (\tau_e\tau_\text{h} \text{ channel}),$$

$$\sigma(pp \rightarrow Z + X, Z \rightarrow \tau\tau) = 912.4 \pm 15.0(\text{stat}) \pm 94.7(\text{syst}) \pm 33.7(\text{lumi}) \text{ pb} \quad (\tau_\mu\tau_\text{h} \text{ channel}),$$

in the invariant mass range [66-116] GeV. They can be combined with the cross section mea-

surement in the leptonic final state $\tau_e\tau_\mu$ [1] to give

$$\sigma(pp \to Z + X, Z \to \tau\tau) = 920.6 \pm 16.7(\text{stat}) \pm 78.1(\text{syst}) \pm 34.0(\text{lumi}) \text{ pb} \quad \text{(combined)}$$

and are compatible with the theoretical prediction (960 ± 50) pb, with the ATLAS cross section measurement for $Z \to ee/\mu\mu$ events [62]

$$\sigma(pp \to Z + X, Z \to \mu\mu, ee) = 937 \pm 6(\text{stat}) \pm 9(\text{syst}) \pm 32(\text{lumi}) \pm 16(\text{acc})^2 \text{ pb}$$

and with the measurement of the CMS experiment [49]

$$\sigma(pp \to Z + X, Z \to \tau\tau) = 1.00 \pm 0.05(\text{stat}) \pm 0.08(\text{syst}) \pm 0.04(\text{lumi}) \text{ nb} \quad \text{(combined)}^3.$$

[2]The theoretical uncertainty in the extrapolation from the fiducial region to the phase space.
[3]The cross section is calculated in the invariant mass range [60-120] GeV.

List of Figures

List of Tables

Acknowledgements

I would like to thank my supervisor Hubert Kroha for giving me the opportunity to prepare my thesis at the Max Planck Institut für Physik in Munich. This was a valuable experience and all people were always available in helping me during my thesis with many suggestions.
I am grateful to Oliver and Sandra Kortner and Mike Flowerdew for helping me during my thesis.
I want to express my gratitude to Mauro Iodice, for introducing me to the ATLAS experiment during my Bachelor thesis and helping me during my PhD.
I would like to thank Elias Coniavitis, Despoina Evangelakou, Jana Novakova and Frank Seifert, for the fruitful collaboration.

A big "THANKS" to all the members of the ATLAS-MDT group (including Andreas and Paola) at the Max Planck Institut für Physik in Munich, for the time spent during lunch and for the german translations.
A special thank to Marco Vanadia, for the fruitful discussions ranging from physics, films, music and football and Elena, for being always the last in the ranking in every game played.

Finally it's time to mention the people who made this thesis possible.

Ilaria, la mia migliore amica - alias *Pollo* - per essermi stata sempre vicina durante questi anni dimostrandosi un'amica vera nonostante la distanza.

Verena, il mio amore, perchè anche se non hai contribuito direttamente al completamento del mio dottorato, la tua presenza rende tutto più sereno, e il pensiero di un futuro sempre migliore ... insieme.

Nulla sarebbe stato possibile senza i miei splendidi genitori Ferdinando e Margherita, che hanno da sempre incoraggiato i miei studi ed hanno sempre fatto sentire casa un po più vicina.

Bibliography

[1] The ATLAS Collaboration, G. Aad et al., *$Z \to \tau\tau$ cross section measurement in proton-proton collisions at 7 TeV with the ATLAS experiment*, ATLAS conference note: ATL-CONF-2012-006. For further details see also ATLAS internal communication: ATL-COM-PHYS-2011-1660.

[2] S. Glashow, *Partial Symmetries of Weak Interactions*, Nucl. Phys. **22** (1961) 579-588.

[3] S. Weinberg, *A Model of Leptons*, Phys. Rev. Lett. **19** (1967) 1264-1266.

[4] A. Salam, *Weak and Electromagnetic Interactions*, originally printed in "Svartholm: Elementary Particle Theory, Proceedings of the Nobel Symposium held 1968 at Lerum, Sweden", Stockholm 1968, 367-377.

[5] E. Noether, *Invariante Variationsprobleme*, Gött. Nachr. (1918) 235-257.

[6] P. Higgs, *Broken Symmetries and the Masses of Gauge Bosons*, Phys. Rev. Lett. **13** (1964) 508-509.

[7] F. Englert and R. Brout, *Broken Symmetry and the Mass of Gauge Vector Mesons*, Phys. Rev. Lett. **13** (1964) 321-322.

[8] G. S. Guralnik, C. R. Hagen, and T. W. B. Kibble, *Global Conservation Laws and Massless Particles*, Phys. Rev. Lett. **13** (1964) 585-587.

[9] A. Djouadi, *The Anatomy of electro-weak symmetry breaking: The Higgs boson in the standard model*, Phys. Rept. **457** (2008) 1-216, `arXiv:hep-ph/0503172`.

[10] The UA1 Collaboration, G. Arnison et al., *Experimental observation of isolated large transverse energy electrons with associated missing energy at $\sqrt{s} = 540$ GeV*, Phys. Lett. **B122** (1983) 103-116.

[11] The UA1 Collaboration, G. Arnison et al., *Experimental observation of lepton pairs of invariant mass around 95 GeV/c^2 at the CERN SPS collider*, Phys. Lett. **B126** (1983) 398-410.

[12] The UA2 Collaboration, M. Banner et al., *Observation of single isolated electrons of high transverse momentum in events with missing transverse energy at the CERN pp collider*, Phys. Lett. **B122** (1983) 476-485.

[13] The UA2 Collaboration, P. Bagnaia et al., *Evidence for $Z^0 \to e^+e^-$ at the CERN pp collider*, Phys. Lett. **B129** (1983) 130-140.

[14] Particle Data Group Collaboration. K. Nakamura et al., *Review of Particle Properties*, J. Phys. **G37** (2010) 075021.

[15] S. Myers, *The LEP collider, from design to approval and commissioning*, proceedings of CERN Accelerator School, Nov. 26, 1990, CERN yellow report 91-08.

[16] L. Evans and P. Bryant, *LHC machine*, JINST **3** (2008) S08001.

[17] The ATLAS Collaboration, G. Aad et al., *The ATLAS Experiment at the CERN Large Hadron Collider*, JINST **3** (2008) S08003.

[18] The CMS Collaboration, S. Chatrchyan et al., *The CMS experiment at the CERN LHC*, JINST **3** (2008) S08004.

[19] The ALICE Collaboration, K. Aamodt et al., *The ALICE experiment at the CERN LHC*, JINST **3** (2008) S08002.

[20] The LHCb Collaboration, A. Augusto Alves Jr et al., *The LHCb Detector at the CERN LHC*, JINST **3** (2008) S08005

[21] The ATLAS Collaboration, Magnet system: Technical Design Report, CERN/LHCC/97-18, 1997.

[22] The ATLAS Collaboration, Inner Detector: Technical Design Report, CERN-LHCC-97-016/017, 1997.

[23] The ATLAS Collaboration, ATLAS liquid-argon calorimeter: Technical Design Report, CERN-LHCC-96-041, 1996.

[24] The ATLAS Collaboration. ATLAS tile calorimeter: Technical Design Report, CERN-LHCC-96-042, 1996.

[25] M. Aharrouche et al., *Energy linearity and resolution of the ATLAS electromagnetic barrel calorimeter in an electron test-beam*, Nucl. Instrum. Methods Phys. Res. **A568** (2006) no. 2, 601-623.

[26] B. Dowler et al., *Performance of the ATLAS hadronic end-cap calorimeter in beam tests*, Nucl. Instrum. Methods Phys. Res. **A482** (2002) no. 1-2, 94-124.

[27] J. Archambault et al., *Energy calibration of the ATLAS Liquid Argon Forward Calorimeter*, JINST **3** (2008) no. 02, P02002.

[28] The ATLAS Collaboration, ATLAS muon spectrometer: Technical Design Report, CERN-LHCC-97-022, 1997.

[29] J. Knobloch et al., LHC Computing Grid: Technical Design Report , CERN-LHCC-2005-024, Geneva, 2005.

[30] The ATLAS Collaboration, G. Aad et al., *The ATLAS Simulation Infrastructure*, Eur. Phys. J. **C70** (2010) 823.

[31] The GEANT-4 Collaboration, S. Agostinelli et al., *GEANT-4: A simulation toolkit*, Nucl. Instrum. Meth. **A506** (2003).

[32] T. Sjostrand, S. Mrenna, and P.Z. Skands, *PYTHIA 6.4 Physics and Manual*, JHEP **09** (2009) 026.

[33] S. Frixione and B. Webber, *Matching NLO QCD computations and parton shower simulations*, JHEP **0206** (2002) 029, `arXiv:hep-ph/0204244`.

[34] G. Corcella at al., *HERWIG 6.5*, JHEP **0101** (2001) 010.

[35] M. Mangano, M. Moretti, F. Piccinini, R. Pittau, and A. Polosa, *ALPGEN, a generator for hard multiparton processes in hadronic collisions*, JHEP **07** (2003) 001.

[36] The TOTEM Collaboration, G. Antchev et. al., *First measurement of the total proton-proton cross-section at the LHC energy of* $\sqrt{s} = 7$ *TeV*, EPL **96** (2011) 21002.

[37] The ATLAS Collaboration, G. Aad et al., *Electron performance measurements with the ATLAS detector using the 2010 LHC proton-proton collision data*, CERN-PH-EP-2011-117, submitted to Eur. Phys. J. C, `arXiv:1110.3174`.

[38] R. Nicolaidou et al., *Muon identification procedure for the ATLAS detector at the LHC using Muonboy reconstruction package and tests of its performance using cosmic rays and single beam data*, J. Phys.: Conf. Ser. **219** 032052.

[39] R. Duda and P. Hart, *Use of the Hough Transformation of Detect Lines and Curves in Pictures*, Comm. ACM, Vol. 15, pp. 11-15 (1972).

[40] M. Cacciari, G.P. Salam, and G. Soyez, *The anti-k_T clustering algorithm*, JHEP **0804** (2008) 063, `arXiv:0802.1189v2`.

[41] The ATLAS Collaboration, G. Aad et al., *Performance of the Reconstruction and Identification of Hadronic Tau Decays with ATLAS*, ATLAS Conference note: ATLAS-CONF-2011-152, Nov. 2011.

[42] Y. Freund and R. Shapire, *Experiments with a New Boosting Algorithm*, in Machine Learning: Proceedings of the Thirteenth International Conference (1996) 148-156.

[43] L. Breiman, J. Friedman, C. Stone, and R. Olshen, *Classification and Regression Trees*, Chapman & Hall, 1984.

[44] The ATLAS Collaboration, G. Aad et al., *Muon reconstruction efficiency in reprocessed 2010 LHC proton-proton collision data recorded with the ATLAS detector*, ATLAS conference note: ATL-CONF-2011-063, Apr. 2011.

[45] The ATLAS Collaboration, G. Aad et al., *Measurement of the $W\rightarrow l\nu$ and $Z/\gamma^* \rightarrow ll$ production in proton-proton collisions at $\sqrt{s} = 7$ TeV*, JHEP **12** (2010) 060.

[46] The ATLAS Collaboration, G. Aad et al., *A measurement of the ATLAS muon reconstruction and trigger efficiency using J/ψ decays*, ATLAS conference note: ATLAS-CONF-2011-021, Mar. 2011.

[47] The ATLAS Collaboration, G. Aad et al., *ATLAS Muon Momentum Resolution in the First Pass Reconstruction of the 2010 pp Collision Data at $\sqrt{s} = 7$ TeV*, ATLAS conference note: ATLAS-CONF-2011-046, Mar. 2011.

[48] The ATLAS Collaboration, G. Aad et al., *Measurement of the Z to tau tau Cross Section with the ATLAS Detector*, Phys. Rev. **D84** (2011) 112006.

[49] The CMS Collaboration, S. Chatrchyan et al., *Measurement on the Inclusive Z Cross Section via Decays to Tau Pairs in pp Collision at $\sqrt{s} = 7$ TeV*, JHEP **08** (2011) 117.

[50] J. Pumplin et al., *New generation of parton distributions with uncertainties from global QCD analysis*, JHEP **0207** (2002) 012.

[51] S. Jadach, Z. Was, R. Decker, and J. H. Kühn, *The τ decay library TAUOLA, version 2.4*, Comput. Phys. Comm., vol. 76, 1993.

[52] P. Golonka and Z. Was, *PHOTOS Monte Carlo: A Precision tool for QED corrections in Z and W decays*, Eur. Phys. J. **C45** (2006) 97.

[53] J. M. Butterworth, J. R. Forshaw, and M. H. Seymour, *Multiparton Interactions in Photoproduction at HERA*, Z. Phys. **C72** (1996) 637.

[54] https://atlas-lumicalc.cern.ch/ (for ATLAS members only).

[55] The ATLAS Collaboration, G. Aad et al., *Data-Quality Requirements and Event Cleaning for Jets and Missing Transverse Energy Reconstruction with the ATLAS Detector in Proton-Proton Collisions at a Center-of-Mass Energy of $\sqrt{s} = 7$ TeV*, ATLAS conference note: ATL-CONF-2010-038.

[56] The ATLAS Collaboration, G. Aad, *Local hadronic calibration*, ATLAS public note: ATL-LARG-PUB-2009-001.

[57] A. Sherstnev and R.S. Thorne, *Parton Distributions for LO Generators*, Eur. Phys. J. **C55** (2008) 553.

[58] The ATLAS Collaboration, G. Aad et al., *Luminosity Determination in pp Collisions at $\sqrt{s}$ = 7 TeV using the ATLAS Detector in 2011*, ATLAS conference note: ATL-CONF-2011-116, Aug. 2011.

[59] K. Melnikov and F. Petriello, *Electroweak gauge boson production at hadron colliders through $O(\alpha_S^2)$*, Phys. Rev. **D74** (2006), 114017, `arXiv:hep-ph/0609070v1`.

[60] R. Gavin et al., *FEWZ 2.0: A code for hadronic Z production at next-to-next-to-leading order*, `arXiv:1011.3540v1 [hep-ph]`.

[61] A.D. Martin et al., *Parton distributions for the LHC*, Eur. Phys. J. **C63** (2009) 189-285, `arXiv:0901.0002v3`.

[62] The ATLAS Collaboration, G.Aad et al., *Measurement of the inclusive $W^{\pm}$ and Z/γ^* cross sections in the electron and muon decay channels in pp collisions at $\sqrt{s}$ = 7 TeV with the ATLAS detector*, `arXiv:1109.5141 [hep-ex]`.

[63] The ATLAS Collaboration, G.Aad et al., *ATLAS Calorimeter Response to Single Isolated Hadrons and Estimation of the Calorimeter Jet Scale Uncertainty*, ATLAS conference note: ATLAS-CONF-2011-028, Mar. 2011.

[64] The ATLAS Collaboration, G.Aad et al., *Measurement of the top-quark pair production cross section in pp collisions at $\sqrt{s}$ = 7 TeV in dilepton final states with ATLAS*, ATLAS conference note: ATL-CONF-2011-100, Oct. 2011.